UNLV Theses, Dissertations, Professional Papers, and Capstones

5-1-2013

How Accurately Can the Inclination Angle, Position Angle, and Location of the Dynamic Center be Measured from the Neutral Hydrogen Disk in the Central Regions of Dwarf Galaxies?

John Henry Boisvert
University of Nevada, Las Vegas, johnb@physics.unlv.edu

Follow this and additional works at: https://digitalscholarship.unlv.edu/thesesdissertations

Part of the Astrophysics and Astronomy Commons

HOW ACCURATELY CAN THE INCLINATION ANGLE, POSITION ANGLE,

AND LOCATION OF THE DYNAMIC CENTER BE MEASURED FROM

THE NEUTRAL HYDROGEN DISK IN THE CENTRAL REGIONS

OF DWARF GALAXIES?

By

John Henry Boisvert

Bachelor of Science in Physics
University of Nevada Las Vegas
2010

A thesis submitted in partial fulfillment
of the requirements for the

Master of Science – Physics

Department of Physics & Astronomy
College of Sciences
The Graduate College

University of Nevada, Las Vegas
August 2013

UNLV
UNIVERSITY OF NEVADA LAS VEGAS

THE GRADUATE COLLEGE

We recommend the thesis prepared under our supervision by

John Henry Boisvert

entitled

How Accurately Can the Inclination Angle, Position Angle, and Location of the Dynamic Center Be Measured From the Neutral Hydrogen Disk in the Central Regions of Dwarf Galaxies?

is approved in partial fulfillment of the requirements for the degree of

Master of Science - Physics

Department of Physics and Astronomy

George Rhee, Ph.D., Committee Chair

Stephen Lepp, Ph.D., Committee Member

Kentaro Nagamine, Ph.D., Committee Member

Rodney Metcalf, Ph.D., Graduate College Representative

Kathryn Hausbeck Korgan, Ph.D., Interim Dean of the Graduate College

August 2013

ABSTRACT

How accurately can the inclination angle, position angle, and location of the dynamic center be measured from the neutral hydrogen disk in the central regions of dwarf galaxies?

by

John Henry Boisvert

Dr. George Rhee, Examination Committee Chair
Professor of Astronomy
University of Nevada, Las Vegas

Rotation curves measured using H I emission are a powerful tool for probing the mass distribution of galaxies. We investigate the accuracy with which rotation curves can be determined using the tilted-ring model. We have examined the effect of varying the dynamic center on measured rotation velocities within the inner regions of galaxies where the disagreement between theory and observation is the greatest. We examine a sample of dwarf galaxies (and one spiral galaxy) from the THINGS high-resolution survey (Walter et al. 2008). We find that the measured rotation curve is quite sensitive to the location of the dynamic center. This center is difficult to determine for dwarf galaxies. We also find that errors in rotation velocities determined with the tilted-ring method have been underestimated in previous studies.

life in numerous ways.

I would like to thank John Kilburg and Jay Nietling for helping me with the computer issues I had while working on this project.

I would also like to thank Robert Thompson for helping me get up to speed with the Latex document markup language. And I cannot forget all of the graduate students and postdoctoral researchers who I've had great intellectual conversations with over the past couple years. Talking with you all about the latest topics in the field has been a rewarding experience and brings everything into perspective.

A huge thanks goes to all of my friends who have had to deal with me droning on about my research topic and other areas of astrophysics. Your support has always reinforced my decision to continue my studies. You all have made me feel like I am doing the right thing with my life. I also would like to thank Mariela Preciado for keeping me sane during the rough times and for always making sure I had a good meal on the days where I just wanted to work. You have been a constant source of positivity during the last year and a half. Last, but certainly not least, I would like to express my thanks and love to Barbara and Louis Boisvert, my mother and father. Without your unconditional love and overwhelming support, I would not have made it anywhere near where I stand today.

TABLE OF CONTENTS

LIST OF TABLES

LIST OF FIGURES

CHAPTER 1

INTRODUCTION

In 1933, American physicist and radio engineer Karl Guthe Jansky discovered the first radio signals emanating from outside the Solar System, in the direction of the center of the Galaxy. He was observing Sagittarius A* for the first time (Jansky 1933). The unit for frequency dependent spectral flux density was named after him. In cgs, $1\,\mathrm{Jy} = 10^{-23}\,\mathrm{erg\,s^{-1}\,cm^{-2}\,Hz^{-1}}$. In 1945, Henrik van de Hulst received an assignment from famous Dutch astronomer, Jan Oort: determine what spectral lines reside in the radio region of the electromagnetic spectrum. He predicted that a hyperfine transition of ground state hydrogen lay in the radio region at a wavelength of 21-cm (van de Hulst 1945). The hyperfine splitting of ground state hydrogen arises from the coupling of the magnetic moment of the electron with the magnetic field produced by the proton. This splits the ground state of hydrogen into two spin states. The higher energy spin state has the spin of the electron and proton parallel and is a triplet state. The lower energy spin state is where the spins are antiparallel and is a singlet state. The origin of 21-cm emission is the spin-flipping of electrons from being parallel to antiparallel compared to the spin of the proton (for more information about 21-cm radiation, see Appendix B).

21-cm radiation was first observed to be coming from the Galaxy at most galactic latitudes by Ewen & Purcell (1951) and Muller & Oort (1951). This was the beginning of a new era in astronomy as the 21-cm line proved to be an excellent tracer of galactic dynamics by tracking the motions of neutral hydrogen (HI) gas. The Doppler motions of the gas along the line of sight allows for the speed of the gas to be mapped. The 21-cm radiation was used to map out the hydrogen distribution of the Galaxy which determined it lies in a disk with spiral arms (Oort 1955). This emission line has since been used to probe the interstellar medium of other galaxies.

Prior to the detection of the 21-cm emission line, galaxy motions were solely

determined by measuring stellar velocities using long-slit spectroscopy. The idea is to obtain a spectrum along the major axis of a galaxy by only allowing light from a small slit centered on the major axis. As one moves across the slit, the emission and absorption lines originating from stellar sources within those galaxies will be redshifted or blueshifted, indicating a velocity at that location. A plot of the rotation speed as a function of distance from the center of the galaxy can be found. These rotation curves model the large scale circular motions of a galaxy. Working in the optical and UV regions of the electromagnetic spectrum is difficult due to extinction and reddening of spectra caused by dust obscuration. This was a motivation for Oort to investigate radio emission sources. 21-cm radiation is optically thin; this means that the absorption of hydrogen (by itself or other sources) is negligible. This is indeed the case at least until cosmological expansion shifts the CMB redward enough to prevent the repopulation of the parallel spin state and stimulate the 21-cm emission and also in the early epoch before the universe was reionized (Draine 2011). Hɪ emission from galaxies extends much further from the galaxy center than stellar light sources which allows one to probe the dynamics at large radii.

Rotation Curves and Evidence for Dark Matter in Galaxies

Rotation curves generated from stellar sources and Hɪ emission show that galaxies do not rotate at speeds predicted by the visibly observed mass density distributions. Newtonian gravity predicts that, for a point mass, the rotation speed should decrease as $V_{rot} \propto r^{-1/2}$. Galaxies are not point masses though, they have an extended mass distribution which alters the rotation speed from this dependency. Observationally, as a function of radius, V_{rot} increases then remains constant. In order to infer the mass distribution, the contribution of the different components (Hɪ component, stellar component, etc.) of the galaxy to the rotation curve must be determined (see Figure 1 for an example of this). Surprisingly, adding the contributions from components

observed can not explain the observed rotation curve. This implies that there is mass present in the galaxy that has not been detected. Simply put, the total mass inferred from the rotation curve of galaxies does not agree with the amount of visible mass seen in the galaxy. The distribution of this *dark* matter extends well beyond the optical and radio discs of galaxies. In Figure 1, NGC 7331 becomes dark matter dominated at 22 kpc; the contributions from the visible components all decrease whereas the halo component continues to rise. The combination of these components at large radii give the flat rotation curve. This dark matter only interacts via the gravitational force attracts baryonic matter. There is evidence for dark matter in galaxy clusters too, and in fact the mass-to-light ratio increases for larger systems such as these.

Other Theories

Other theories to explain galaxy rotation curves include the Modified Newtonian Dynamics (MOND) introduced by Milgrom (1983). MOND does away with the missing matter by assuming that gravity deviates from the r^{-2} dependence at large radii allowing the speed of stars and gas to increase.

MAssive Compact Halo ObjectS (MACHOS) have been proposed as a possible candidate for dark matter. MACHOS can include objects such as rogue planets, brown dwarfs, or any other extremely low surface brightness object. However, gravitational microlensing studies of the Large Magellanic Cloud have revealed that MACHOS alone can not account for the amount of missing matter in galaxies (Alcock et al. 2000).

Galaxy Selection

In order to determine the mass distribution in galaxies, accurate rotation curves are required. Rotation curves track the mass distribution within the galaxy. The extent of HI disks help characterize the properties of the dark matter halos beyond

the visible stellar disks of galaxies. Dwarf galaxies and low surface brightness (LSB) galaxies may be well suited for studying the dark matter distribution. This is because these galaxies may be dominated, at all radii, by dark matter; they lack strong stellar components and other components such as bulges and pseudobulges. An example of this is shown in Figure 2 from van der Kruit & Freeman (2011). This is a rotation curve of the LSB disk spiral galaxy NGC 3198. Visibly, this galaxy only has a disk component. The derived rotation curve is shown going through the data points. Two fits were made to reconcile the contributions to this rotation curve, one assuming the disk contributes the maximum amount to the rotation curve (panel a) and the other with an arbitrary fit (panel b). Each fit shows that the galaxy is dark matter dominated at large radii. Dwarf galaxies are studied due to their small scale size, and the investigation of the small scale structure of dark matter halos are possible with high resolution observations of those nearby. LSBs are usually twice the scale size of dwarf galaxies. Since we seek an understanding of the distribution of dark matter, it makes sense to go to smaller galaxies in which the dark matter affects the dynamics more than any visible components. Correctly determining the dark matter density profile over all radii of galaxies is a challenge for theories of galaxy formation and evolution.

<center>The Navarro-Frenk-White Profile</center>

Is there a single density profile which describes all dark matter halos? Or is there a family of functions which can describe the mass distribution of galaxies? To answer these questions, high-resolution N-body simulations testing the ΛCDM concordance model of a hierarchically clustering universe are needed. They have been shown to produce cosmic web structures similar to those seen in observations (Navarro et al. 1997). N-body simulations include dark matter particles only, which are collisionless. The simulations suggest that the Navarro-Frenk-White (NFW)

<center>4</center>

profile is the characteristic density profile which describes the distribution of dark matter particles within all the halos formed in these simulations (Navarro et al. 1997). This profile predicts a sharp rise of the matter density to a cusp at the halo center. Despite the lack of evidence of a cusp in observations of dwarf galaxies, the NFW profile has been used because it provides a good fit to all of the dark matter halos in cosmological simulations. However, both LSBs and dwarf galaxies can be represented with a shallow core or a low concentration dark matter halo (Gentile et al. 2004; Rhee et al. 2004). Shallow cores have classically been modeled with a pseudo-isothermal core (ISO) model which hold the density of the central regions constant. Both the NFW and ISO models require two parameters to describe the halos in full. The Einasto halo model shows improvement over both the NFW and ISO profiles (Navarro et al. 2004; Chemin et al. 2011) however at the cost of adding another parameter. See Appendix C for an investigation of these three density profiles.

The Effect of Baryons on Dark Matter

The real universe is comprised of baryonic matter and dark matter. In current models, baryonic matter streams into dark matter halos along filaments. This gas then collapses due to its self-gravity and star formation begins. Halos are responsible for igniting the first stars in the universe, the essential building blocks of galaxies today. When star formation occurs, almost immediately in astronomical terms, the O and B type stars begin to explode as supernovae due to their short lifetimes. Gravitational feedback from these supernovae events could remove the central density cusp and form a core. Supernovae feedback could also prevent the formation of bulges by kicking parts of the stellar population out of their circular orbits (Governato et al. 2010). The ΛCDM cosmological model describes the large scale structure of the universe well, but it does less well with the smaller structure of the universe, such as the dynamics and mass distribution of individual galaxies and dwarf galaxies (Klypin et al. 2002).

Dwarf galaxy hydrodynamic simulations done by Governato et al. (2010), which include dark matter and baryonic physics, show that the combination of supernovae winds throughout the galaxy remove low angular momentum baryons from the centers of galaxies. This prevents the formation of bulges and suppress star formation. Star formation happens in dense clouds where the Jeans conditions are satisfied. These dense clouds fall toward the center of the galaxy as star formation and supernovae are happening throughout the galaxy. As the cloud is traveling towards to center of the galaxy, it is bombarded by the collective supernovae feedback and subsequently destroyed. The removal of baryonic matter from the central regions of the galaxy causes a loss in the gravitational binding energy of the dark matter, which then causes it to expand into a shallow central profile. Recently the Eris (Guedes et al. 2011) zoom-in high resolution cosmological hydrodynamics simulation of a Milky Way type disc galaxy exhibit a miss match between the center of the dark matter density profile and the dynamic center of the galaxy of order a few hundreds of parsecs. They also have seen that the growth of this offset flattens the central density profile to a core within one kiloparsec (Kuhlen et al. 2013). One has to wonder how the story will change as the resolution of high-resolution cosmological simulations continues to increase, notably will the NFW profile remain the 'universal' halo density profile or will other profiles like the Einasto profile be a better fit.

Motivation for Current Work

In this work we investigate the accuracy of rotation measurements. How would the derived rotation curve and, thus, density profile change if important model parameters, such as the dynamic center were measured incorrectly? In addition, what are the uncertainties associated with determining important model parameters? In this thesis we investigate how accurately the tilted-ring model parameters are able to be calculated and the effect on the circular velocity, $V_c(R)$. The inner parts of galaxies

are difficult to model because of projection effects due to the optically thin nature of H I emission. Consider two H I clouds along a light of sight which are traveling at two distinct speeds. A spectrum of the line of sight will show two distinct emission profiles, one from each cloud. This makes extracting gas velocities more difficult for inclined systems and for the inner regions of galaxies. Often a tilted-ring model (Begeman 1989) is used to extract the large scale circular motions of the galaxy with some assumptions. This is a dynamical mass model which derives a rotation curve from a two dimensional observed velocity field. Currently, the algorithm requires some amount of human intervention to initialize. For example, a radio nuclear source or the presence of a massive star cluster is taken as an initial dynamic center estimate, if available (Trachternach et al. 2008).

The Square Kilometre Array

The advent of the Australian Square Kilometre Array Pathfinder (ASKAP) will provide a huge amount of high quality data. The array consists of 36 12-meter radio telescopes which will be used in the Widefield ASKAP L-band Legacy All-sky Blind surveY (WALLABY). This survey will deliver observations of the H I emission for hundreds of thousands of galaxies (Duffy et al. 2012). There is a need for a fully automated algorithm to process galaxies and determine rotation curves. This work investigates how well the parameters of tilted-ring models, which describe galaxy dynamics, can be extracted with minimal human intervention. More specifically how accurately can the dynamic center of the galaxy be found using the tilted ring model on highly resolved galaxies and how does an incorrect dynamic center affect the rotation curve and derived density distribution? These questions need to be answered before the flood of galaxy data comes down the pipeline.

CHAPTER 2

THE TILTED-RING MODEL

Spiral galaxies tend to have a flattened stellar distribution which can be represented by a rotating disk. The so called tilted-ring model is designed to describe a rotating disk. It was implemented by Begeman (1989) to model the rotation curve of NGC 3198 from its HI distribution. The frequency of radiation emitted by the neutral hydrogen gas is Doppler shifted due to the radial motion of the gas. The tilted-ring model assumes that the gas is rotating in a plane with circular orbits, i.e., the circular motions dominate the non-circular (random) motions. This may not necessarily be the case in most radii of dwarf galaxies. Random motions seen in dwarf galaxies will decrease the true rotation velocity from the circular velocity. This is because circular motions imply there are no outside forces changing the velocity vector of an object; an object orbits around the center of the galaxy on a circular orbit. However, galaxies have internal events such as supernovae explosions or dense regions which would change the velocity vector of an object and will cause it to deviate from its circular motion. The model constructs concentric annuli and describes each annulus with six parameters. These parameters are determined independently for each annulus. They are:

1., 2. (x_c, y_c) denote the location of the dynamic center, in right ascension (α) and declination (δ). This is, by definition, the origin of the rotation curve. This is not necessarily the same as the optical center of the galaxy because this dynamic center depends on the velocity field of the galaxy.

3. V_{sys}, the velocity of the galaxy with respect to the sun.

4. The position angle (ϕ) of the major axis. This is defined as the angle between the northern direction of the sky to the major axis of receding emission. Figure 3 shows an illustration of position angle.

5. The inclination angle (i) of the galaxy. The inclination angle is defined as the

angle between the line-of-sight and a line normal to the plane of the galaxy. Figure 4 shows an illustration of the inclination angle. This projects the circular galaxy on the sky as an ellipse (see Figure 3). The ellipticity of the projected ellipse, ϵ, is related to the inclination angle by:

$$\cos(i) \;=\; 1 - \epsilon \tag{2.1}$$

6. The circular velocity, V_c, a distance R from the dynamic center. This velocity is assigned to a single annulus. The combination of circular velocity measurements for all annuli construct the rotation curve. Circular velocity is the velocity a particle would have if it was orbiting in uniform circular motion around the center of the galaxy. The true value of the circular velocity curve may be higher than the observed velocities due to projection effects from inclination (Rhee et al. 2004). The circular velocity is different from the rotation velocity. Rotation velocity is the velocity at which a particle is actually revolving about the dynamic center.

The orientation parameters, ϕ and i, define an ellipse projected on the sky. This ellipse is now broken up into many concentric annuli. Each annulus is characterized independently by the six tilted-ring parameters introduced above. The width of each concentric annulus is determined by the size of the radio beam. A good rule of thumb is to choose a width which allows a few annuli to fit within a single beam. The goal of this model is to build a rotation curve by extracting a circular velocity from each annulus. Each annulus is comprised of many lines-of sight each providing a radial velocity measurement. These line-of-sight velocities are related to the tilted-ring parameters by:

$$V_{rad}(x,y) \;=\; V_{sys} + V_c(R)\,\sin(i)\,\cos(\theta) \tag{2.2}$$

This expression breaks the radial velocities into two components; one representing

the entire galaxy receding away from the Sun (V_{sys}) and the other representing the internal rotation of the galaxy, $V_c(R)$. R is taken as the mean radius of the annulus. θ represents the azimuthal angle within the galaxy. This angle is related to the orientation parameters through the transformation matrices. Using transformation matrices, one can relate sky coordinates to a unique pair of θ and R. It does this through the tilted ring parameters: ϕ, i, x_c, and y_c.

$$\cos(\theta) = \frac{-(x - x_c)\sin(\phi) + (y - y_c)\cos(\phi)}{R} \tag{2.3}$$

$$\sin(\theta) = \frac{-(x - x_c)\cos(\phi) - (y - y_c)\sin(\phi)}{R\cos(i)} \tag{2.4}$$

Substituting Equation 2.3 into Equation 2.2 gives the full tilted-ring model. The left side of the Equation 2.2 comes directly from the data; they are the line-of-sight spectra of each annulus otherwise known as the velocity field. While the right side describes the geometry of the galaxy; its inclination, position angle, dynamic center, systemic velocity, and circular velocity for each annulus of the model.

Begeman (1989) outlines his algorithm as follows. First, reasonable initial parameters for V_{sys}, ϕ, i, x_c, and y_c are obtained. There are many ways this can be done. Some methods include (but are not limited to) fitting ellipses to isophotes of constant brightness using the IRAF software package. Knowledge of radio nuclear sources within galaxies can be used as an initial center estimation (Trachternach et al. 2008), as radio nuclear sources are associated with a compact object and should be at the center of the potential well of the galaxy. The dynamic center has also been estimated by fitting ellipses to 3.6 μm data because this emission traces old stellar populations and provides a dust free view of the stellar component (Oh et al. 2008; Trachternach et al. 2008). Old star clusters should have had enough time to be drawn to the center of the potential well of the galaxy. The photometric center is a good approximation of the dynamic center for distant galaxies (Weldrake et al., 2003).

Consider a galaxy where the dynamic and optical centers are not at the same location. The angular separation between these centers decrease as the distance to the galaxy increases. Combined with the spatial resolution of instruments; these two centers will appear to converge. However when considering our sample of dwarf galaxies, which are both low mass and at distances of a few Mpc, these basic approaches for obtaining the initial estimates of the tilted ring parameters are not sufficient. This is a major motivation for this work.

The set of parameters define the annuli. For each annulus, a least-squares fit is made with the above parameters against the velocity field defined by the initial parameters. The model parameters are then allowed to vary and the least-squares fit is made with the initial velocity field. If the results of these least-squares fits provide improved values of the model parameters (by minimizing the χ^2 of the fit) then these new values for the model parameters are taken as a new initial estimate and sent through the algorithm again. This is an iterative process which is repeated until convergence to a set of model parameters is reached. Each annulus is required to have at least thirty velocity measurements (spectra) in order to have a meaningful fit (Begeman, 1989).

Three of the model parameters should be considered 'global' parameters; they do not change throughout the galaxy disk. These parameters are the location of the dynamic center, x_c and y_c, and the systemic velocity of the galaxy, V_{sys}. Since the algorithm predicts all of the model parameters for each ring independently, these three parameters must be consistent throughout the galaxy disc. In fact, looking at Equations 2.2 and 2.3, there must be some symmetry to the velocity field because θ determines the sign of V_{rad}.

Observationally, the orientation parameters (ϕ and i) vary with radius. Warping of galaxy disks occurs in the outer radii of most galaxies with strong rotation (van der Kruit & Freeman, 2011). Warping should be thought of as the systemic deviation

of the matter distribution from equatorial symmetry (Corbelli et al. 2010). Its effects are seen as a systematic change of ϕ and i along the major and minor axis (Rogstad et al. 1974). However, V_{sys}, x_c and y_c must be known to a high degree of certainty before finding $\phi(R)$ and $i(R)$. A way to obtain these global model parameters using the tilted ring model is to run the algorithm keeping the orientation parameters fixed. Keeping the orientation parameters constant define the plane of the galaxy (this is the plane which θ is measured). This will determine the best dynamic center and the system velocity for each ring (Begeman, 1989). These estimates of V_{sys}, x_c and y_c for each ring are then averaged (Trachternach et al., 2008). Then the algorithm is run again but this time fixing V_{sys}, x_c and y_c to the values just found and not fixing the orientation parameters. This finds $\phi(R)$ and $i(R)$. In total the algorithm is run two times on a single galaxy, first to establish the global parameters then again to determining the warp of the galaxy disk (Begeman, 1989).

Another approach to the algorithm exploits the symmetry of the velocity field. Since V_{sys} and (x_c, y_c) are known, the remaining parameters can be found by using the algorithm on the approaching and receding sides of the galaxy separately. This is a check for symmetry (Begeman, 1989).

The above is an automatic algorithm, with exception of the initial estimates of model parameters. Again, with the advent of ASKAP and the WALLABY survey observing hundreds of thousands of galaxies and providing the community with Hı data cubes (Duffy et al. 2012), a fully automated algorithm is greatly needed.

<center>Implementation of the Tilted Ring Model</center>

In this work, the tilted ring model is tested by a more rigorous approach. V_{sys} is determined outside of the model (see below). Using independent measurements of V_{sys} will serve as a consistency check to ensure the final fit parameters are physically meaningful. For each galaxy, two annuli are selected, an inner and outer annulus.

<center>12</center>

The tilted ring model is applied to these annuli by simply varying the center and orientation parameters until the algorithm finds a V_c where the RMS is minimized (see Equation 2.11). This lets the tilted-ring model determine the best set of model parameters from the observed dynamics. The focus of this work is investigating how accurately these model parameters, specifically the dynamical center, can be determined using the tilted ring model with minimal human intervention. Since we are interested in the central regions of galaxies, the rotation curves generated here will have the orientation parameters, ϕ and i fixed.

We now discuss how the radial velocity is extracted from each line-of-sight spectrum ($V_{rad}(x, y)$). A radio telescope array measures $I_\nu(\alpha, \delta)$ within a beam area of the sky. In HI radio astronomy, the frequency of radiation received by the telescope or array is reported in units of velocity. This is because the rest frame emitted frequency is known to fairly high accuracy: ν_{em}=1420.4 MHz which corresponds to λ_{em}=21.106 cm and E_{em}=5.8743 $\times$ 10^{-6} eV (Essen et al. 1971). Laboratory hydrogen masers have exhibited drifts in this frequency of less than one part in 10^{13} over a period of 12 hours (Storey et al., 1994). Therefore, in the non-relativistic limit ($V_{rad} \ll c$) a corresponding redshift velocity can be calculated directly with:

$$V_{rad} = \left(\frac{\nu_{em} - \nu_{obs}}{\nu_{em}} \right) c \qquad (2.5)$$

These velocities have little physical meaning unless $V_{rad} \ll c$. If not, the use of the full relativistic expression is required (Roelfsema, 1989).

Intensity Weighted Method

There are various methods of extracting a velocity measurement from a spectrum. We focus on the intensity weighted method. The intensity weighted method uses the specific intensity (or Jansky beam^{-1}) of each velocity channel and performs a simple weighted average among those velocity channels. The velocity is extracted from the

spectrum as follows:

$$V_{rad,IW}(x,y) \; = \; \frac{\sum (\, I(v_{ch}) \, \times \, v_{ch} \,)}{\sum I(v_{ch})} \qquad (2.6)$$

v_{ch} is the velocity channel and $I(v_{ch})$ is the specific flux density, or pixel value.

Modified Envelope Tracing Method

Another method used in this work is the Modified Envelope Tracing method (MET) (Gentile et al., 2004). The idea is simple, only the extreme side of the line-of-sight spectrum is considered. The extreme side of the spectrum is the side opposite the system velocity. Then a half Gaussian is fit to the extreme side of the spectrum. The half maximum of this is taken to be the terminal velocity for that line-of-sight. This is done instead of taking the peak of the half Gaussian because each line-of-sight spectra is sampling multiple radii for a disk of finite thickness; these projection effects are unavoidable. This contamination due to the unwanted annuli, will result in more emission at velocities towards the systemic velocity.

There are additional effects which broaden the line-of-sight spectrum which need to be taken into account in order for the half maximum value to have physical meaning.

$$V_{rad,MET}(x,y) \; = \; V_{HM} \pm V_{broad} \qquad (2.7)$$

The sign of the correction depends on which side of the spectrum is the extreme side. If the extreme side is the red side, then the correction is added. If the extreme side is the blue side then the correction is subtracted. In either case it can be regarded as a 'pull back' of the velocity towards the system velocity. Corrections are given in terms of FWHM; the correction is halved after adding in quadrature. The correction

is given by:

$$V_{broad} \;\; = \;\; 0.5\sqrt{(\delta V_{ISM})^2 + (\delta V_{obs})^2} \tag{2.8}$$

There are two broadening effects which are taken into account. The first is δV_{ISM} with is broadening due to turbulence of the interstellar medium. Which is found by assuming a constant velocity dispersion.

$$\delta V_{ISM} \;\; = \;\; \sigma_{ISM}\sqrt{8\ln 2} \tag{2.9}$$

This work adopts a velocity dispersion of 8 km s^{-1}. A typical spiral galaxy has a velocity dispersion of 10 km s^{-1}. Work done by Kamphuis (1993) shows the velocity dispersion to be between 7 and 12 km s^{-1} does not significantly affect derived rotation curves for a collection of spiral galaxies.

The second broadening effect is due to the spectral resolution of the instrument used to collect the data. The data used in this work were gathered at the Very Large Array (VLA), which has a spectral resolution of 5.2 km s^{-1}.

Figure 5 illustrates these effects. In this case, the spectrum shows the contamination due to projection effects on the high velocity (red) side of the spectrum. A Gaussian is fit to the blue side of the spectrum and the 'pull back' is applied at the half maximum. However, this method may have trouble with emission profiles which have a small FWHM; the 'pull back' may be too large for those cases.

Using these methods, velocities can be measured at each location within the galaxy. For a given annulus containing sky positions, the predicted velocity field can be calculated at each location using the model parameters from Equation 2.2. The velocity field for an annulus changes if any of the model parameters change because they define new annuli. To determine $V_c(R)$ for a particular ring, a linear least-squares fit of Equation 2.2 (the predicted velocity field for the annulus) with

the extracted velocity field is performed (the velocity field observed in the annulus). This is done using plots of $\cos(\theta)(x,y)$ vs. $V_{rad}(x,y)$ and fitting Equation 2.2 to the extracted velocity field. The fitting function is:

$$V_{extr}(x,y) \quad = \quad a + b\cos(\theta) \qquad\qquad (2.10)$$

Figure 6 shows an example of the fit for an annulus in dwarf galaxy DDO 154. The zero-intercept, or a-parameter, of the fit corresponds to the V_{sys}. The slope, or b-parameter, corresponds to $V_c(R)\sin(i)$ as these parameters are coupled. Then the variance of the root mean squared values between the data and the linear fit based on the relationship between the velocity of the particles and the cosine of the angle within the galaxy is calculated. The RMS between the predicted and extracted velocity fields are calculated by:

$$\text{RMS}(R) \quad = \quad \sqrt{\frac{\sum[\ (V_{extr}(x,y) - V_{fit})^2\ ]}{n_{anu}}} \qquad\qquad (2.11)$$

where $V_{extr}(x,y)$ is the velocity field extracted from the data, V_{fit} is the velocity calculated using the model parameters and fitting Equation 2.2 (b-parameter), and n_{anu} is the number of sky positions in the annulus. We seek the lowest RMS by varying the model parameters. The χ^2 minimized in other work are equivalent to Equation 2.11 except for a simple numerical factor in front; minimizing either equation is essentially equivalent (Corbelli et al. 2010). Now there is a V_c for every R; the rotation curve is found.

The fit provides an estimate of portions of the radial velocity field which are due to the rotational motion of the gas on an inclined disk. This couples V_c and inclination angle. The derived slope needs to be corrected for the inclination of the galaxy. The slope parameter includes a $\sin(i)$ term. This can be seen by inspecting Equation 2.2 and 2.10. So, changing i define different annuli, which then of course changes the

$V_{rad}(x, y)$ for each annulus. $\text{Cos}(\theta)$ depends on ϕ and (x_c, y_c), so changing these values will change the θ of each sky position. This will change the results of the least-squares fit.

Investigation of $\cos(\theta)$ weighting schemes have been done to see what effect this has on the fits (Weldrake et al., 2003). Since the only information available is radial component of velocity, it follows that gas near the major axis of the galaxy has more rotational information. Here, the motion of the gas is mostly towards or away from the observer. Data near the minor axis carry less information because there the motion of the gas lacks radial motion. The overall inclination of a galaxy also affects the quality of the derived rotation curve. For a face on galaxy, all of the rotation information is suppressed and the radial velocity measures the turbulence of the ISM.

Signal to Noise Requirements

We only accepted data above a signal to noise of 2.5. The noise level is determined using the `imexam` task from the IRAF software package. The procedure goes as follows: six 35×35 pixel boxes containing only noise were sampled. The RMS of the pixel values inside the pixel box were calculated. These values are then averaged to give an estimate of the noise within that velocity channel. This process is applied to six velocity channels which are evenly spaced in velocity-space. σ is taken to be the mean of these six values collected from the velocity channels and are reported on Table 6. The noise level adopted for this work is 2.5σ; pixels with values under this threshold are ignored. Furthermore, spurious pixels are eliminated by ensuring emission spreads to at least three consecutive velocity channels.

System Velocity Determination

Global HI profiles can be generated by finding the flux density in each velocity channel (see Appendix A). The HI profile is a spectrum of the emission from the entire

17

galaxy. For galactic discs, the emission peaks on the extreme velocity sides of the galaxy (see Figure 7). This effect is due to the rotation of the galaxy. In these plots one can disentangle the systemic and rotational velocity components of Equation 2.2. The entire galaxy spectrum is redshifted due to its systemic velocity, then the emission is spread out due to the rotation of the gas within the galaxy. The systemic velocity can be estimated from the Global H I profiles. This is done by averaging the velocities on each side of the spectrum corresponding to 20% of the peak level. The uncertainty of this measurement is equal to the width of the velocity channel. This procedure was carried out by Walter et al. (2008) on all of the THINGS galaxies. The precision of this method was tested by comparing the results with the heliocentric velocities derived by Fisher & Tully (1981). They found excellent agreement with Fisher & Tully's results. Therefore, this is a method of finding V_{sys}.

Since V_{sys} can be found independent of the model, it can be used to determine if the tilted-ring model is providing physically meaningful results. As stated earlier, the a-parameter of the fit is analogous to V_{sys}; the reliability of a fit can be quantified by how low the quantity $|a - V_{sys}|$ becomes. V_{sys} and the a-parameter should be consistent. This adds an additional criterion to determining the correct dynamic centers of galaxies besides minimizing the RMS. Oftentimes, the minimization of RMS alone will only drive the dynamic center to an unrealistic location with a system velocity greater than found from the H I profile.

CHAPTER 3

N-BODY MODEL

An N-body simulation of an exponential disc galaxy is used to check the results of the 'brute force' version of the algorithm (see previous section). The model's center, inclination angle (i), position angle (ϕ), and rotation curve are known in advance. The program is tested by seeing how accurately these parameters can be recovered.

This work uses model IV from Rhee et al. (2004), which is a thin disc embedded in an NFW halo potential with a high concentration. First the virial mass needs to be defined. It is defined as follows:

$$M_{vir} \;=\; \frac{4\pi}{3}\, r_{vir}^3\, \rho_{cr}\, \Omega_0\, \delta_{th} \tag{3.1}$$

where M_{vir} and r_{vir} are the virial mass and radius. ρ_{cr} is the critical density to close the universe and δ_{th} is the over density of a collapsed object in the "top-hat" collapse model. The simulation assumes a current mass density of $\Omega_{m,o} = 0.3$ and assumes $H_o = 70$ km s^{-1} Mpc^{-1}. A requirement for a collapsed object is it must have M_{vir} within a sphere of size $\frac{4\pi}{3}\, r_{vir}^3$ with a density of $(\rho_{cr}\, \Omega_0\, \delta_{th})$.

The NFW profile is defined by the following equations (Klypin et al. 2002; Rhee et al. 2004; Navarro et al. 1997):

$$\rho_{NFW}(r) \;=\; \frac{\rho_s}{x\,(1+x)^2} \tag{3.2}$$

$$C \;\equiv\; \frac{r_{vir}}{r_s}, \; x \equiv \frac{r}{r_s} \tag{3.3}$$

$$M_{halo}(<r) \;=\; 4\pi\, r_s^3\, \rho_s\, f_{NFW}(x) \tag{3.4}$$

$$f_{NFW}(x) \;\equiv\; \ln(1+x) - \frac{x}{1+x} \tag{3.5}$$

$$M_{halo}(<r) \;=\; M_{vir} \times \frac{f_{NFW}(x)}{f_{NFW}(C)} \tag{3.6}$$

where M_{vir} and r_{vir} are the virial mass and radius. r_s is the scale radius of the halo (not the scale radius of the disc). ρ_s is the scale density representing the density at a location r_s from the center of the galaxy. C is the halo concentration parameter. C is a measure of the concentration of dark matter particles within the halo, or the ratio of the virial radius and scale radius. $\rho_{NFW}(r)$ is the density profile. This is integrated over a volume to obtain the mass of the halo within r, $M_{halo}(< r)$. $f(x)$ is the result of this integration. It describes how the mass of the dark matter particles in the halo changes as a function of radius. This function corresponds to a spherical halo model. Two independent parameters, M_{vir} and C, along with the parameterization of x is all that is required to describe the halo (see Equation 3.6 and Appendix C for more information).

From the equations one can find the circular velocity as a function of radius, aka the rotation curve, for a halo with mass M_{vir} and concentration C. The final relationship comes from balancing the centripetal and gravitational forces:

$$V_c(r) \;=\; \sqrt{\frac{G\,M_{halo}(< r)}{r}} \tag{3.7}$$

$$=\; \sqrt{\frac{G\,M_{vir}}{r} \times \frac{f_{NFW}(x)}{f_{NFW}(C)}} \tag{3.8}$$

The Adaptive Refinement Tree (ART) N-body code was used to run the simulation (Kravtsov et al. 1997; Kravtsov 1999). The relevant model parameters are shown in Table 1. The model consists of 1.6×10^6 particles in total. There are no stellar or gaseous components to the model, just a dark matter halo and disk component. The model was run for 1.6 Gyr to ensure the final state of the disk was in dynamic equilibrium. Figure 8 shows the galaxy model in four different orientations: face-on, edge-on, position angle 48° with inclination angle 65°, and position angle 300° with inclination angle 42°.

The N-body data consist of a list of three spatial positions $(x,\ y,\ z)$ and three

velocity components (v_x, v_y, v_z) for each particle in the model. Knowing these, the disk can be reoriented to a specific inclination and position angle. With the new orientation, the velocity vector of each particle is projected along the line of sight to obtain the radial component. This is an important step as the frequency of radiation seen from the galaxy is determined by the component of the particle motion along the line of sight.

Creating a mock observation is straightforward. After the orientation change and the projection of the velocity vectors, we generate a cube of data with components (x', y', v_{rad}). These are the new positions of the particles in the model projected onto the "sky" along with the radial velocity of the particles. Additional code was written to place each particle in pixel bins and subsequent radial velocity bins of same spatial and spectral widths as the VLA and then convert the particle density in each position and velocity bin into a surface brightness measurement for each line of sight. The data are then smoothed to mimic the resolution of VLA radio data. This was done using a Gaussian function with care to ensure the number of particles is preserved. The data are first spread to the adjacent position pixels (x, y) in a bivariate Gaussian function creating a 9 x 9 grid of emission. Then each position pixel is spread to the adjacent velocity channels (v_{rad}) with a standard two dimensional Gaussian function, again ensuring the pixel value is preserved. This spreads the emission into three velocity channels in total; a requirement of the real data cubes. Then the data are converted to a FITS file. The N-body model now has a known center, position angle, and inclination angle. Four FITS files generated this way are shown in Figure 8. In addition, the Global Hɪ profiles and IW velocity maps of the simulated galaxy in two orientations are shown in Figure 9. Notice the 'double horned' feature on the receding and approaching sides of the Global Hɪ spectrum. This indicates internal rotation within the galaxy. The piling up of particles at the red and blue sides are a signature of a flat rotation curve. Now the FITS files are ready to be analyzed with our version

of the tilted ring algorithm.

The objective was to have the program search the ϕ, i, x_c, y_c parameter space of a single annulus to see how accurately we could recover the correct values by choosing the set of parameters with the lowest RMS deviations from the least-squares fit. 49 centers were included in the parameter space, each spaced about 0.25 kpc apart (the simulated galaxy is 'located' about 4 Mpc away). The search includes the N-body model in two orientations and is shown in panel a of Figures 10 and 13. The two methods used to extract a velocity from each spectrum are the traditional Intensity Weighted (IW) method and the Modified-Envelope-Tracing (MET) method. The latter is designed to correct for projection effects. We then calculate the variance of the root mean squared values between the data and the linear fit based on the relationship between the velocity of the particles and the cosine of the angle within the galactic plane. This generates two contour maps for each galactic center, one for each velocity extraction method, sampling the RMS for all possible position and inclination angles.

The results for orientation 1 are shown in Figures 10 through 12. Panel b of Figure 10 show the orientation parameters corresponding to the ten lowest RMS_{IW}, while panel c shows the center locations for those orientation parameters. Figure 11 shows contour plots of RMS for the ϕ and i parameter space. The first two plots are for the 3.03 kpc annulus, IW and MET respectively. The last two plots are for a 1.01 kpc annulus, again, IW and MET respectively. Table 2 shows the best collections of center, position angle, and inclination angle corresponding to the lowest RMS for each method/annulus for comparison with the known orientation parameters and center. The algorithm correctly recovers the dynamic center, recovers ϕ with better than $1°$ accuracy, and recovers i with better than $4°$ accuracy.

The results for orientation 2 are shown in Figures 13 through 15. Panel b of Figure 13 show the orientation parameters corresponding to the ten lowest RMS_{IW}, while

panel c shows the center locations for those orientation parameters. Figure 14 are contour plots of RMS for the ϕ and i parameter space. The first two plots are for the 3.03 kpc annulus, IW and MET respectively. The last two plots are for a 1.01 kpc annulus, again, IW and MET respectively. Table 3 shows the best collections of center, position angle, and inclination angle corresponding to the lowest RMS for each method/annulus for comparison with the known orientation parameters and center. The algorithm correctly recovers the dynamic center, recovers ϕ with better than 2° accuracy, and recovers i with better than 10° accuracy. It is interesting to note the difficulty of determining the inclination angle.

In each orientation the contour plots show a clear convergence onto the correct values, although the algorithm overestimated the inclination for orientation #2. Also, the algorithm recovered the correct values more precisely using a larger annulus. This shows that even with moderate galactic broadening due the the finite thickness of the disc, the original center and orientation parameters can be found using this method. The symmetry of these plots will vanish when moving to observed galaxies which contain a higher percentage of random motions than this model and less complete spatial H I coverage. Also, it it worth noting that if the position angle drifts away from the correct value the RMS will quickly increase. The uncertainties in inclination angle are larger than those for position angle.

Rotation curves can be generated for a single collection of x_c, y_c, ϕ, and i. This was done for the N-body model in orientation 1. Figure 16 panel a shows a rotation curve for parameters corresponding to the lowest RMS obtained for the 3.03 kpc annulus (first two rows of Table 2). The red points correspond to the IW method and the blue points correspond to the MET method. The rotation curve for the true parameters are superimposed on top of these curves as open circles. Figure 16 panel b shows a rotation curve for parameters corresponding to the lowest RMS obtained for the 1.01 kpc annulus (last two rows of Table 2). Again, the red points correspond to the IW

method and the blue points correspond to the MET method. The rotation curve for the true parameters are again superimposed on top of these curves as open circles. In addition, the theoretical NFW model (Equation 3.8) showing the true circular velocity is also plotted (see Table 1 for NFW model parameters). It is interesting to see the MET routine underestimates the true rotation curve by 5-15 km s^{-1} from 2 kpc to the edge of the galaxy. It is worth pointing out the difference between the true and best parameters for the IW method from the 1.01 kpc annulus. The main difference between the two rotation curves is that i is only off by 5°, but this seems to affect the rotation curve little. It overestimates the rotation curve with the true parameters by less than 1 km s^{-1}, and possibly agrees better with the true rotation curve derived from the NFW model.

Figure 17 shows the effect of shifting the dynamic center by one third of a kiloparsec. The red points correspond to a shift along the major axis towards to receding (red) side of the galaxy and the blue points correspond a shift along the major axis towards to approaching (blue) side of the galaxy. The open circles correspond to the true orientation parameters and dynamic center for the galaxy. The up triangles correspond to a shift along the minor axis towards the northern side of the galaxy, while the down triangles correspond to a shift along the minor axis towards the southern side of the galaxy. Again, the true rotation curve from the NFW model is plotted for perspective. Error bars were left off for ease of reading, but are about ± 5 km s^{-1} in the outer radii.

Immediately, one can see the shape of the rotation curves with incorrect centers have a different shape than the correct rotation curve. In the inner 2 kpc of the galaxy, shifting the dynamic center along the major axis causes the rotation curve to be overestimated. Shifting the dynamic center along the minor axis cases the rotation curve to agree with the true rotation curve; these results on the minor axes represent degenerate models. These are models which happen to track along the

rotation of the galaxy, but are not anchored at the correct location. Interestingly, the true parameters underestimate the true rotation curve. This has been seen in the literature (Rhee et al., 2004). At around 2 kpc to 4 kpc the rotation curves derived from incorrect centers all begin to overlap nicely and are around 5 km s^{-1} below the true rotation curve. While the rotation curve for the true parameters continues to increase (with the theoretical model). However, at large radii the rotation curves with incorrect centers have greatly underestimated the true rotation curve by about 8-10 km s^{-1}. This is greatly significant as deviations from the true parameters and true rotation curve are around 2-3 km s^{-1}. The rotation curve derived with the shifted centers begin to slightly decrease before 6 kpc whereas the rotation curve derived with the correct center remain steady around 60 km s^{-1}. The rotation curves derived with the correct and incorrect centers begin to become unreliable after 6 kpc because of the poor signal at large radii. This effects both simulated and observed galaxies; the outer edges of a galaxy are where the neutral hydrogen column density is the lowest. This accounts for the rather noisy data points and small populations inside large annuli, which results in larger error bars at these radii. Each spectrum must meet certain requirements in order to extract a reliable velocity; there are more stringent requirements for the MET method compared to the IW method.

For a well-defined galaxy lacking random velocities, the algorithm accurately recovers the original parameters. It finds the correct center and recovers the orientation parameters to some degree using the kinematic motions of the model.

For orientation 1, the position angles are recovered to better than 1° accuracy with both IW and MET methods and for both annuli. The inclination angles are found to 1° accuracy with IW for a 3.03 kpc annulus and better than 5° accuracy for a 1.01 kpc annulus. With MET, the inclination angles are found better than 4° accuracy for a 3.03 kpc annulus and better than 9° accuracy for a 1.01 kpc annulus.

For orientation 2, the position angles are recovered to better than 2° accuracy with

both IW and MET methods and for both annuli. However, the inclination angles are found to 7° accuracy with IW for a 3.03 kpc annulus and better than 9° accuracy for a 1.01 kpc annulus. With MET, the inclination angles are found better than 10° accuracy for a 3.03 kpc annulus and better than 2° accuracy for a 1.01 kpc annulus.

This confirms the code is working correctly. Also, insight is gained as to how changing the dynamic center affects the rotation curve. In addition, using this method has determined the shape of the search area can be modified to eliminate centers along the semi-minor axis towards the outskirts of galaxies (see Figure 10 panel a) as these are not likely to be the locations of the centers. This saves in computational time, as the parameter space of certain centers no longer need to be sampled. Further criteria are applied, the position and inclination angles are not allowed to drift to unphysical values (these were not needed for the N-body model, but application of this criteria can be seen in panel b) of Figures 10 and Figures 13 as the dotted rectangles). The underwhelming performance of the MET method of extracting velocities from the spectra has resulted in sticking with the IW method when shifting to the observed galaxies. The MET method and additional methods of extracting velocities will be investigated in future work.

CHAPTER 4

THE SAMPLE

Our galaxy sample is taken from The H<small>I</small> Nearby Galaxy Survey (THINGS, Walter et al. 2008). This survey done at the Very Large Array (VLA) radio array from Summer 2003 to Summer 2005. This survey was made with a high spatial resolution (6") and high spectral resolution (≤ 5.2 km s^{-1}). The goal of the survey was to obtain high quality observations of the H<small>I</small> distribution of nearby galaxies which cover a wide range of Hubble types, star formation rates, absolute luminosities, and metallicities (Walter et al. 2008). The survey included 34 galaxies from small dwarf galaxies to massive spiral galaxies. Elliptical type galaxies were omitted because they contain minimal amounts of neutral gas.

VLA Configurations B through D were used. The B array configuration (baselines: 210 m to 11.4 km) achieves the high angular resolution and was used to probe the small scale structure of the H<small>I</small> distribution. Array configurations C (baselines: 35 m to 3.4 km) and D (baselines: 35 m to 1.03 km) were used to gather data from the extended emission. Galaxies surveyed were at distances closer than 15 Mpc, and this work mostly focuses on galaxies situated around 5 Mpc with one exception, shown in Table 6. Close galaxies were chosen in order to resolve internal structures on orders of 500 pc. Since the 1σ velocity dispersion of warm neutral medium is 6-7 km s^{-1}, all observations in the survey were done with at least 5 km s^{-1} velocity resolution in order to Nyquist sample the H<small>I</small> line (Walter et al. 2008).

The THINGS data were calibrated with natural weighting (NA) to obtain maps of the highest surface brightness sensitivity and with the ROBUST weighting scheme (RO) (Briggs 1995). The raw data from the THINGS survey calibrated using both schemes are publicly available in the Flexible Image Transport System (FITS) file format. They come in four dimensional cubes of right ascension, α; declination, δ; radial velocity, V_{rad}; and specific flux density per beam, I_i. Every point in the data

cube (x and y) is a point spectrum with V_{ch} corresponding to frequency and the pixel value, I_i, corresponding to the intensity. For this work, the NA data cubes were used.

Five galaxies were selected for this work. They are DDO 154, NGC 2366, IC 2574, NGC 3627 (M 66), and DDO 53. The integrated Hi maps (moment 0) are shown in Figure 18. These maps have been generated after employing the signal to noise requirements outlined above. The spacial resolution of one pixel for each galaxy, in many units and the major/minor axis of the beam are shown in Table 4. Distances to these galaxies were taken from Walter et al. (2008) and are displayed on Table 6 (other values on this table are explained below). The spectral resolution of each velocity channel is listed on Table 5. Here the spectral resolution is converted to frequency and wavelength for perspective. Additionally, the number of velocity channels are listed.

All of the galaxies in this work are dwarf galaxies situated around 4 Mpc from the Galaxy, except NGC 3627. These dwarfs were chosen not only because they are great at probing the dark matter distribution, but they are so close that they can be resolved to subkiloparsec scales. One pixel is about 30 pc (projected) in size! DDO 154 and NGC 2366 are both classified as Im galaxies, irregular galaxies, although they do exhibit rotation and seem to be flattened systems. IC 2574 is classified a Sm galaxy, which means it has a spiral structure but is irregular in appearance. This galaxy exhibits rotation and seems like a flattened system, but has strong random motions within the galaxy disk. DDO 53 is another Im galaxy, the velocity maps indicate some rotation, but the Global Hi maps (see below) indicate little rotation. This is the smallest galaxy is the sample, in both angular and physical size. NGC 3627 is classified a Sb galaxy. It has two prominent spiral arms clearly seen in the Hi map. Despite this galaxy not being a dwarf, it was selected because it has similar angular size as the rest of the galaxies in this work but it twice the distance (9.3 Mpc). How does this affect the performance of the algorithm?

CHAPTER 5

DATA REDUCTION & ANALYSIS

After the NA data cubes for these galaxies were obtained, elimination of spurious pixels and the a noise level was applied as outlined in Chapter 2. Emission is required to be in at least three velocity channels to be acceptable, and each pixel is required to have a S/N of at least 2.5σ.

V_{sys} is extracted from the Global HI profiles by taking the velocity channels on each side of the spectrum at 20% of the peak and averaging them. The uncertainty is equal to the width of a velocity channel. The velocities extracted are in agreement with those reported by Walter et al. (2008) and Fisher & Tully (1981).

The total flux density is calculated by taking the integral of the Global HI profile, or directly by using Equation A.6. Errors in $\mathcal{S}_{HI}$ are dominated by uncertainties in the flux calibration, generally taken to be ten percent. The total flux densities found are in agreement with those published by Walter et al. (2008).

One advantage of working with HI emission is that if self-absorption is neglected (optically thin assumption), then all of the atomic hydrogen in the region are seen. The total flux density can be converted directly into column densities using Equation A.7 and then into HI mass using Equation A.8. The derivation of these are in Appendix B.

$\mathcal{S}_{HI}$, HI mass, V_{sys}, distance, and σ for these galaxies are reported on Table 6.

The objective is to search the ϕ, i, x_c, y_c parameter space of an annulus to see if the algorithm settles on reasonable model parameters indicated by the lowest RMS from the fitting Equation 2.11 to the velocity field. The intensity weighted (IW) method is used for extracting radial velocities from each line of sight spectrum. The orientation parameter space are in increments of one degree. Two separate annuli were investigated for each galaxy (three for DDO 53). The size of annulus, width of annulus, number of centers searched, and the spacing of the centers in both pixel

and projected physical coordinates are shown in Table 7. The two annuli chosen were to investigate which region of galaxies do better at describing the large scale motions. Disk warping is more likely to occur on the outer regions of the galaxy as opposed to the inner regions. However, projection effects are known to make working in these regions difficult. Large annuli contain over a thousand of individual line of sight spectra which causes the computational time to run the algorithm to be 1-2 weeks on average to run. Formal fitting errors are too small to be taken, typically the velocity dispersion within an annulus (represented by the RMS) should be taken as the uncertainty of the measured rotational velocity (de Blok et al. (2008)).

The locations of the centers investigated and the Global H$\textsc{i}$ profiles for these galaxies are located in Figures 19, 23, 27, 31, and 35. The center locations sample the centroid regions and the minor axis (more specifically, regions where radial velocities match V_{sys}) of these galaxies well.

The algorithm draws annuli of radii defined in Table 7 and centers them on each location in panel c and d of the figures listed above for every ϕ and i. A least-squares fit to Equation 2.2 is performed using the radial velocities within the annulus. This gives a circular velocity for an annulus of those parameters. The RMS of this fit calculated using Equation 2.11.

The hope had been that finding the set of parameters which has the lowest RMS would provide reasonable parameters, but in some cases this is not true. The algorithm finds a low RMS with unrealistically large and small inclinations. This is because with large inclinations, the majority of the emission comes from near the major axis. With larger annuli, small inclinations have a similar affect. The annuli become nearly circular and a majority of locations within them are devoid of emission. These annuli will have an artificially low RMS. Additional criteria is needed to narrow the search window to physical results. Limits on the allowable inclination angles were set and shown on Table 8. This was not enough to determine physically motivated

centers. The a fit parameter (see Equation 2.2 and Chapter 2) represents V_{sys}, so they must be in agreement. The allowed boundaries for the quantity $(a - V_{sys})$ is $\pm 1.5 v_{ch}$. These are also listed Table 8.

The results of the center search are shown in the next section.

CHAPTER 6

RESULTS

The algorithm was run as described in previous sections for the annuli shown in Table 7. A table showing the set of parameters which yields the lowest RMS is on Table 10. In addition, the set of parameters from Oh et al. (2011) and Trachternach et al. (2008) were also sent through the algorithm. The results are shown on Table 11. The comparison between these two tables are shown in Table 12. Lists of the twenty best sets of parameters are shown in Tables 13 through 23 with the mean and scatter of the parameters in the captions. Now, the set of parameters corresponding to the ten lowest RMS the annuli in each galaxy are investigated.

DDO 154

DDO 154 is a dwarf galaxy which has a well behaved velocity field. The regions of emission near the system velocity show a well defined minor axis with exception of a slight warp in the outer radii of the galaxy. The results of the run can be seen in Figure 20. The set of parameters for the ten lowest RMS values are displayed in panels b and c, as well as published results from Oh et al. (2011) and Trachternach et al. (2008). Panel d show the best set of parameters found for each annulus and with parameters taken from Trachternach et al. (2008). The $\cos(\theta)$ vs velocity plots for these annuli are found on Figure 22. The centers found from the 3.07 kpc fit are reasonable. Using the 3.07 kpc annulus the algorithm settles on a set of parameters which yields a V_c which is consistent with those found with Trachternach et al. (2008) and Oh et al. (2011) parameters, but the center settled on is about 0.4 kpc away from theirs. The inclination angle recovered is 2° lower and the position angle is 6° lower than their results. It is interesting this does not affect the V_c determined. The RMS found in this work is lower than theirs by about 0.6 km s^{-1}.

However, the 1.07 kpc annulus did not perform as well. The center the algorithm

settled on is at the boundary of the search area, too far away from where the true dynamic center would be. Despite this, the center is on the minor axis of the galaxy. The center is 1 kpc away from the center found in Trachternach et al. (2008). The inclination angle recovered is 9° larger while the position angle was off by only 4°. This led the algorithm to find a V_c which is not consistent with what the algorithm found with their parameters. However, the RMS recovered is much lower than with their parameters, by about 6 km s^{-1}. Figure 20 panel b compares the orientation parameters for the ten best sets of parameters. The smaller annulus is driven to larger inclinations, which allow the fits to contain fewer points. This subsequently allows the RMS to become artificially low. Interestingly, this degenerate result does find position angles better than 4°. The larger annulus finds the inclination angle better than 2° and position angle better than 6°. The position angle being so different is attributed to the slight warping of the galaxy, despite this the algorithm still found a reasonable dynamic center using a larger annulus.

Figure 21 show contour plots of the RMS for the position angle and inclination angle parameter space corresponding to the best dynamic center found for both annuli as well as using the dynamic center reported by Trachternach et al. (2008). The RMS contour plots for the 3.07 kpc annulus are very similar to those obtained for the N-body model (Figures 11 and 14) and show a clear convergence on the orientation parameters reported for both annuli.

<div align="center">NGC 2366</div>

NGC 2366 is a dwarf galaxy with warping present in its velocity field. There is a counterclockwise distortion in the emission near the systemic velocity in which defines a minor axis. The major axis appears to be distorted in the same fashion; therefore this is a warp and not simply random motions. The results of the run can be seen in Figure 24. The set of parameters for the ten lowest RMS values are displayed in panels

b and c, as well as published results from Oh et al. (2011) and Trachternach et al. (2008). The $\cos(\theta)$ vs velocity plots for these annuli are found on Figure 26. Figure 24 panel d show the best set of parameters found for each annulus and with parameters taken from Trachternach et al. (2008). The centers found from the 3.02 kpc fit are reasonable. The orientation parameters were not found so well. Panel b shows the orientation parameters for both annuli were driven to the boundaries of allowed values. However, the 3.02 kpc annulus seems to be tracking along the warp of the velocity field and this is represented by the settling of ϕ around 50° (see Panel d). This position angle is 15° larger than the parameters presented in Trachternach et al. (2008) and Oh et al. (2011). The position angle being so different is attributed to the slight warping of the galaxy, despite this the algorithm still found a reasonable dynamic center using a larger annulus. The center the algorithm found is about 0.5 kpc away from theirs. Despite this, the V_c determined is consistent with the one found with set of parameters from Trachternach et al. (2008) and Oh et al. (2011).

However, the 1.07 kpc annulus did not perform as well. The center the algorithm settled on is on the minor axis but is far away from where the true dynamic center would be and 1 kpc away from the center from Trachternach et al. (2008). The inclination angle and position angle recovered is 10° larger than theirs. The incorrect center affects the measured V_c the algorithm found; it is not consistent with what the algorithm found with their parameters. However, the RMS recovered is lower than with theirs, by about 1 km s^{-1}.

Figure 25 show contour plots of the RMS for the ϕ and i parameter space corresponding to the best dynamic center found for both annuli as well as using the dynamic center reported by Trachternach et al. (2008). The RMS contour plot for the large annulus show a convergence on the orientation parameters reported. The large annulus, for both centers have low points at i greater than 70°. This visibly shows why the algorithm likes large inclinations; it provides an artificially low RMS. For

the 1.09 kpc annulus, both contour plots show the algorithm likes higher orientation parameters.

IC 2574

IC 2574 is a dwarf galaxy which has a velocity field which contain random motions throughout the velocity field. The emission near the systemic velocity show a minor axis with a pronounced bend just north of the centroid of the galaxy. The results of the run can be seen in Figure 28. The set of parameters for the ten lowest RMS values are displayed in panels b and c, as well as published results from Oh et al. (2011) and Trachternach et al. (2008). Panel d show the best set of parameters found for each annulus and with parameters taken from Trachternach et al. (2008). The $\cos(\theta)$ vs velocity plots for these annuli are found on Figure 30. The centers found from the 4.07 kpc fit are on the boundary of the search area. Investigation of Figure 30 shows the $\cos(\theta)$ vs velocity plot for the best annulus and for the set of parameters from Trachternach et al. (2008). The algorithm drove the annulus to the bend in the minor axis and found a location which it could achieve a low RMS, exhibited in panel d of Figure 28 and panel a of Figure 30. This lead to the orientation parameters to be different from published results; the algorithm changed its ϕ to match the random motion, and i increased enough to find a low RMS. The smaller annulus performed better. However, the centers the algorithm settled on are on the edge of the search area but are still near the minor axis. The ϕ recovered agree with published results, but i was again pushed to large values likely because it is there where the RMS is easily artificially lowered.

Using both annuli the algorithm settled on a set of parameters which yield rotational velocities which are consistent with those found with Trachternach et al. (2008) and Oh et al. (2011) parameters; although only because the RMS for their sets of parameters were so large. This galaxy is an example where the algorithm

has a hard time determining the parameters. Galaxies with strong random motions, are difficult for the algorithm to function properly. Methods of extracting the bulk rotation (such as the algorithm presented in Oh et al. (2011)) should be used in cases such as these. The centers the algorithm settled on is about 1.25 kpc and 1 kpc away from theirs using the 4.07 kpc and 2.07 kpc annuli, respectively, and both are on the minor axis.

Figure 29 show contour plots of the RMS for the ϕ and i parameter space corresponding to the best dynamic center found for both annuli as well as using the dynamic center reported by Trachternach et al. (2008). The RMS contour plots are different from those seen in galaxies with well behaved contour plots. Panel a shows a clear convergence to the orientation parameters reported for the 4.07 kpc annulus. One can see how changing ϕ and i to the values reported found a sweet spot in the velocity field. Using the center reported by Trachternach et al. (2008) give RMS contour plots which the lowest contour is 3 km s^{-1} larger than the one using the algorithm. The inclination angles recovered are 7° and 11° larger using the same two annuli. The position angle using the 4.07 kpc annulus differ from their results by 9°. This annulus latched onto the bending mentioned at the start of the paragraph and got as thin as possible (increase i) to find the lowest RMS. Turning to the 2.07 kpc annulus (panels c and d), the algorithm likes very large i, where the annulus is so thin that barely any points are fit in the $\cos(\theta)$ vs velocity plots. There are no clear convergence in either RMS contour plot. The position angle is just 1° shy of their result, despite having a center so far away from their result. The RMS recovered is lower than theirs by about 4 km s^{-1}. It is clear the random motions are throwing off the algorithm.

NGC 3627 is a spiral galaxy which has a well behaved velocity field with a slight warp and two prominent spiral arms. Since this galaxy is physically much larger than the rest of the sample, the velocities recovered are rather large. The regions of emission near the system velocity show a well defined minor axis with a warp. The results of the run can be seen in Figure 32. The set of parameters for the ten lowest RMS values are displayed in panels b and c, as well as published results from Trachternach et al. (2008). Panel d show the best set of parameters found for each annulus and with parameters taken from Trachternach et al. (2008). The $\cos(\theta)$ vs velocity plots for these annuli are found on Figure 34.

The large annulus used with this galaxy is slightly bigger than the one used for IC 2574. This is to catch the spiral arms in the outer regions of the galaxy, where regions of strong emission are. The search area sampled the central regions well but should have extended more into the blue region of the galaxy. Despite this, the algorithm performed well for the 4.17 kpc annulus. The centers recovered are reasonable and they describe the rotation of the galaxy at that radius well. Figure 32 panel d shows that the annulus is catching the slight warp highlighted earlier. Panel b show i recovered are in agreement with published results. ϕ results are in agreement as well, with exception of the deviation from published results of around 3° can be attributed to the slight warping of the galaxy plane.

The 2.01 kpc annulus did not perform as well. The center the algorithm settled on is at the boundary of the search area, too far away from where the true dynamic center would be. Despite this, the center is near the minor axis of the galaxy. Panel b shows the smaller annulus is driven to a larger inclination to achieve an artificially low RMS. Interestingly, this degenerate result does find ϕ which are in agreement with the larger annulus. The larger annulus finds the inclination angle better than 1° and position angle better than 3°. The position angle being slightly off published results

37

is attributed to the slight warping of the galaxy, despite this the algorithm still found a reasonable dynamic center using a larger annulus. Using both annuli the algorithm settled on a set of parameters which yields V_cs which are consistent with those found with Trachternach et al. (2008) parameters; although only because the RMS for their set of parameters were larger than those found in this work by 6 km s^{-1} and 12 km s^{-1} for the 4.17 kpc and 2.01 kpc annuli, respectively.

Figure 33 show contour plots of the RMS for the ϕ and i parameter space corresponding to the best dynamic center found for both annuli as well as using the dynamic center reported by Trachternach et al. (2008). The RMS contour plot for the 4.17 kpc annulus (panel a) shows a clear convergence on the orientation parameters reported, and are similar to those obtained for the N-body model (Figure 11). Panel b show this same plot using the dynamic center reported by Trachternach et al. (2008). It shows the orientation parameters reported from Trachternach et al. (2008) are near the location of the lowest RMS for that center. For the 4.17 kpc annulus, the algorithm settles on a center 0.4 kpc away from theirs and finds position and inclination angles which are lower than theirs by 4° and 3°, respectively. The RMS using this annulus was about 6 km s^{-1} lower than with using their set of parameters. For the 2.01 kpc annulus, the algorithm finds large i to have the lowest RMS. The center found using the 2.01 kpc annulus is about 1.2 kpc away from theirs, but is still on the minor axis. Because of this, the algorithm finds position angle lower than theirs by 4° as well, but finds inclination angle 7° larger than theirs.

DDO 53

DDO 53 is a dwarf galaxy which has a rather strange velocity field. The global H I profile (Figure 35 panel b) show no signs of rotation. The velocity field is not very symmetric but does show a slight rotation. The emission near V_{sys} show a minor axis which is curved. The results of the run can be seen in Figure 36. The set of

parameters for the ten lowest RMS values are displayed in panels b and c, as well as published results from Oh et al. (2011). Panel d show the best set of parameters found for each annulus and with parameters taken from Oh et al. (2011). Three annuli were used with the algorithm because the galaxy is so small. The radius of the annuli are 0.94, 0.78, and 0.55 kpc. The algorithm settled on centers which are along the minor axis and are 0.40 kpc; 0.26 kpc; and 0.48 kpc, respectively, from the center reported in Oh et al. (2011). The centers recovered from the 0.94 and 0.78 kpc annulus are reasonable in that they are near the centroid of the galaxy, near emission of systemic velocity. These annuli track along the regions of strong rotation. The $\cos(\theta)$ vs velocity plots corresponding to the two largest annuli in panel d can be found in Figure 39. The center the algorithm settled on is near the minor axis, too far away from where the true dynamic center would be. Surprisingly, the center is not at the edge of the search area. The $\cos(\theta)$ vs velocity plots for the 0.55 kpc annuli are found on Figure 39. The algorithm has found a nice set of parameters which have an artificially low RMS, ultimately the annulus does not describe the true rotation. Panel b of Figure 36 show the orientation parameters the algorithm found for the annuli. There is agreement with ϕ between the 0.78 kpc annuli, 0.55 kpc annuli, and published results. The 0.94 kpc annulus found ϕ slightly lower than the other two annuli. For all annuli, i was driven to extremely high inclinations resulting in annuli which do not describe the motions of this galaxy, despite the algorithm still founding a reasonable dynamic center using the 0.94 and 0.78 kpc annulus.

The 0.94 kpc annulus found a set of parameters with which the position angle was underestimated by 7° and inclination angle overestimated by 20°. Despite this, the V_c found in this work and with their set of parameters are consistent due to their set of parameters being 1.3 km s^{-1} larger than ours. Figure 37 show contour plots of the RMS for the ϕ and i parameter space corresponding to the best dynamic center found for the 0.94 kpc and 0.78 kpc annuli as well as using the dynamic center reported

by Oh et al. (2011). Figure 38 show the same thing but for the 0.55 kpc annulus. The RMS contour plot for the 0.94 kpc annulus using dynamic center found by the algorithm is shown in panel a of Figure 37. It shows a convergence to the orientation parameters reported. The orientation parameters the algorithm settled on are not in agreement with those reported in Trachternach et al. (2008). Panel b show the results using the dynamic center reported by Trachternach et al. (2008); the lowest RMS in the parameter space is being driven to large inclinations.

The 0.78 kpc annulus found a set of parameters with which the position angle was underestimated by only 2° and inclination angle overestimated by 21°. Despite this, the V_c found in this work and with their set of parameters are consistent due to the RMS using their set of parameters is 0.9 km s^{-1} larger than ours. The RMS contour plot for the 0.78 kpc annulus using dynamic center found by the algorithm is shown in panel c of Figure 37. The RMS contour plot for the large annulus show a convergence on the orientation parameters reported. The orientation parameters the algorithm settled on are not in agreement with those reported in Trachternach et al. (2008). The lowest RMS contours in panel a and c are in agreement. However the orientation parameters of the lowest RMS are slightly different, about 2° difference in ϕ and 4° difference in i. Panel d show the results using the dynamic center reported by Trachternach et al. (2008); the lowest RMS in the parameter space is at large inclinations. A region of low RMS is present and in agreement with panel a.

The 0.55 kpc annulus found a set of parameters with which the position angle was underestimated by 4° and inclination angle overestimated by 23°. The V_c found in this work and with their set of parameters are not consistent, and the RMS found with their set of parameters is 1 km s^{-1} larger than ours. The consistency with the measured V_cs is not surprising because of the coupling of V_c and i. If the slopes (b fit parameter) found with the $\cos(\theta)$ vs velocity plots are different and there are rather large difference in i, then converting the slope to V_c ($V_c = b/\sin(i)$) may make

the final results consistent. The RMS contour plot for the 0.55 kpc annulus using dynamic center found by the algorithm is shown in panel a of Figure 38. The RMS contour plot for the large annulus show a convergence on the orientation parameters reported. The orientation parameters the algorithm settled on are not in agreement with those reported in Trachternach et al. (2008). The lowest RMS contours in panels a and c of Figure 37 are in agreement with the lowest contour region in panel a of Figure 38. However the orientation parameters of the lowest RMS are slightly different, about 2° difference in i. Panel b show the results using the dynamic center reported by Trachternach et al. (2008); the lowest RMS in the parameter space is at large inclinations.

In general, the algorithm does a better job working with larger annuli as opposed to smaller annuli. These annuli are not as susceptible to projection effects and are large enough in order to find the bulk motions of the galaxy. Smaller annuli did a good job at recovering ϕ values which were in agreement with the large annulus (DDO 154, IC 2574 [with published results], NGC 3627, and DDO 53). Larger annuli did a good job at recovering i in galaxies without large quantities of random motions or warps (DDO 154, NGC 3627). The algorithm chooses ϕ which deviate from published results in order to track along warps in galaxy disks (DDO 154 and NGC 3627). From the RMS contour plots, the algorithm prefers to use annuli with large inclinations because they are so thin that there is only emission from locations in the annulus were $\cos(\theta) \approx |1|$, this would give an artificially low RMS. Conversely, some contour plots for large annuli show that low inclination annuli are preferred as well. This is because with these parameters, the annuli will have many locations where there lacks emission. This also give an artificially low RMS. It is interesting to note that the RMSs found with that algorithm are lower than those found using the set of parameters from the literature. When considering the galaxies which reports reasonable center locations, the fact that the orientation parameters deviate from published results

is expected. Once a dynamic center is found, then one can go back and find the orientation parameters with the center fixed.

CHAPTER 7

DISCUSSION & CONCLUSIONS

The ΛCDM cosmology has been very successful at accounting for observations of galaxies on large scales (Mpc and above) but has had trouble reproducing the data on small scales. In particular, the central kpc of dwarf galaxies have been problematic. The theory predicts a rise in dark matter density as one approaches the galaxy center but the data suggest the presence of a constant density core. One key question is the accuracy with which one can measure the density in the central parts of these galaxies. This depends on the tilted-ring analysis and its implementation.

Previous studies have fixed the values of key parameters such as the galaxy center, inclination and position angle to those determined from the outer parts of galaxies. In this study we have let the parameters vary and searched for the which produced the best titled ring model fit to the data. The results show that the shape of the rotation curve in the inner regions is quite sensitive to the values adopted for the galaxy center as illustrated by Figure 17.

We determined the best center for a given annulus by examining a grid of centers separated by 0.25 kpc over a region 2.25 kpc in size. For each center location the parameter space of ϕ and i was searched in order to find the set of parameters which has the lowest RMS deviations. We did this for two annuli, one with a semi-major axis of 1 kpc and one with a semi major axis of 3 kpc. These annuli probe the inner and outer parts of the galaxies.

We began by testing the algorithm using an N-body model of a disk galaxy in an NFW potential. We found that we could recover the model parameters to reasonable accuracy using the tilted ring analysis of the model viewed at various orientations. For the first orientation (ϕ=48, i=65), the algorithm recovered the correct center and inclination angle for the 3 kpc annulus (to within our measuring accuracy). The position angle was recovered to 1° accuracy. At 1 kpc we recovered the correct

center and position angle, but underestimated the inclination angle by 5°. For the galaxy sample, additional criteria were necessary to eliminate parameters that were not plausible. In particular we eliminated centers that gave best fit systemic velocities inconsistent with those determined from spectra of the whole galaxy. This criterion essentially restricts the allowable center to be near the minor axis of the galaxy.

We find that the tilted-ring method is most reliable at large radii. By exploring the whole parameter space we found solutions that have lower RMS than those found by in Trachternach et al. (2008) and Oh et al. (2011). The published results are shown in Table 11, the circular velocities were calculated by using their values of inclination, position angle and center. Our best fit parameters are shown in Table 10. We have shown the difference between our results and the published results in Table 12. The data are in reasonable agreement. At 3 kpc the RMS scatter between our rotation velocities and the published ones is 9.4 km s^{-1} (a fractional error of about 15%). The difference is mostly due to the different galaxy centers that our method selected. The center positions differed by about 0.5 kpc from the published ones. The RMS difference in position angle is 10°. The RMS difference in inclination angle is 6.5°.

In the central kpc the differences between our results and Trachternach et al. (2008) are mostly larger. The inner annulus rotation velocities have an RMS scatter of 6 km s^{-1} (a fractional error of about 30%). The centers differed by about 1 kpc. The differences in position angle is 6°. The inclination angle difference is around 12°. The tilted-ring model produced a better fit to the data in the outer regions (residuals of about 4 km s^{-1}) than the inner regions (residuals of about 6 km s^{-1}).

The key question is how one should estimate the uncertainties in the rotation velocities. We can estimate these by comparing our results with those in the literature as shown above. This suggests that the formal errors in velocity underestimate the true errors as the difficulty in locating the true rotation center introduces additional uncertainty.

Our results make it clear that determining the galaxy center is critical to measuring accurate rotation curves in the centers of galaxies. What is the best way to do this? This work suggests that one needs to do a computer intensive search of parameter space with centers spaced by 0.1 kpc. Future work will focus on developing an implementation of the algorithm that can be automated and sped up to cope with the flood of data anticipated with the WALLABY survey using the Australia Square Kilometer Array Pathfinder. We would also like to compare rotation curve estimates done using the present method with results obtained from measurements of CO gas rotation in the same regions of the galaxies.

The issue is then which approach should be adopted? Should one fix the galaxy parameters based on measurements at large radii, or should one let the parameters vary in the central regions and find the best fit. It is not clear which method is best, but the difference in results from the two methods give a good estimate of the accuracy with which one can measure rotation velocities in the central regions of galaxies. The uncertainty in the rotation speed is one of several factors that determines the accuracy with which one measure the dark matter density in the centers of galaxy. We propose to estimate the complete uncertainty in dark matter measurements in future work.

APPENDIX A

FITS FILES

The raw data from the THINGS survey are publicly available in the Flexible Image Transport System (FITS) file format. This is the standard file format for all of astronomy, endorsed by the IAU in 1982 (Pence et al. 2010). This file format is 'flexible' because it can store an N-dimensional array of world coordinates in pixel coordinates. The FITS file header contains the conversion factors between pixel coordinates to world coordinates. The way to convert between pixel values and world values in the nth dimension is by:

$$X_w = \mathtt{CDELT}n_w^p \left(X_p - \mathtt{CRPIX}n_p\right) + \mathtt{CRVAL}n_w \tag{A.1}$$

where $\mathtt{CDELT}n_w^p$ is the conversion between pixel (p) coordinates and world (w) coordinates. $\mathtt{CRPIX}n_p$ is a pixel location which corresponds to the world coordinate $\mathtt{CRVAL}n_w$. Finally, X_p is the pixel coordinate in question and X_w is the corresponding world coordinate. FITS files are quite powerful because there can be many different physical quantities stored in the different dimensions. For radio data, these data are four dimensional. The first two dimensions are the sky positions, which the world coordinate equivalent is right ascension (α) and declination (δ). The third dimension is the spectral dimension, it records the velocities corresponding to the measured frequencies. Therefore, $\mathtt{CDELT}1_{RA}^{x_{pxl}}$ and $\mathtt{CDELT}2_{DEC}^{y_{pxl}}$ both give the spacial resolution while $\mathtt{CDELT}3_V^{V_{ch}}$ gives the spectral resolution. The final dimension is the pixel brightness, or specific intensity, in units of Jansky per beam. As one can see, Janskys measure the amount of radiation of a specific frequency, as it hits a radio dish with a finite surface area, per second. So every collection of x and y is a point spectrum with V_{ch} corresponding to frequency and the pixel value corresponding to the intensity.

Each individual pixel has a brightness value of units Jansky per beam. In order to obtain a frequency dependent spectral flux density measurement for a pixel (with units of Jansky), the size of the beam in pixels is required. The equation for flux density for any discrete source is as follows:

$$S_{source} = \int I_{source} \, P_n d\Omega \tag{A.2}$$

where S is the flux density of the source, I is the brightness as a function of position over source, P_n is the normalized power pattern of the antenna, and $d\Omega$ is the solid angle element. The beam solid angle, or beamsize, is found by:

$$\Omega_b = \int P_n d\Omega \tag{A.3}$$

The beam used by the VLA is represented by a two dimensional Gaussian function. Then, its beamsize is defined as the FWHM of the beam.

$$\Omega_b = \frac{2\pi}{8 \ln(2)} \, b_{maj} \, b_{min} \tag{A.4}$$

where b_{maj} and b_{min} are the major and minor axis of the beam. One cannot directly use Equation A.2 to find the flux density of a pixel directly. Using Equation A.2 will calculate the flux density within a single beam. However, one needs to be able to calculate the flux density in a single pixel. The flux density from the ith pixel is found by:

$$S_i = I_i \frac{\Omega_{beam}}{\Omega_{pxl}} \tag{A.5}$$

In this case, I_i (the pixel value measured in units of Jansky/beam) is being multiplied by the ratio of the beamsizes in units 'unit beam' and 'pixel,' respectively.

The ratio then has units 'unit beam × pixel^{-1}'. The result, $\mathcal{S}_i$, is the contribution to the overall flux density from the ith pixel, or how many Janskys are coming from the ith pixel.

The total flux density for the entire galaxy, is found by summing $\mathcal{S}_i$ from every pixel and velocity channel:

$$\mathcal{S}_{HI} = \sum \mathcal{S}_i \times \Delta v \tag{A.6}$$

This result is the H$\textsc{i}$ signal in a line-of-sight, in units of Jy km s^{-1}. Δv is the velocity channel width in km s^{-1}. (Note: the total flux density presented in textbooks are typically in units of erg s^{-1} cm^{-2} or Jy Hz, but frequencies are reported in velocities in this line of work.) The total flux densities for the galaxies in the sample are reported in Table 6.

Since H$\textsc{i}$ gas is optically thin to 21-cm radiation, the total flux density is a direct measurement of the amount of neutral hydrogen in the galaxy. The column density can be found with:

$$N(\text{H\textsc{i}}) \quad = \quad 2.784 \times 10^{62} D^2 \, \mathcal{S}_{\text{H\textsc{i}}} \tag{A.7}$$

where D is the distance is measured in Mpc and $N_{H\textsc{i}}$ is the column density measured in cm^{-2}.

The total H$\textsc{i}$ mass is determined as follows:

$$M_{H\textsc{i}} = 2.341 \times 10^5 \, D^2 \, \mathcal{S}_{\text{H\textsc{i}}} \tag{A.8}$$

Where the distance is measured in Mpc and M_{HI}. These two equations are derived in Appendix B. Results for the sample are shown on Table 6.

Hı EMISSION

Hı emission arises from the Zeeman effect. The Zeeman effect splits an energy state into two distinct states due to the presence of an external magnetic field. In atomic hydrogen, the magnetic moment of the electron is coupled to the magnetic field produced by the proton. This causes the hyperfine splitting of the electronic ground state. The spin of the proton and electron can be either parallel (total spin S=1) or antiparallel (total spin S=0). The parallel spin state has a higher energy level and is a triply degenerate state (g_u=3). The antiparallel state is a singlet state (g_ℓ=1).

To the most decimals, laboratory measurements of the hyperfine splitting using hydrogen masers have found ν_{em}=1420.405751766 MHz which corresponds to λ_{em}=21.10611405419 cm and E_{em}=5.874325804963 $\times$ 10^{-6} eV (Essen et al. 1971). Laboratory hydrogen masers have exhibited drifts in this frequency of less than one part in 10^{13} over a period of 12 hours (Storey et al., 1994). The Einstein $A_{u\ell}$ parameter corresponding to this system is 2.88426$\times10^{-15}$ s^{-1}, which is about 9.1 Myr^{-1} (Gould 1994). This means that if a hydrogen atom is in the higher energy state, it will take about 9.1 Myr for it to spontaneously decay to the ground state. Since Hı emission is so prevalent, there must be something stimulating the transition to the lower energy state (and release of the 21-cm photon). Gazing above, the energy splitting of these levels is extremely small. It turns out that CMB photons are energetic enough to stimulate emission and repopulate the hydrogen to the higher energy level!

Relative state populations are given by:

$$\frac{n_u}{n_\ell} = \frac{g_u}{g_\ell} \exp\left(-\frac{h\,\nu_{em}}{k_B\,\mathcal{T}_{exc}}\right) \tag{B.1}$$

Where n are number densities, g are the degeneracies (g = 2S + 1), h is

Planck's constant, k_B is the Maxwell-Boltzmann constant, and $\mathcal{T}_{exc}$ is the excitation temperature. Excitation temperature characterizes the relative importance of emission and absorption. It is often referred to as the spin temperature or kinetic temperature. Using quantities from the 2002 CODATA recommended values of the fundamental physical constants (Mohr & Taylor 2005) and substituting in what is known:

$$\frac{n_u}{n_\ell} = 3 \times \exp\left(-\frac{0.068169\,\text{K}}{\mathcal{T}_{spin}}\right) \tag{B.2}$$

This is an interesting situation. $h\,\nu_{em}/k_B$ for optical lines are around 10^4 K or more, this usually causes the exponential in Equation B.1 to be extremely small (Field 1957). For the hyperfine transitions the opposite is true. Since observed interstellar temperatures range from 10^2 K to 10^4 K, it is safe to assume $\mathcal{T}_{spin} \gg 0.068169$ K. Therefore, the exponential is close to unity:

$$\frac{n_u}{n_\ell} = 3 \times \left(1 - \frac{0.068169\,\text{K}}{\mathcal{T}_{spin}}\right) \tag{B.3}$$

$$\frac{n_u}{n_\ell} \approx 3 \tag{B.4}$$

This shows that at any single time, there are three times as many hydrogen atoms in the parallel spin state compared to the antiparallel spin state. The population inversion is enforced through absorption of CMB photons. Once an atomic hydrogen atom transitions from the higher energy state to the lower energy state, a CMB photon will boost the atom back to the higher energy level. The total atomic hydrogen number density can be found from Equation B.4.

$$n(\text{HI}) = \frac{3}{4}n_u + \frac{1}{4}n_\ell \tag{B.5}$$

From radiative transfer physics, the absorption coefficient (or attenuation

coefficient) is given by the populations in the two levels and the cross sections for absorption and stimulated emission:

$$\kappa_\nu = n_\ell \sigma_{\ell \to u}(\nu) - n_u \sigma_{u \to \ell}(\nu) \tag{B.6}$$

Where κ_ν is the absorption coefficient and σs are the cross sections. A good way to think about this equation is that it represents the net absorption: true absorption minus stimulated emission. Draine (2011) shows that:

$$\sigma_{u \to \ell} = \frac{c^2}{8\pi\nu_{em}^2} A_{u\ell} \varphi_\nu \tag{B.7}$$

$$\sigma_{\ell \to u} = \frac{g_u}{g_\ell} \sigma_{u \to \ell} \tag{B.8}$$

Where φ_ν is the line width profile, which will be taken as a Gaussian velocity distribution. Substituting these into Equation B.6 yield:

$$
\begin{aligned}
\kappa_\nu &= n_\ell \frac{g_u}{g_\ell} \frac{c^2}{8\pi\nu_{em}^2} A_{u\ell} \varphi_\nu \left[1 - \frac{n_u}{n_\ell} \frac{g_\ell}{g_u} \right] & \text{(B.9)} \\
&= n_\ell \frac{g_u}{g_\ell} \frac{\lambda_{em}^2}{8\pi} A_{u\ell} \varphi_\nu \left[1 - \exp\left(-\frac{h\,\nu_{em}}{k_B\,\mathcal{T}_{exc}} \right) \right] & \text{(B.10)} \\
&= n_\ell \frac{g_u}{g_\ell} \frac{\lambda_{em}^2}{8\pi} A_{u\ell} \varphi_\nu \left[1 - \left(1 - \frac{h\,\nu_{em}}{k_B\,\mathcal{T}_{exc}} \right) \right] & \text{(B.11)} \\
&= n_\ell \frac{g_u}{g_\ell} \frac{\lambda_{em}^2}{8\pi} A_{u\ell} \varphi_\nu \left[\frac{h\,c}{\lambda_{em} k_B\,\mathcal{T}_{exc}} \right] & \text{(B.12)} \\
&= n_\ell \frac{g_u}{g_\ell} \frac{h\,c\,\lambda_{em}}{8\pi k_B} A_{u\ell} \mathcal{T}_{exc}^{-1} \varphi_\nu & \text{(B.13)} \\
&= \frac{3h\,c\,\lambda_{em}}{32\pi k_B} A_{u\ell}\, n(\text{HI})\, \mathcal{T}_{exc}^{-1} \varphi_\nu & \text{(B.14)}
\end{aligned}
$$

Here, Equation B.1 is substituted to obtain Equation B.10. Earlier we showed the exponential is near unity, so it can be approximated as shown in Equation B.11. Equation B.5 and the degeneracies are substituted into Equation B.14. One can see that $\kappa_\nu \propto \mathcal{T}_{exc}^{-1}$ (ignoring φ_ν for a moment). κ_ν decreases as the spin temperature

increases, which can be interpreted as a decrease in net absorption.

A Maxwellian velocity distribution is assumed.

$$\kappa_\nu = \frac{3h\,c\,\lambda_{em}}{32\pi k_B}\,A_{u\ell}\,n(\text{HI})\,\mathcal{T}_{exc}^{-1}\left[\frac{1}{\sqrt{2\pi}}\frac{c}{\nu_{em}}\frac{1}{\sigma_V}\exp\left(-\frac{u^2}{2\sigma_V^2}\right)\right] \tag{B.15}$$

$$= \frac{3}{\sqrt{32\pi}}\frac{1}{\sqrt{2\pi}}\frac{hc\lambda_{em}^2}{k_B}\,A_{u\ell}\,n(\text{HI})\,\mathcal{T}_{exc}^{-1}\,\sigma_V^{-1}\exp\left(-\frac{u^2}{2\sigma_V^2}\right) \tag{B.16}$$

Where σ_V is the velocity dispersion in km s^{-1} and u is the mean of the Gaussian. Plugging in values from above the absorption coefficient is found:

$$\kappa_\nu = 2.201\times10^{-19}\text{cm}^2\,n(\text{HI})\,\frac{\text{K}}{\mathcal{T}_{exc}}\frac{\text{km s}^{-1}}{\sigma_V}\exp\left(-\frac{u^2}{2\sigma_V^2}\right) \tag{B.17}$$

This is related to the optical depth by:

$$d\tau_\nu = \kappa_\nu ds = 2.201\times10^{-19}\text{cm}^2\,n(\text{HI})\,\frac{\text{K}}{\mathcal{T}_{exc}}\frac{\text{km s}^{-1}}{\sigma_V}\exp\left(-\frac{u^2}{2\sigma_V^2}\right)ds \tag{B.18}$$

The column number density is defined as being:

$$N(\text{HI}) \equiv \int n(\text{HI})\,ds \tag{B.19}$$

Which allows for the integration of both sides of Equation B.18 and finding the optical depth for the 21 cm line.

$$\tau_\nu = 2.201\times10^{-19}\text{cm}^2\,N(\text{HI})\,\frac{\text{K}}{\mathcal{T}_{exc}}\frac{\text{km s}^{-1}}{\sigma_V}\exp\left(-\frac{u^2}{2\sigma_V^2}\right) \tag{B.20}$$

The optical depth is extremely small, and decreases with increasing $\mathcal{T}_{exc}$ or σ_V. Therefore, 21-cm radiation is optically thin; absorption is negligible. This changes

the radiative transfer equation to:

$$dI_\nu = -I_\nu \kappa_\nu \, ds + j_\nu \, ds \tag{B.21}$$

$$= j_\nu ds \tag{B.22}$$

The specific emissivity for randomly orientated emitters is:

$$j_\nu = n_u \frac{A_{u\ell}}{4\pi} h\nu_{em}\varphi_\nu \tag{B.23}$$

In terms of the total HI number density:

$$j_\nu = n(\text{HI})\frac{3A_{u\ell}}{16\pi} h\nu_{em}\varphi_\nu \tag{B.24}$$

Substituting this into Equation B.22 and integrating:

$$\int dI_\nu = \frac{3A_{u\ell}}{16\pi} h\nu_{em}\varphi_\nu \int n(\text{HI}) ds \tag{B.25}$$

$$I_\nu - I_\nu(0) = \frac{3A_{u\ell}}{16\pi} h\nu_{em}N(\text{HI})\varphi_\nu \tag{B.26}$$

Now integrating over frequency-space (and normalizing, $\int \varphi_\nu d\nu = 1$):

$$\int (I_\nu - I_\nu(0)) \, d\nu = \frac{3A_{u\ell}}{16\pi} h\nu_{em}N(\text{HI}) \int \varphi_\nu d\nu \tag{B.27}$$

$$= \frac{3A_{u\ell}}{16\pi} h\nu_{em}N(\text{HI}) \tag{B.28}$$

The left side of the equation is related to both the flux density at the observer and the square of the distance to the source. Changing the integration variable using $d\nu = d\nu_{obs}(1 + z)$, and substituting in Equation A.6. Since HI emission is optically thin, the flux density from the source is a direct measurement of the column number

density of atomic hydrogen in cm^{-2}:

$$N(\text{Hi}) = \frac{16\pi}{3} \frac{1}{A_{u\ell} \, h \, \nu_{em}} (1+z) D^2 \int \mathcal{F}_\nu d\nu_{obs} \tag{B.29}$$

$$N(\text{Hi}) = 2.784 \times 10^{62} \, (1+z) \left(\frac{D}{\text{Mpc}}\right)^2 \left(\frac{\mathcal{S}_{HI}}{\text{Jy km s}^{-1}}\right) \tag{B.30}$$

Since the amount of hydrogen atoms in the signal are known, it can then be converted directly into Hi mass:

$$M(\text{Hi}) = \frac{16\pi}{3} \frac{m_H}{A_{u\ell} \, h \, \nu_{em}} (1+z) D^2 \mathcal{S}_{HI} \tag{B.31}$$

$$M(\text{Hi}) = 2.341 \times 10^5 \text{M}_\odot \, (1+z) \left(\frac{D}{\text{Mpc}}\right)^2 \left(\frac{\mathcal{S}_{HI}}{\text{Jy km s}^{-1}}\right) \tag{B.32}$$

In the low-z universe, the $(1+z)$ term can be dropped, leaving the same result as Equation A.8.

APPENDIX C

HALO MASS MODELS

In Chapter 3, the NFW halo density profile was introduced. The pseudo isothermal core (ISO) profile, which is traditionally used, and the Einasto profile were mentioned in the Introduction. An overview of these three density profiles is given in this appendix. A description of the density profile for the dark matter distribution is essential because it determines the contribution it has to the overall rotation curve. Remember Equation 3.7:

$$V_c(r) = \sqrt{\frac{G\,M_{halo}(<r)}{r}} \tag{C.1}$$

The mass within radius r comes from integrating the density equation using one of the various density profiles. The key parameter is the virial mass, which is defined as:

$$M_{vir} = \frac{4\pi}{3}\,r_{vir}^3\,\rho_{cr}\,\Omega_0\,\delta_{th} \tag{C.2}$$

NFW Halo Model

We characterize the density as a function of radius: (Klypin et al. 2002; Rhee et al. 2004; Navarro et al. 1997):

$$\rho_{NFW}(r) = \frac{\rho_s}{x\,(1+x)^2} \tag{C.3}$$

$$C \equiv \frac{r_{vir}}{r_s},\ x \equiv \frac{r}{r_s} \tag{C.4}$$

where ρ_s is the scale density, the density at the scale radius, r_s. C is the concentration parameter which represents the concentration of matter in the halo. It is defined as the ratio of the virial radius to the scale radius. Typically the density

profile is parametrized by x.

Integrating the NFW density profile yields:

$$M_{halo}(< r) \;=\; 4\pi \int_0^r r'^2 \, \rho_{NFW}(r') dr' \tag{C.5}$$

$$M_{halo}(< r) \;=\; 4\pi \, r_s^3 \, \rho_s \, f_{NFW}(x) \tag{C.6}$$

$$f_{NFW}(x) \;\equiv\; \ln(1 + x) - \frac{x}{1 + x} \tag{C.7}$$

Or in terms of the virial mass is:

$$M_{halo}(< r) \;=\; M_{vir} \times \frac{f_{NFW}(x)}{f_{NFW}(C)} \tag{C.8}$$

Substituting this result into Equation C.1 solves for the contribution to the rotation curve from an NFW halo.

$$V_c(r) \;=\; \sqrt{\frac{G \, M_{vir}}{r} \times \frac{f_{NFW}(x)}{f_{NFW}(C)}} \tag{C.9}$$

Additionally, the scale density can be found by setting Equation C.6 to the virial radius.

$$\rho_s \;=\; \frac{M_{vir}}{4\pi \, r_s^3 \, f_{NFW}(C)} \tag{C.10}$$

The NFW model is described in full by knowing a set of M_{vir} and C. The effect of varying M_{vir} and C can be seen in Figure 41. Panel a and b show the effect of varying M_{vir} while keeping C fixed at 15. The rotation curves for these density profiles simple reach a larger rotation velocity in the outer regions with a larger virial mass. Panel c and d show the effect of varying C while keeping M_{vir} fixed at 6×10^{10} M$_\odot$. Panel c shows these density profiles are nearly on top of each other. The differing concentrations change the inner slope of the density profile. This changes the shape

of the rotation curve quite dramatically; which is seen in panel d.

ISO Halo Model

The pseudo isothermal core model differs from the NFW model in that the central regions are of constant density; the density does not increase to a cusp like the NFW density profile. The ISO density profile is:

$$\rho_{ISO}(r) = \frac{\rho_c}{1 + x^2} \tag{C.11}$$

$$C \equiv \frac{r_{vir}}{r_c}, \ x \equiv \frac{r}{r_c} \tag{C.12}$$

Here x and C are defined in the same manner as the NFW profile. ρ_c is the density of the core at radius r_c. When this profile is integrated, the result is:

$$M_{halo}(< r) = 4\pi \, r_c^3 \, \rho_c \, f_{ISO}(x) \tag{C.13}$$

$$f_{ISO}(x) \equiv x - \arctan(x) \tag{C.14}$$

Which, in terms of the virial mass is:

$$M_{halo}(< r) = M_{vir} \times \frac{f_{ISO}(x)}{f_{ISO}(C)} \tag{C.15}$$

And finally, the contribution to the rotation curve is:

$$V_c(r) = \sqrt{\frac{G \, M_{vir}}{r} \times \frac{f_{ISO}(x)}{f_{ISO}(C)}} \tag{C.16}$$

The density at r_c can be solved for by setting Equation C.13 to the virial radius.

$$\rho_c = \frac{M_{vir}}{4\pi \, r_c^3 \, f_{ISO}(C)} \tag{C.17}$$

Just like the NFW model, the ISO model is described in full by knowing a set of

M_{vir} and C. The effect of varying M_{vir} and C can be seen in Figure 42. Panel a and b show the effect of varying M_{vir} while keeping C fixed at 15. Here one can see the density at the center is the same for models of same concentration, and the density profile decreases as the radius gets larger. This decrease is steeper for a lower virial mass halo. The rotation curves for these density profiles follow the same trend as the NFW in that they reach a larger rotation velocity in the outer regions with a larger virial mass, however the rate of increase in rotation velocity is more or less linear in the inner regions. Panel c and d show the effect of varying C while keeping M_{vir} fixed at 6×10^{10} M$_\odot$. Panel c shows these density profiles reach different densities in the core while they appear to converge at large radii. This changes the shape of the rotation curve for these models quite dramatically as well; this is seen in panel d.

Einasto Halo Model

The Einasto model was originally used to describe the distribution of stellar light and mass in galaxies (Einasto 1965; Einasto 1969). Recently it is being used to describe the dark matter distributions (Chemin et al. (2011)). This density profile differs from the previous two profiles because there is a third parameter, the Einasto index, which controls the shape of the density profile. The advantage is that this functional form fits both cupsy (high n) and core-like (low n) density profiles. The Einasto density profile is:

$$\rho_{EIN}(r) \;\; = \;\; \rho_s \exp\left(-2n\left[\left(\frac{r}{r_s}\right)^{1/n} - 1\right]\right) \tag{C.18}$$

$$C \;\; \equiv \;\; \frac{r_{vir}}{r_s}, \; x \equiv \frac{r}{r_s} \tag{C.19}$$

Here x and C are defined in the same manner as the NFW and ISO models. When

integrating this profile, one finds:

$$M_{halo}(< r) \quad = \quad 4\pi \, r_s^3 \, \rho_s \, f_{EIN}(n, x) \tag{C.20}$$

$$f_{EIN}(n, x) \quad \equiv \quad e^{2n} \, n \, (2n)^{-3n} \gamma(3n, \, 2n \cdot (x^{1/n})) \tag{C.21}$$

Where the incomplete gamma function is given by: $\gamma(3n, b) = \int_0^b e^{-y} y^{3n-1} dy$. Which, in terms of the virial mass is:

$$M_{halo}(< r) \quad = \quad M_{vir} \frac{f_{EIN}(n, x)}{f_{EIN}(n, C)} \tag{C.22}$$

$$= \quad M_{vir} \frac{\gamma(3n, \, 2n \cdot (x^{1/n}))}{\gamma(3n, \, 2n \cdot (C^{1/n}))} \tag{C.23}$$

And finally, the contribution to the rotation curve is:

$$V_c(r) \quad = \quad \sqrt{\frac{G \, M_{vir}}{r} \times \frac{\gamma(3n, \, 2n \cdot (x^{1/n}))}{\gamma(3n, \, 2n \cdot (C^{1/n}))}} \tag{C.24}$$

The scale density can be solved for by setting Equation C.20 to the virial radius.

$$\rho_s \quad = \quad \frac{M_{vir}}{4\pi \, r_s^3 \, f_{EIN}(n, C)} \tag{C.25}$$

Unlike the NFW and ISO model, the Einasto profile requires knowledge of n as well as M_{vir} and C in order to describe the model in full. The effect of varying M_{vir}, C, and n can be seen in Figures 43 and 44. Figure 43 panel a show the density profile for different M_{vir} while keeping C fixed at 15 and n fixed at 2. This is reminiscent of the NFW profile, although the NFW profile increases to a cusp with a steeper slope. The rotation curves for these profiles are shown in panel b. Panel c show the density profile for different C while keeping M_{vir} fixed at 6×10^{10} $M_\odot$ and n fixed at 2. As the concentration parameter increases, the inner parts of the density profile increase more rapidly while the outer parts decrease. A low concentration model is

more dense at large radii compared to a high concentration model. The corresponding rotation curves can be seen in panel d. The slope of the rotation curve in the inner part changes dramatically with different concentrations. Figure 44 shows the effect of varying the Einasto index, n while keeping M_{vir} fixed at 6×10^{10} M$_\odot$ and C fixed at 15. Panel a show the density profiles. The density profile looks very cuspy with n=5 and the cusp transitions into a core as this index decreases. The rotation curves corresponding to these density profiles are seen in panel b.

Figure 45 shows all of the profiles, NFW; ISO; and Einasto, on a single plot. They all have M_{vir} fixed at 6×10^{10} M$_\odot$ and C fixed at 15. Three Einasto indicies are plotted, 5; 1; and 0.5. Panel a show the density profiles. Immediately one sees the density profile for the NFW and Einasto n=5 models look strikingly similar, this similarity carries over onto panel b. The ISO profile is below the other profiles, but this is because the density profile decreases must more slowly compared to the Einasto n=1 and n=0.5 density profiles. This also explains the slowly increasing rotation curve in panel b. Panel b shows the rotation curves corresponding to the density profiles in panel a.

APPENDIX D

COPYRIGHT PREMISSIONS

For Figure 1, Credit/Premissions: Galaxies in the Universe by Linda S. Sparke and John S. Gallagher, III, Cambridge University Press, 2007. Reproduced with the written permission of Dr. Sparke for republish in this thesis. Reproduction of Figure 5.20.

For Figure 2, Credit/Premissions: Annual Review of Astronomy and Astrophysics by Annual Reviews. Reproduced with permission of Annual Reviews in the format Republish in a thesis/dissertation via Copyright Clearance Center.

Model IV	
Halo mass, M_{halo} $[M_\odot]$	6.0×10^{10}
Disk mass, M_{disk} $[M_\odot]$	5.7×10^8
Disk scale length, R_d [kpc]	2.14
Disk stability parameter, Q	3.0
Number of halo particles	3.45×10^6
Number of disk particles	1.6×10^5
Halo Concentration, C	12.0
Duration of evolution [Gyr]	1.6
Time step [yr]	1.4×10^4

TABLE 1: The Parameters of N-Body Simulation of Disk Galaxy –
From Model ɪᴠ (Thin Disk) (Rhee et al. 2004).

Annulus [kpc]	Method	x_c,y_c [pxl]	ϕ [°]	i [°]	RMS [km s^{-1}]
3.03	IW	512,511	49	65	2.25
3.03	MET	512,511	48	69	3.95
1.01	IW	512,511	48	60	2.11
1.01	MET	512,511	49	56	4.17
Model	Known	512,511	48	65	-

TABLE 2: N-Body Orientation #1 – Results for 3.01 kpc and 1.01 kpc Annuli
Here the results from sending the N-body in Orientation#1 ($\phi = 48°$, $i = 65°$) through the algorithm. The RMS of the least-squares fit is shown. The known center and orientation parameters are shown in the last line. The mean and scatter of the top twenty results using the IW method on the 3.01 kpc annulus are: $\bar{x}_c, \bar{y}_c = 512, 511 \pm 4$, $\bar{\phi} = 48.8 \pm 1.0$, and $\bar{i} = 64.7 \pm 2.1$. And for the 1.01 kpc annulus: $\bar{x}_c, \bar{y}_c = 512, 511 \pm 4$, $\bar{\phi} = 49.1 \pm 1.2$, and $\bar{i} = 61.3 \pm 2.7$.

Annulus [kpc]	Method	x_c,y_c [pxl]	ϕ [°]	i [°]	RMS [km s^{-1}]
3.03	IW	512,511	302	49	2.28
3.03	MET	512,511	301	52	4.08
1.01	IW	512,511	301	51	2.11
1.01	MET	512,511	301	40	4.57
Model	Known	512,511	300	42	-

TABLE 3: N-Body Orientation #2 – Results for 3.01 kpc and 1.01 kpc Annuli
Here the results from sending the N-body in Orientation#1 ($\phi = 300°$, $i = 42°$) through the algorithm. The RMS of the least-squares fit is shown. The known center and orientation parameters are shown in the last line. The mean and scatter of the top twenty results using the IW method on the 3.01 kpc annulus are: $\bar{x}_c, \bar{y}_c = 512, 511 \pm 4$, $\bar{\phi} = 301.1 \pm 0.9$, and $\bar{i} = 45.2 \pm 2.7$. And for the 1.01 kpc annulus: $\bar{x}_c, \bar{y}_c = 512, 511 \pm 4$, $\bar{\phi} = 301.1 \pm 1.7$, and $\bar{i} = 50.8 \pm 3.0$.

Galaxy	Spacial Res [pc]	Spacial Res ["]	Spacial Res [']	B_{maj} ["]	B_{min} ["]
DDO 154	31.3	1.5	0.025	14.1	12.6
NGC 2366	24.7	1.5	0.025	13.1	11.8
IC 2574	29.1	1.5	0.025	12.8	11.9
NGC 3627	67.6	1.5	0.025	10.0	8.9
DDO 53	26.2	1.5	0.025	11.8	9.5
N-Body #1	29.7	1.5	0.025	13.1	11.8
N-Body #2	29.7	1.5	0.025	13.1	11.8

TABLE 4: Spacial Resolutions for Galaxy Sample –
For completeness, the equivalent resolutions of the simulated galaxy is also shown.
In addition, the major and minor axis of the beam used for each galaxy are shown.

Galaxy	Spectral Res [km s^{-1}]	Spectral Res [kHz]	Spectral Res [μm]	# Channels
DDO 154	2.58	12.2	1.82	57
NGC 2366	2.58	12.2	1.82	66
IC 2574	2.58	12.2	1.82	83
NGC 3627	5.18	24.6	3.65	92
DDO 53	2.58	12.2	1.82	41
N-Body #1	2.58	12.2	1.82	58
N-Body #2	2.58	12.2	1.82	56

TABLE 5: Spectral Resolutions for Galaxy Sample –
For completeness, the equivalent resolutions of the simulated galaxy is also shown.
In addition, the number of velocity channels in each galaxy are shown.

Galaxy	$\mathcal{S}_{HI}$ [Jy km s^{-1}]	M_{HI} [$10^8 M_\odot$]	$V_{20,sys}$ [km s^{-1}]	Dist [Mpc]	σ [mJy]
DDO 154	79.3 ± 4.0	3.46	375.0 ± 2.6	4.3	0.4494
NGC 2366	229 ± 11.4	6.25	100.0 ± 2.6	3.4	0.5267
IC 2574	401 ± 20.1	15.2	48.3 ± 2.6	4.0	0.5235
NGC 3627	39.1 ± 2.0	7.98	719.7 ± 5.2	9.3	0.3868
DDO 53	18.2 ± 0.9	0.56	17.4 ± 2.6	3.6	0.4469

TABLE 6: Information About Galaxy Sample –
The galaxies investigated in this work. S_{HI} is the total flux density, M_{HI} is the Hɪ mass, $V_{20,sys}$ is the velocity from the global Hɪ profile taken at the 20% level, and σ is an estimation of the noise fluctuations. These results are after the cleaning of spurious pixels and are measured using a noise level of 2.5σ. Distances are taken from Walter et al. 2008.

Galaxy	Radii Sampled [kpc]	da [pxl]	# Centers	$\Delta(\text{x,y})_c$ [pxl]	$\Delta(\text{x,y})_c$ [kpc]
DDO 154	3.07, 1.07	$4\frac{1}{3}$	91	8	0.233
NGC 2366	3.02, 1.09	4	92	10	0.247
IC 2574	4.07, 2.07	4	101	9	0.262
NGC 3627	4.17, 2.01	$3\frac{1}{3}$	81	4	0.271
DDO 53	0.94, 0.78, 0.55	$3\frac{2}{3}$	93	6	0.157
N-Body #1	3.03, 1.01	4	49	8	0.237
N-Body #2	3.03, 1.01	4	49	8	0.237

TABLE 7: Annuli and Centers in the Galaxy Sample –
Here the radii of the annuli sampled, the width of those annuli, the number of centers in the search area, and the distance between two centers are shown for each galaxy.

Galaxy	Max i [°]	Min i [°]	Max $|a\text{-}V_{sys}|$ [km s^{-1}]
DDO 154	75	50	4
NGC 2366	75	50	4
IC 2574	65	45	4
NGC 3627	70	40	8
DDO 53	50	15	4
N-Body #1	70	40	4
N-Body #2	55	25	4

TABLE 8: Boundaries of Allowed i and (a-V_{sys}) for the Galaxy Sample.

Galaxy and Annulus	x_c,y_c [pxl]	α_{2000} [h m s]	δ_{2000} [° ' "]	ϕ [°]	i [°]
DDO 154 3.07 kpc^T	504,510	12 54 05.9	+27 09 09.9	230	66
DDO 154 3.07 kpc^O	506,510	12 54 05.7	+27 09 10.0	229	66
NGC 2366 3.02 kpc^T	515,500	07 28 53.9	+69 12 37.4	40	64
NGC 2366 3.02 kpc^O	517,509	07 28 53.4	+69 12 51.0	39	63
IC 2574 4.07 kpc^T	518,525	10 28 27.5	+68 24 58.7	56	53
IC 2574 4.07 kpc^O	517,526	10 28 27.7	+68 24 59.0	53	55
NGC 3627 4.17 kpc^{T,R}	512,513	11 20 15.0	+12 59 29.6	173	62
DDO 53 0.94 kpc^O	522,484	08 34 06.5	+66 10 48.0	131	27

TABLE 9: Model Parameters from Trachternach et al. 2008 and Oh et al. 2011 – Rows labeled with ^{O} come from Oh et al. 2011, which investigated THINGS Dwarfs. Rows labeled with ^{T} come from Trachternach et al. 2008 and the center used comes from the ROTCUR routine while ^{T,R} means it comes from the location of a radio nuclear source. This is associated with a central compact object which should be at (or close to) the bottom of the potental well.

Galaxy and Annulus	x_c,y_c [pxl]	α_{2000} [h m s]	δ_{2000} [° ' '']	ϕ [°]	i [°]	V_c [km s^{-1}]	RMS [km s^{-1}]
DDO 154 3.07 kpc	516,505	12 54 04.6	+27 09 02.0	224	64	38.033	1.366
1.07 kpc	476,489	12 54 09.0	+27 08 38.0	226	75	14.420	0.928
NGC 2366 3.02 kpc	535,504	07 28 48.4	+69 12 43.1	55	70	50.932	2.797
1.09 kpc	555,524	07 28 48.4	+69 13 13.1	50	74	13.955	1.358
IC 2574 4.07 kpc	543,561	10 28 20.7	+68 25 52.4	46	64	25.449	4.440
2.07 kpc	507,489	10 28 30.4	+68 24 04.1	54	63	18.260	2.360
NGC 3627 4.17 kpc	510,508	11 20 15.2	+12 59 22.0	169	59	194.976	9.329
2.01 kpc	494,512	11 20 16.9	+12 59 28.0	169	69	127.673	9.097
DDO 53 0.94 kpc	516,470	08 34 07.8	+66 10 27.5	124	47	14.263	1.870
0.78 kpc	516,476	08 34 07.8	+66 10 36.5	129	48	12.690	1.667
0.55 kpc	534,470	08 34 03.3	+66 10 27.5	127	50	6.808	1.233

TABLE 10: The Top Results –
Here the set of parameters the algorithm found corresponding to the lowest RMS from each galaxy and annulus in this work are shown. See the Tables 13 through 23 for lists of the top twenty results, and for the mean and scatter of those results.

Galaxy and Annulus	x_c,y_c [pxl]	ϕ [°]	i [°]	V_c	RMS
DDO 154 3.07 kpc^T	504,510	230	66	38.336	2.081
1.07 kpc^T				20.070	1.699
DDO 154 3.07 kpc^O	506,510	229	66	38.356	1.880
1.07 kpc^O				20.553	1.700
NGC 2366 3.02 kpc^T	515,500	40	64	47.194	4.413
1.09 kpc^T				21.301	2.825
NGC 2366 3.02 kpc^O	517,509	39	63	47.907	5.038
1.09 kpc^O				21.061	3.291
IC 2574 4.07 kpc^T	518,525	56	53	34.229	8.909
2.07 kpc^T				24.408	6.437
IC 2574 4.07 kpc^O	517,526	53	55	36.088	8.948
2.07 kpc^O				21.224	4.599
NGC 3627 4.17 kpc^T	512,513	173	62	178.857	21.688
2.01 kpc^T				118.004	15.583
DDO 53 0.94 kpc^O	522,484	131	27	17.711	3.190
0.78 kpc^O				16.860	2.558
0.55 kpc^O				13.094	2.208

TABLE 11: Results Using Sets Parameters from Trachternach et al. 2008 and Oh et al. 2011 –
Rows labeled with ^{O} come from Oh et al. 2011. Rows labeled with ^{T} come from Trachternach et al. 2008. These set of parameters were run through the algorithm using the IW method for the annuli listed and yielded V_c and the associated RMS.

Galaxy and Annulus	$\Delta(x_c, y_c)$ [kpc]	$\Delta\phi$ [°]	Δi [°]	ΔV_c [km s^{-1}]	ΔRMS [km s^{-1}]
DDO 154 3.07 kpc^T	0.407	-6	-2	-0.303	-0.714
1.07 kpc^T	1.096	-4	+9	-5.65	-0.771
DDO 154 3.07 kpc^O	0.350	-5	-2	-0.323	-0.514
1.07 kpc^O	1.146	-3	+9	-6.133	-0.772
NGC 2366 3.02 kpc^T	0.504	+15	+6	+3.738	-1.613
1.09 kpc^T	1.152	+10	+10	-7.346	-0.152
NGC 2366 3.02 kpc^O	0.461	+16	+7	+3.025	-2.241
1.09 kpc^O	1.009	+11	+11	-7.106	-1.933
IC 2574 4.07 kpc^T	1.275	-10	+11	-8.780	-4.47
2.07 kpc^T	1.095	-1	+10	-6.148	-4.08
IC 2574 4.07 kpc^O	1.269	-7	+9	-10.639	-4.508
2.07 kpc^O	1.115	+1	+8	-2.964	-2.239
NGC 3627 4.17 kpc^T	0.364	-4	-3	+16.119	-6.251
2.01 kpc^T	1.219	-4	+7	+9.669	-12.593
DDO 53 0.94 kpc^O	0.399	-7	+20	-3.448	-1.32
0.78 kpc^O	0.262	-2	+21	-4.170	-0.893
0.55 kpc^O	0.483	-4	+23	-6.286	-0.977

TABLE 12: Comparison with Other Work –
Here the differences between the model parameters found in this work with work from Trachternach et al. (2008) (rows marked with ^{T}) and Oh et al. (2011) (rows marked with ^{O}). Equation to compare parameters: $ThisWork - TheirWork$.

	x_c,y_c	α_{2000}	δ_{2000}	ϕ	i	V_c	RMS	$(a - V_{sys})$	
	[pxl]	[h m s]	[° ' "]	[°]	[°]	[km s^{-1}]	[km s^{-1}]	[km s^{-1}]	n_{anu}
1	516,505	12 54 04.6	+27 09 02.0	224	64	38.033	1.366	3.72	1178
2	516,505	12 54 04.6	+27 09 02.0	224	65	37.961	1.381	3.84	1108
3	508,513	12 54 05.5	+27 09 14.0	225	69	38.326	1.405	1.30	944
4	516,505	12 54 04.6	+27 09 02.0	225	66	37.873	1.410	3.97	1068
5	516,505	12 54 04.6	+27 09 02.0	225	65	37.922	1.411	3.83	1108
6	516,505	12 54 04.6	+27 09 02.0	224	66	37.889	1.413	3.97	1068
7	516,505	12 54 04.6	+27 09 02.0	225	64	38.044	1.413	3.71	1166
8	508,513	12 54 05.5	+27 09 14.0	225	68	38.450	1.417	1.20	992
9	516,505	12 54 04.6	+27 09 02.0	223	64	38.081	1.427	3.78	1178
10	516,505	12 54 04.6	+27 09 02.0	224	63	38.228	1.438	3.59	1204
11	508,513	12 54 05.5	+27 09 14.0	224	69	38.254	1.443	1.33	956
12	516,505	12 54 04.6	+27 09 02.0	223	65	38.012	1.445	3.90	1122
13	516,505	12 54 04.6	+27 09 02.0	223	63	38.270	1.450	3.63	1212
14	508,513	12 54 05.5	+27 09 14.0	226	68	38.439	1.466	1.17	994
15	508,513	12 54 05.5	+27 09 14.0	226	69	38.344	1.467	1.29	956
16	508,513	12 54 05.5	+27 09 14.0	225	65	38.741	1.480	1.10	1108
17	508,513	12 54 05.5	+27 09 14.0	224	68	38.365	1.486	1.27	994
18	508,513	12 54 05.5	+27 09 14.0	225	70	38.253	1.489	1.38	892
19	516,505	12 54 04.6	+27 09 02.0	223	66	37.900	1.493	3.99	1074
20	516,505	12 54 04.6	+27 09 02.0	225	63	38.183	1.501	3.57	1194

TABLE 13: DDO 154 – Results for 3.07 kpc Annulus

These are the 20 best set of parameters based on lowest RMS. The intensity weighted method was used to extract velocities from line-of-sight spectra. The mean and scatter of these top twenty results are: $\bar{x}_c, \bar{y}_c = 512.8, 508.2 \pm 4.0$, $\bar{\phi} = 224.4 \pm 0.9$, $\bar{i} = 66 \pm 2.3$, $\bar{V}_c = 38.18 \pm 1.25$, and $\bar{RMS} = 1.44 \pm 0.04$.

	x_c, y_c [pxl]	α_{2000} [h m s]	δ_{2000} [° ' '']	ϕ [°]	i [°]	V_c [km s^{-1}]	RMS [km s^{-1}]	$(a - V_{sys})$ [km s^{-1}]	n_{anu}
1	476,489	12 54 09.0	+27 08 38.0	226	75	14.420	0.928	-0.91	244
2	476,489	12 54 09.0	+27 08 38.0	225	75	14.423	0.931	-0.95	244
3	476,489	12 54 09.0	+27 08 38.0	224	75	14.480	0.933	-0.97	244
4	476,489	12 54 09.0	+27 08 38.0	225	74	14.399	0.944	-1.01	248
5	476,489	12 54 09.0	+27 08 38.0	223	75	14.435	0.946	-1.00	246
6	476,489	12 54 09.0	+27 08 38.0	223	73	14.505	0.947	-1.09	272
7	476,489	12 54 09.0	+27 08 38.0	223	74	14.453	0.949	-1.07	260
8	476,489	12 54 09.0	+27 08 38.0	224	74	14.451	0.955	-1.03	258
9	476,489	12 54 09.0	+27 08 38.0	225	73	14.417	0.958	-1.05	260
10	476,489	12 54 09.0	+27 08 38.0	224	73	14.419	0.965	-1.09	272
11	476,489	12 54 09.0	+27 08 38.0	226	74	14.421	0.968	-0.98	258
12	476,489	12 54 09.0	+27 08 38.0	224	72	14.432	0.973	-1.11	294
13	476,489	12 54 09.0	+27 08 38.0	222	74	14.457	0.980	-1.08	268
14	476,489	12 54 09.0	+27 08 38.0	222	75	14.440	0.983	-1.03	252
15	476,489	12 54 09.0	+27 08 38.0	225	72	14.459	0.984	-1.05	288
16	476,489	12 54 09.0	+27 08 38.0	227	75	14.354	0.984	-0.88	246
17	476,489	12 54 09.0	+27 08 38.0	223	72	14.491	0.993	-1.14	286
18	476,489	12 54 09.0	+27 08 38.0	222	73	14.480	1.001	-1.11	272
19	476,489	12 54 09.0	+27 08 38.0	226	73	14.414	1.001	-1.01	272
20	476,489	12 54 09.0	+27 08 38.0	224	71	14.460	1.001	-1.16	300

TABLE 14: DDO 154 – Results for 1.07 kpc Annulus

These are the 20 best set of parameters based on lowest RMS. The intensity weighted method was used to extract velocities from line-of-sight spectra. The mean and scatter of these top twenty results are: $\bar{x}_c, \bar{y}_c = 476, 489 \pm 4.0$, $\bar{\phi} = 224.2 \pm 1.5$, $\bar{i} = 73.6 \pm 1.2$, $\bar{V}_c = 14.44 \pm 1.25$, and $\bar{RMS} = 0.97 \pm 0.02$.

	x_c, y_c	α_{2000}	δ_{2000}	ϕ	i	V_c	RMS	$(a - V_{sys})$	
	[pxl]	[h m s]	[° ' "]	[°]	[°]	[km s^{-1}]	[km s^{-1}]	[km s^{-1}]	n_{anu}
1	535,504	07 28 48.4	+69 12 43.1	55	70	2.797	50.932	-1.30	1057
2	535,504	07 28 48.4	+69 12 43.1	55	71	2.820	50.637	-1.28	996
3	535,504	07 28 48.4	+69 12 43.1	54	70	2.837	50.996	-1.28	1058
4	535,504	07 28 48.4	+69 12 43.1	54	69	2.922	51.192	-1.23	1094
5	535,504	07 28 48.4	+69 12 43.1	54	71	2.925	50.829	-1.39	988
6	535,504	07 28 48.4	+69 12 43.1	56	70	2.926	50.735	-1.40	1030
7	535,504	07 28 48.4	+69 12 43.1	55	69	2.941	51.352	-1.36	1075
8	535,504	07 28 48.4	+69 12 43.1	56	72	2.957	50.295	-1.42	959
9	535,504	07 28 48.4	+69 12 43.1	56	71	2.982	50.601	-1.42	996
10	545,514	07 28 45.6	+69 12 58.1	49	75	3.009	50.136	-2.43	767
11	535,504	07 28 48.4	+69 12 43.1	53	70	3.016	51.085	-1.33	1042
12	545,514	07 28 45.6	+69 12 58.1	48	75	3.032	50.163	-2.36	802
13	535,504	07 28 48.4	+69 12 43.1	57	71	3.045	50.450	-1.51	983
14	535,504	07 28 48.4	+69 12 43.1	53	69	3.049	51.293	-1.19	1098
15	535,504	07 28 48.4	+69 12 43.1	55	72	3.050	50.527	-1.22	938
16	535,504	07 28 48.4	+69 12 43.1	53	71	3.062	50.813	-1.29	994
17	545,514	07 28 45.6	+69 12 58.1	50	75	3.075	50.042	-2.41	774
18	545,514	07 28 45.6	+69 12 58.1	47	75	3.102	50.344	-2.33	788
19	535,504	07 28 48.4	+69 12 43.1	52	70	3.122	50.886	-1.20	1046
20	535,504	07 28 48.4	+69 12 43.1	57	70	3.124	50.880	-1.51	1041

TABLE 15: NGC 2366 – Results for 3.02 kpc Annulus
These are the 20 best set of parameters based on lowest RMS. The intensity weighted method was used to extract velocities from line-of-sight spectra. The mean and scatter of these top twenty results are: $\bar{x}_c, \bar{y}_c = 537, 506 \pm 4.1$, $\bar{\phi} = 53.45 \pm 2.9$, $\bar{i} = 71.3 \pm 2.1$, $\bar{V}_c = 50.71 \pm 1.25$, and $\bar{RMS} = 2.99 \pm 0.10$.

	x_c, y_c	α_{2000}	δ_{2000}	ϕ	i	V_c	RMS	$(a - V_{sys})$	
	[pxl]	[h m s]	[° ' "]	[°]	[°]	[km s^{-1}]	[km s^{-1}]	[km s^{-1}]	n_{anu}
1	555,524	07 28 48.4	+69 13 13.1	50	74	13.955	1.358	-1.26	300
2	555,524	07 28 48.4	+69 13 13.1	49	74	13.801	1.375	-1.16	310
3	555,524	07 28 48.4	+69 13 13.1	48	74	13.636	1.387	-1.16	306
4	555,524	07 28 48.4	+69 13 13.1	50	75	13.733	1.392	-1.24	276
5	555,524	07 28 48.4	+69 13 13.1	48	75	13.534	1.406	-1.16	286
6	555,524	07 28 48.4	+69 13 13.1	51	74	13.965	1.412	-1.22	304
7	555,524	07 28 48.4	+69 13 13.1	50	73	14.043	1.414	-1.25	324
8	555,524	07 28 48.4	+69 13 13.1	51	73	14.054	1.420	-1.30	320
9	555,524	07 28 48.4	+69 13 13.1	49	73	13.882	1.420	-1.19	324
10	555,524	07 28 48.4	+69 13 13.1	49	75	13.678	1.423	-1.11	296
11	555,524	07 28 48.4	+69 13 13.1	47	75	13.469	1.436	-1.09	274
12	555,524	07 28 48.4	+69 13 13.1	52	75	13.915	1.441	-1.36	294
13	555,524	07 28 48.4	+69 13 13.1	51	75	13.847	1.442	-1.25	288
14	555,524	07 28 48.4	+69 13 13.1	52	74	14.078	1.444	-1.32	314
15	555,524	07 28 48.4	+69 13 13.1	51	72	14.191	1.447	-1.35	338
16	555,524	07 28 48.4	+69 13 13.1	49	72	14.007	1.447	-1.25	338
17	555,524	07 28 48.4	+69 13 13.1	50	72	14.136	1.457	-1.26	352
18	555,524	07 28 48.4	+69 13 13.1	47	74	13.590	1.458	-1.12	298
19	555,524	07 28 48.4	+69 13 13.1	52	73	14.167	1.462	-1.34	326
20	555,524	07 28 48.4	+69 13 13.1	50	71	14.222	1.469	-1.37	366

TABLE 16: NGC 2366 – Results for 1.09 kpc Annulus

These are the 20 best set of parameters based on lowest RMS. The intensity weighted method was used to extract velocities from line-of-sight spectra. The mean and scatter of these top twenty results are: $\bar{x}_c, \bar{y}_c = 555, 524 \pm 5$, $\bar{\phi} = 49.8 \pm 1.5$, $\bar{i} = 73.7 \pm 1.2$, $\bar{V}_c = 13.90 \pm 1.25$, and $\bar{\mathrm{RMS}} = 1.43 \pm 0.04$.

	x_c, y_c	α_{2000}	δ_{2000}	ϕ	i	V_c	RMS	$(a - V_{sys})$	
	[pxl]	[h m s]	[° ' "]	[°]	[°]	[km s^{-1}]	[km s^{-1}]	[km s^{-1}]	n_{anu}
1	543,561	10 28 20.7	+68 25 52.4	46	64	25.449	4.440	0.28	1529
2	543,561	10 28 20.7	+68 25 52.4	45	64	25.198	4.492	0.27	1518
3	543,561	10 28 20.7	+68 25 52.4	47	64	25.765	4.554	0.32	1553
4	543,561	10 28 20.7	+68 25 52.4	47	65	25.175	4.560	-0.038	1476
5	543,561	10 28 20.7	+68 25 52.4	45	63	25.558	4.593	0.43	1600
6	543,561	10 28 20.7	+68 25 52.4	46	63	25.847	4.600	0.49	1596
7	543,561	10 28 20.7	+68 25 52.4	44	62	25.883	4.618	0.61	1665
8	543,561	10 28 20.7	+68 25 52.4	44	63	25.315	4.620	0.41	1595
9	543,561	10 28 20.7	+68 25 52.4	43	62	25.641	4.623	0.57	1650
10	543,561	10 28 20.7	+68 25 52.4	44	64	25.185	4.634	0.40	1537
11	543,561	10 28 20.7	+68 25 52.4	43	63	25.192	4.659	0.39	1604
12	543,561	10 28 20.7	+68 25 52.4	48	65	25.308	4.660	-0.028	1490
13	543,561	10 28 20.7	+68 25 52.4	41	61	25.646	4.673	0.66	1703
14	543,561	10 28 20.7	+68 25 52.4	46	65	25.114	4.677	0.093	1464
15	543,561	10 28 20.7	+68 25 52.4	42	61	25.883	4.678	0.75	1706
16	543,561	10 28 20.7	+68 25 52.4	42	62	25.397	4.701	0.52	1651
17	543,561	10 28 20.7	+68 25 52.4	45	62	25.959	4.742	0.63	1653
18	543,561	10 28 20.7	+68 25 52.4	43	61	26.056	4.745	0.77	1708
19	543,561	10 28 20.7	+68 25 52.4	47	63	26.133	4.750	0.51	1606
20	543,561	10 28 20.7	+68 25 52.4	48	64	25.856	4.758	0.25	1540

TABLE 17: IC 2574 – Results for 4.07 kpc Annulus

These are the 20 best set of parameters based on lowest RMS. The intensity weighted method was used to extract velocities from line-of-sight spectra. The mean and scatter of these top twenty results are: $\bar{x}_c, \bar{y}_c = 543, 561 \pm 4.5$, $\bar{\phi} = 44.8 \pm 2.1$, $\bar{i} = 63.1 \pm 1.32$, $\bar{V}_c = 25.58 \pm 1.25$, and $\bar{RMS} = 4.64 \pm 0.08$.

	x_c, y_c	α_{2000}	δ_{2000}	ϕ	i	V_c	RMS	$(a - V_{sys})$	
	[pxl]	[h m s]	[° ' "]	[°]	[°]	[km s^{-1}]	[km s^{-1}]	[km s^{-1}]	n_{anu}
1	507,489	10 28 30.4	+68 24 04.1	54	63	18.260	2.360	-1.14	802
2	507,489	10 28 30.4	+68 24 04.1	55	63	18.291	2.361	-1.27	810
3	516,480	10 28 27.9	+68 23 50.7	59	65	16.441	2.364	-3.98	732
4	507,489	10 28 30.4	+68 24 04.1	56	64	17.958	2.364	-1.33	792
5	507,489	10 28 30.4	+68 24 04.1	55	64	17.928	2.371	-1.27	780
6	507,489	10 28 30.4	+68 24 04.1	57	65	17.479	2.375	-1.37	758
7	516,480	10 28 27.9	+68 23 50.7	58	65	16.470	2.379	-3.94	750
8	507,489	10 28 30.4	+68 24 04.1	53	63	18.340	2.383	-1.06	814
9	507,489	10 28 30.4	+68 24 04.1	54	64	18.021	2.393	-1.18	778
10	507,489	10 28 30.4	+68 24 04.1	58	65	17.351	2.394	-1.46	750
11	507,489	10 28 30.4	+68 24 04.1	56	63	18.200	2.398	-1.33	806
12	507,489	10 28 30.4	+68 24 04.1	57	64	17.889	2.400	-1.45	770
13	507,489	10 28 30.4	+68 24 04.1	56	65	17.619	2.401	-1.35	750
14	507,489	10 28 30.4	+68 24 04.1	58	64	17.685	2.403	-1.44	780
15	507,489	10 28 30.4	+68 24 04.1	59	65	17.237	2.406	-1.48	732
16	507,489	10 28 30.4	+68 24 04.1	53	62	18.610	2.410	-1.06	832
17	507,489	10 28 30.4	+68 24 04.1	53	65	17.781	2.414	-1.16	770
18	507,489	10 28 30.4	+68 24 04.1	55	65	17.707	2.416	-1.27	760
19	516,480	10 28 27.9	+68 23 50.7	58	64	16.621	2.419	-3.99	780
20	507,489	10 28 30.4	+68 24 04.1	60	65	17.081	2.420	-1.54	754

TABLE 18: IC 2574 – Results for 2.07 kpc Annulus
These are the 20 best set of parameters based on lowest RMS. The intensity weighted method was used to extract velocities from line-of-sight spectra. The mean and scatter of these top twenty results are: $\bar{x}_c, \bar{y}_c = 508.4, 487.7 \pm 4.5$, $\bar{\phi} = 56.2 \pm 2.2$, $\bar{i} = 64.2 \pm 0.9$, $\bar{V}_c = 17.65 \pm 0.62$, and $\bar{RMS} = 2.39 \pm 0.02$.

	x_c,y_c	α_{2000}	δ_{2000}	ϕ	i	V_c	RMS	$(a - V_{sys})$	
	[pxl]	[h m s]	[° ' "]	[°]	[°]	[km s^{-1}]	[km s^{-1}]	[km s^{-1}]	n_{anu}
1	510,508	11 20 15.2	+12 59 22.0	169	59	194.976	9.329	-4.78	619
2	506,512	11 20 15.6	+12 59 28.0	170	61	192.108	9.331	-7.28	545
3	506,512	11 20 15.6	+12 59 28.0	170	62	191.958	9.364	-6.66	528
4	506,512	11 20 15.6	+12 59 28.0	171	62	191.571	9.436	-6.90	497
5	510,508	11 20 15.2	+12 59 22.0	170	59	195.459	9.442	-5.03	613
6	510,508	11 20 15.2	+12 59 22.0	168	60	194.841	9.446	-4.43	616
7	510,508	11 20 15.2	+12 59 22.0	169	61	194.481	9.449	-4.10	588
8	510,508	11 20 15.2	+12 59 22.0	169	60	194.337	9.468	-4.64	622
9	506,512	11 20 15.6	+12 59 28.0	169	61	191.739	9.472	-7.75	553
10	510,508	11 20 15.2	+12 59 22.0	169	58	195.552	9.477	-5.15	640
11	510,508	11 20 15.2	+12 59 22.0	169	57	196.020	9.508	-5.54	672
12	510,508	11 20 15.2	+12 59 22.0	170	58	195.606	9.517	-5.03	657
13	510,508	11 20 15.2	+12 59 22.0	168	59	194.242	9.605	-4.89	648
14	506,512	11 20 15.6	+12 59 28.0	171	61	191.349	9.670	-7.66	535
15	510,508	11 20 15.2	+12 59 22.0	170	60	194.687	9.703	-4.61	613
16	510,508	11 20 15.2	+12 59 22.0	170	57	196.521	9.721	-5.25	679
17	506,512	11 20 15.6	+12 59 28.0	169	62	191.711	9.727	-7.24	538
18	510,508	11 20 15.2	+12 59 22.0	168	61	194.595	9.738	-4.26	587
19	510,508	11 20 15.2	+12 59 22.0	170	61	193.925	9.837	-4.51	583
20	510,508	11 20 15.2	+12 59 22.0	168	58	193.925	9.850	-4.97	651

TABLE 19: NGC 3627 – Results for 4.17 kpc Annulus
These are the 20 best set of parameters based on lowest RMS. The intensity weighted method was used to extract velocities from line-of-sight spectra. The mean and scatter of these top twenty results are: $\bar{x}_c, \bar{y}_c = 508.8, 508.2 \pm 2$, $\bar{\phi} = 169.4 \pm 0.9$, $\bar{i} = 59.9 \pm 1.6$, $\bar{V}_c = 193.98 \pm 2.59$, and $\bar{\text{RMS}} = 9.55 \pm 0.16$.

	x_c, y_c	α_{2000}	δ_{2000}	ϕ	i	V_c	RMS	$(a - V_{sys})$	
	[pxl]	[h m s]	[° ' "]	[°]	[°]	[km s^{-1}]	[km s^{-1}]	[km s^{-1}]	n_{anu}
1	494,512	11 20 16.9	+12 59 28.0	169	69	127.673	9.097	2.64	172
2	494,512	11 20 16.9	+12 59 28.0	168	69	127.457	9.152	2.52	166
3	494,512	11 20 16.9	+12 59 28.0	170	70	126.786	9.393	3.52	163
4	494,512	11 20 16.9	+12 59 28.0	170	68	129.661	9.454	4.33	180
5	494,512	11 20 16.9	+12 59 28.0	169	68	129.206	9.479	3.63	175
6	494,512	11 20 16.9	+12 59 28.0	171	70	127.115	9.513	3.95	168
7	494,512	11 20 16.9	+12 59 28.0	166	70	127.019	9.520	1.94	162
8	494,512	11 20 16.9	+12 59 28.0	171	68	129.456	9.557	4.29	183
9	494,516	11 20 16.9	+12 59 34.0	172	69	122.278	9.581	-6.86	196
10	494,512	11 20 16.9	+12 59 28.0	167	70	126.504	9.582	2.21	163
11	494,512	11 20 16.9	+12 59 28.0	168	70	126.617	9.711	2.38	177
12	494,512	11 20 16.9	+12 59 28.0	167	69	127.241	9.798	1.77	162
13	494,516	11 20 16.9	+12 59 34.0	171	70	122.156	9.803	-7.37	190
14	494,516	11 20 16.9	+12 59 34.0	172	70	121.612	9.838	-7.40	198
15	494,512	11 20 16.9	+12 59 28.0	168	68	128.550	9.923	1.87	188
16	494,516	11 20 16.9	+12 59 34.0	170	70	121.383	9.924	-7.87	186
17	494,512	11 20 16.9	+12 59 28.0	168	67	130.006	9.925	2.59	189
18	494,516	11 20 16.9	+12 59 34.0	173	69	121.749	9.948	-6.92	200
19	494,516	11 20 16.9	+12 59 34.0	171	68	123.149	9.984	-7.75	201
20	494,512	11 20 16.9	+12 59 28.0	166	69	128.507	10.031	0.94	179

TABLE 20: NGC 3627 – Results for 2.01 kpc Annulus
These are the 20 best set of parameters based on lowest RMS. The intensity weighted method was used to extract velocities from line-of-sight spectra. The mean and scatter of these top twenty results are: $\bar{x}_c, \bar{y}_c = 494, 513.2 \pm 2$, $\bar{\phi} = 169.4 \pm 2.0$, $\bar{i} = 69.1 \pm 0.94$, $\bar{V}_c = 126.21 \pm 2.59$, and $\bar{RMS} = 9.66 \pm 0.27$.

	x_c, y_c	α_{2000}	δ_{2000}	ϕ	i	V_c	RMS	$(a - V_{sys})$	
	[pxl]	[h m s]	[° ' '']	[°]	[°]	[km s^{-1}]	[km s^{-1}]	[km s^{-1}]	n_{anu}
1	516,470	08 34 07.8	+66 10 27.5	124	47	14.263	1.870	3.95	556
2	516,470	08 34 07.8	+66 10 27.5	126	45	14.712	1.879	3.84	588
3	516,470	08 34 07.8	+66 10 27.5	126	46	14.489	1.880	3.87	578
4	516,470	08 34 07.8	+66 10 27.5	124	46	14.477	1.882	3.90	568
5	516,470	08 34 07.8	+66 10 27.5	125	46	14.527	1.885	3.88	582
6	516,470	08 34 07.8	+66 10 27.5	125	45	14.640	1.889	3.80	584
7	516,470	08 34 07.8	+66 10 27.5	126	44	14.924	1.890	3.80	598
8	516,470	08 34 07.8	+66 10 27.5	127	45	14.727	1.891	3.81	588
9	516,470	08 34 07.8	+66 10 27.5	123	46	14.451	1.891	3.89	562
10	516,470	08 34 07.8	+66 10 27.5	125	44	14.851	1.892	3.77	590
11	516,470	08 34 07.8	+66 10 27.5	124	44	14.857	1.895	3.76	576
12	516,470	08 34 07.8	+66 10 27.5	123	47	14.295	1.898	3.91	562
13	516,470	08 34 07.8	+66 10 27.5	125	47	14.391	1.902	3.94	560
14	516,470	08 34 07.8	+66 10 27.5	124	45	14.674	1.903	3.80	582
15	516,470	08 34 07.8	+66 10 27.5	127	46	14.528	1.905	3.84	568
16	516,470	08 34 07.8	+66 10 27.5	127	47	14.348	1.911	3.87	556
17	516,470	08 34 07.8	+66 10 27.5	125	48	14.206	1.912	3.93	554
18	516,470	08 34 07.8	+66 10 27.5	126	47	14.340	1.914	3.89	560
19	516,470	08 34 07.8	+66 10 27.5	124	48	14.213	1.915	3.97	566
20	516,470	08 34 07.8	+66 10 27.5	128	48	14.161	1.919	3.90	548

TABLE 21: DDO 53 – Results for 0.94 kpc Annulus
These are the 20 best set of parameters based on lowest RMS. The intensity weighted method was used to extract velocities from line-of-sight spectra. The mean and scatter of these top twenty results are: $\bar{x}_c, \bar{y}_c = 516, 470 \pm 3$, $\bar{\phi} = 125.2 \pm 1.4$, $\bar{i} = 46.1 \pm 1.3$, $\bar{V}_c = 14.50 \pm 0.23$, and $\bar{RMS} = 1.90 \pm 0.01$.

	x_c,y_c	α_{2000}	δ_{2000}	ϕ	i	V_c	RMS	$(a - V_{sys})$	
	[pxl]	[h m s]	[° ' "]	[°]	[°]	[km s^{-1}]	[km s^{-1}]	[km s^{-1}]	n_{anu}
1	516,476	08 34 07.8	+66 10 36.5	129	48	12.690	1.667	3.15	454
2	516,476	08 34 07.8	+66 10 36.5	131	48	12.704	1.678	3.16	452
3	516,476	08 34 07.8	+66 10 36.5	130	48	12.707	1.680	3.16	458
4	516,476	08 34 07.8	+66 10 36.5	130	47	12.915	1.684	3.13	468
5	516,476	08 34 07.8	+66 10 36.5	128	48	12.708	1.686	3.19	468
6	516,476	08 34 07.8	+66 10 36.5	130	49	12.501	1.686	3.20	448
7	516,476	08 34 07.8	+66 10 36.5	131	47	12.882	1.687	3.13	456
8	516,476	08 34 07.8	+66 10 36.5	128	47	12.887	1.688	3.21	474
9	516,476	08 34 07.8	+66 10 36.5	128	50	12.309	1.689	3.22	432
10	516,476	08 34 07.8	+66 10 36.5	130	46	13.106	1.691	3.10	484
11	516,476	08 34 07.8	+66 10 36.5	129	49	12.530	1.691	3.21	446
12	516,476	08 34 07.8	+66 10 36.5	129	47	12.895	1.692	3.17	466
13	516,476	08 34 07.8	+66 10 36.5	127	46	13.080	1.692	3.17	478
14	516,476	08 34 07.8	+66 10 36.5	128	49	12.517	1.695	3.21	446
15	516,476	08 34 07.8	+66 10 36.5	130	45	13.279	1.696	3.09	486
16	516,476	08 34 07.8	+66 10 36.5	129	46	13.122	1.697	3.15	484
17	516,476	08 34 07.8	+66 10 36.5	125	48	12.649	1.697	3.22	458
18	516,476	08 34 07.8	+66 10 36.5	128	46	13.070	1.699	3.15	480
19	516,476	08 34 07.8	+66 10 36.5	132	48	12.731	1.700	3.16	460
20	516,476	08 34 07.8	+66 10 36.5	129	50	12.350	1.700	3.25	432

TABLE 22: DDO 53 – Results for 0.78 kpc Annulus
These are the 20 best set of parameters based on lowest RMS. The intensity weighted method was used to extract velocities from line-of-sight spectra. The mean and scatter of these top twenty results are: $\bar{x}_c, \bar{y}_c = 516, 476 \pm 3$, $\bar{\phi} = 129.1 \pm 1.6$, $\bar{i} = 47.6 \pm 1.4$, $\bar{V}_c = 12.78 \pm 1.25$, and $\bar{RMS} = 1.69 \pm 0.01$.

	x_c,y_c	α_{2000}	δ_{2000}	ϕ	i	V_c	RMS	$(a - V_{sys})$	
	[pxl]	[h m s]	[° ' "]	[°]	[°]	[km s^{-1}]	[km s^{-1}]	[km s^{-1}]	n_{anu}
1	534,470	08 34 03.3	+66 10 27.5	127	50	6.808	1.233	-0.54	306
2	534,470	08 34 03.3	+66 10 27.5	129	50	6.832	1.235	-0.57	298
3	534,470	08 34 03.3	+66 10 27.5	130	50	6.805	1.237	-0.58	300
4	534,470	08 34 03.3	+66 10 27.5	131	50	6.789	1.241	-0.60	304
5	534,470	08 34 03.3	+66 10 27.5	128	50	6.834	1.242	-0.53	302
6	534,470	08 34 03.3	+66 10 27.5	126	50	6.833	1.243	-0.55	310
7	534,470	08 34 03.3	+66 10 27.5	127	49	6.826	1.255	-0.53	322
8	534,470	08 34 03.3	+66 10 27.5	129	49	6.849	1.258	-0.55	314
9	534,470	08 34 03.3	+66 10 27.5	130	49	6.854	1.259	-0.55	316
10	534,470	08 34 03.3	+66 10 27.5	132	50	6.757	1.266	-0.61	308
11	534,470	08 34 03.3	+66 10 27.5	128	49	6.888	1.268	-0.57	320
12	534,470	08 34 03.3	+66 10 27.5	135	50	6.719	1.268	-0.58	314
13	534,470	08 34 03.3	+66 10 27.5	126	49	6.851	1.271	-0.51	318
14	534,470	08 34 03.3	+66 10 27.5	127	48	6.868	1.271	-0.53	324
15	534,470	08 34 03.3	+66 10 27.5	125	49	6.849	1.273	-0.50	318
16	534,470	08 34 03.3	+66 10 27.5	125	50	6.771	1.275	-0.53	312
17	534,470	08 34 03.3	+66 10 27.5	131	49	6.819	1.275	-0.56	320
18	534,470	08 34 03.3	+66 10 27.5	128	48	6.866	1.279	-0.54	324
19	534,470	08 34 03.3	+66 10 27.5	126	48	6.914	1.283	-0.51	322
20	528,470	08 34 03.3	+66 10 27.5	115	38	9.258	1.283	1.46	374

TABLE 23: DDO 53 – Results for 0.55 kpc Annulus

These are the 20 best set of parameters based on lowest RMS. The intensity weighted method was used to extract velocities from line-of-sight spectra. The mean and scatter of these top twenty results are: $\bar{x}_c, \bar{y}_c = 533.7, 470 \pm 3$, $\bar{\phi} = 127.8 \pm 3.9$, $\bar{i} = 48.8 \pm 2.6$, $\bar{V}_c = 6.95 \pm 0.55$, and $\bar{RMS} = 1.26 \pm 0.02$.

Model	M_{vir}	C	n	$r_{s/c}$	$\rho_{s/c}$
	$[10^{10} M_\odot]$	$[-]$	$[-]$	[kpc]	$[10^8 \ \mathrm{M_\odot \ kpc^{-3}}]$
NFW	6.0	15	–	8.04	9.00
NFW	2.0	15	–	5.58	9.00
NFW	10.0	15	–	9.54	9.00
NFW	6.0	12	–	10.05	5.15
NFW	6.0	20	–	6.03	18.71
ISO	6.0	15	–	8.04	1.22
ISO	2.0	15	–	5.58	1.22
ISO	10.0	15	–	9.54	1.22
ISO	6.0	12	–	10.05	0.80
ISO	6.0	20	–	6.03	2.12
EIN	6.0	15	2	8.04	5.17
EIN	2.0	15	2	5.58	5.17
EIN	10.0	15	2	9.54	5.17
EIN	6.0	12	2	10.05	2.66
EIN	6.0	20	2	6.03	1.22
EIN	6.0	15	5	8.04	2.34
EIN	6.0	15	1	8.04	8.94
EIN	6.0	15	0.5	8.04	13.76

TABLE 24: NFW, ISO, and Einasto Profile Parameters –
This table shows halo density profiles investigated in Figures 41 through 45. The three density profiles investigated are the NFW model, the pseudo-isothermal core model, and the Einasto model. Explainations of each halo model are in Appendix C.
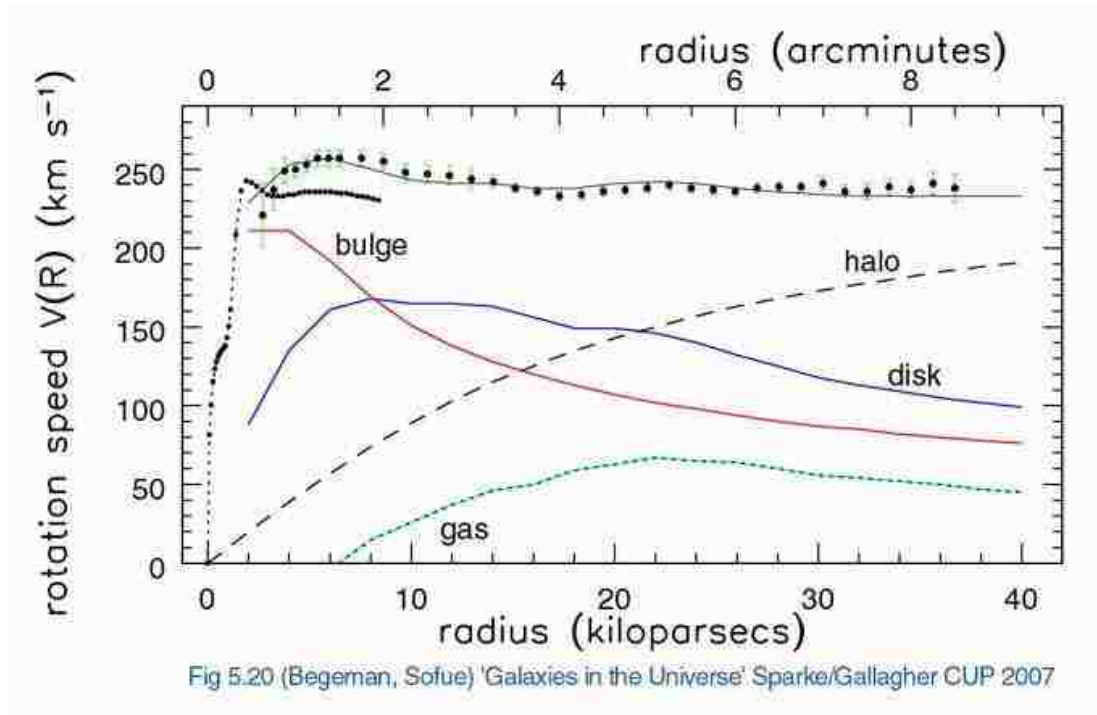
FIGURE 1: Rotation Curve of NGC 7331 –
This shows the rotation curve for spiral galaxy NGC 7331. The points show the total rotation curve derived from HI data and the dotted like show the total rotation curve for the inner 2 kpc derived from CO data. The lower solid curves show the contribution to the rotation curve from each component of the galaxy: the gas disk, the bulge, and the stellar disk. The dashed line is the contribution due to the dark matter halo. This component is needed in order to match the rotation curve to what is observed. This figure comes from Figure 5.20 in Sparke & Gallagher (2007) (data from K. Begeman and Y. Sofue). Credit/Premissions: Galaxies in the Universe by Linda S. Sparke and John S. Gallagher, III, Cambridge University Press, 2007. Reproduced with the written permission of Dr. Sparke for republish in this thesis.
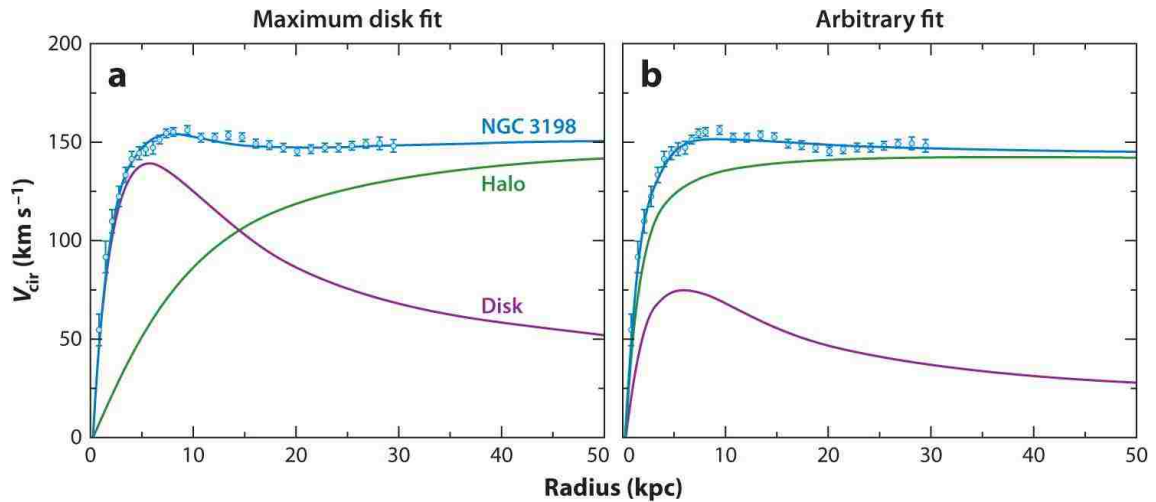
FIGURE 2: Rotation Curve of NGC 3198 –
This shows the rotation curve for LSB spiral disk galaxy NGC 3198. The points show
the total rotation curve derived from HI data, blue line was fit to the data. The
black curves show the contribution to the rotation curve from the disk and the red
line is the contribution due to the dark matter halo. Lacking more components, the
fit becomes easier. Panel a assumes the maximum disk fit; this fit maximizes the
amplitude of the disk rotation curve. The galaxy is dark matter dominated at the
outer radii for this fit. Panel b is an arbitrary fit (has a disk mass 0.3 times that
of the maximum disk fit). The galaxy is dark matter dominated at all radii with
this fit. This figure comes from Figure 12 in van der Kruit & Freeman (2011) (data
from van Albada et al. 1985). Credit/Premissions: Annual Review of Astronomy and
Astrophysics by Annual Reviews. Reproduced with permission of Annual Reviews in
the format Republish in a thesis/dissertation via Copyright Clearance Center.
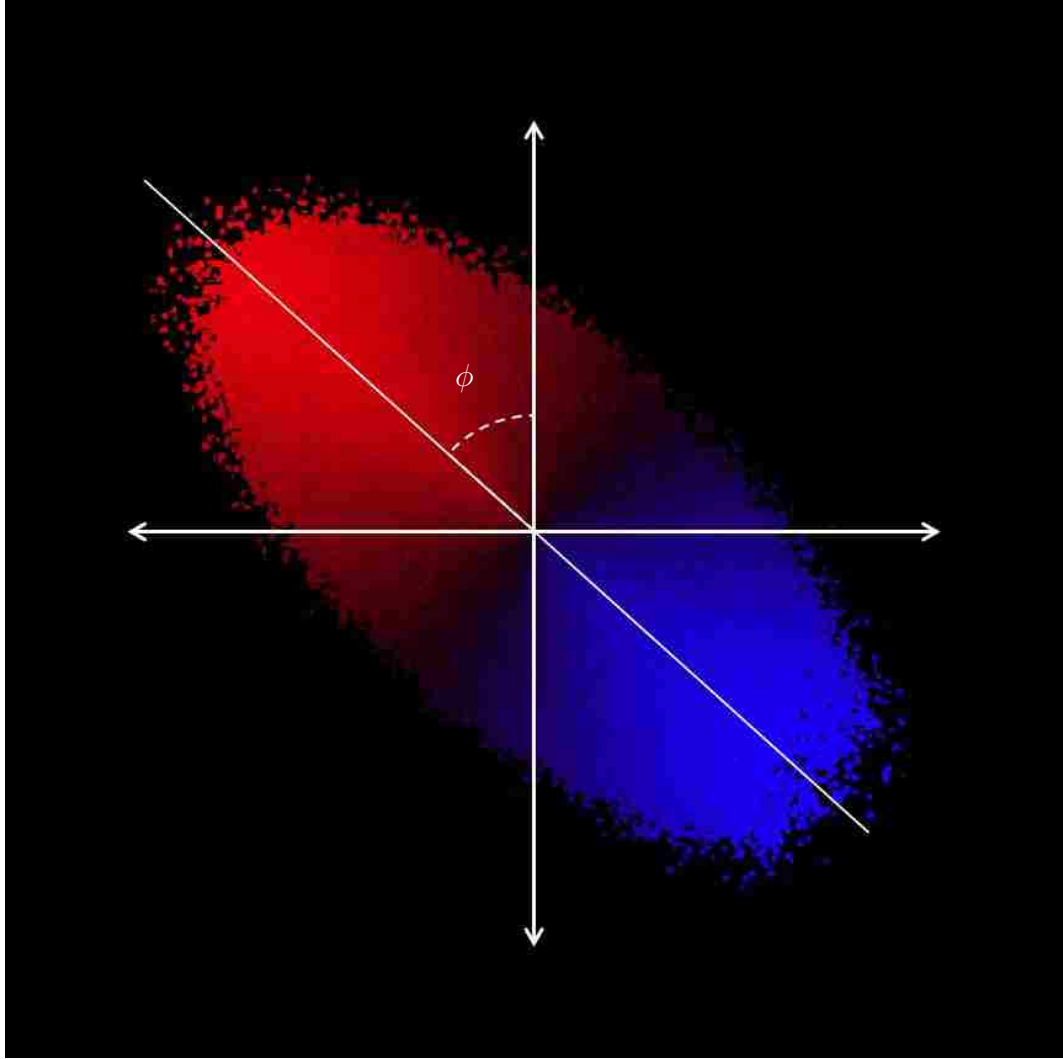
FIGURE 3: The Definition of Position Angle, ϕ –
The position angle is defined as the angle measured counterclockwise from the north direction in the sky to the major axis of the receding (red) side of the galaxy.
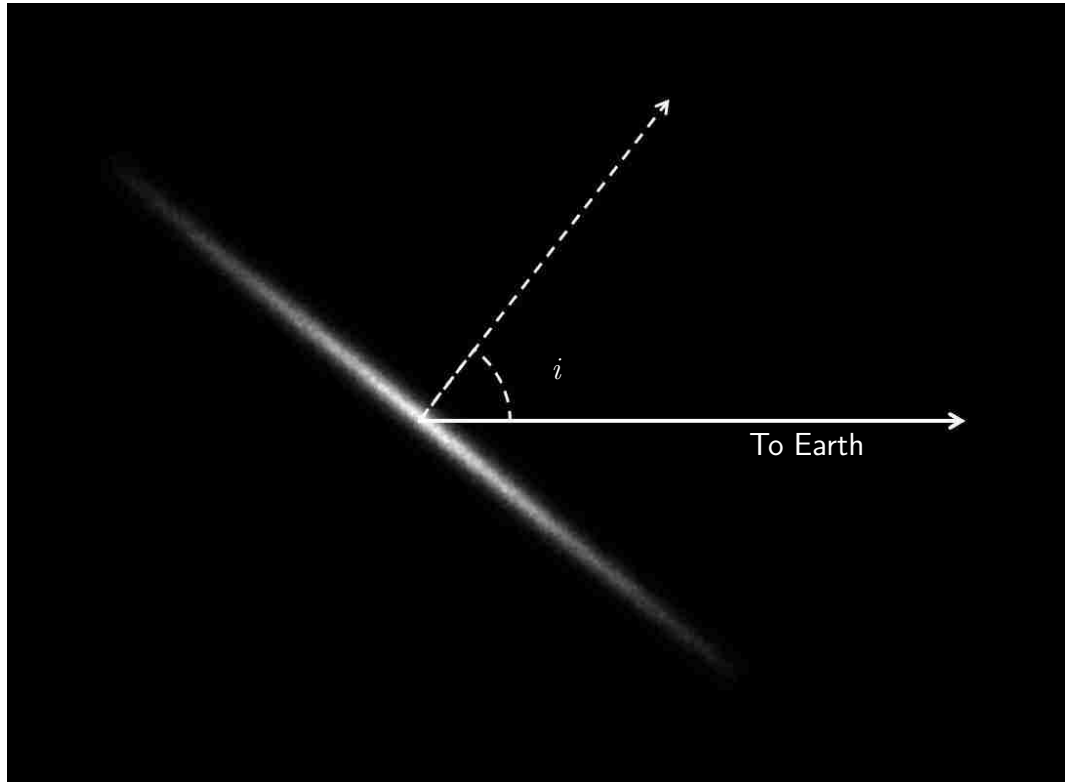
FIGURE 4: The Definition of Inclination Angle, i –
This shows a galaxy disk perpendicular to the line-of-sight. The inclination angle is defined as the angle between line-of-sight and a line normal to the plane of the galaxy.
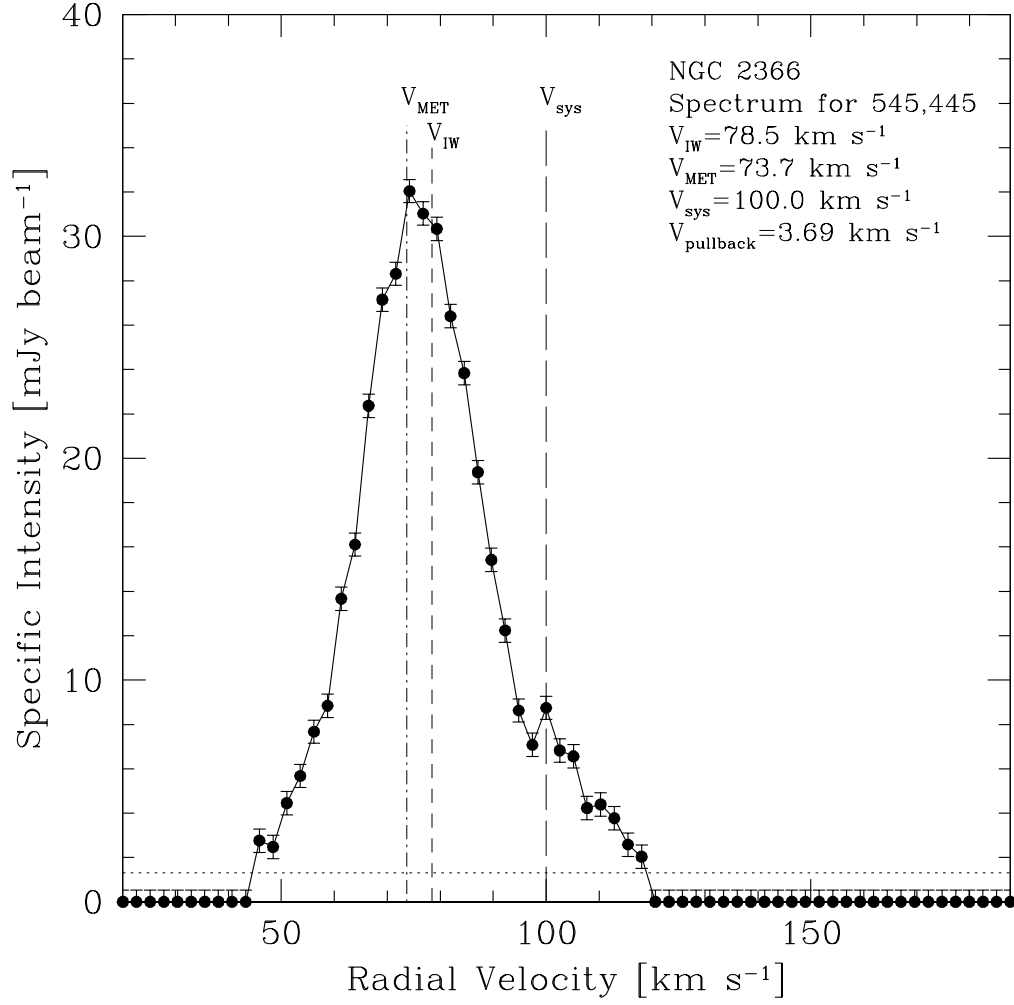
FIGURE 5: Example Spectrum from NGC 2366 –
Spectrum of location $(\alpha_{2000}, \delta_{2000}) = (12^h\ 54^m\ 01.3^s, +27°\ 07'\ 32.0")$ within NGC 2366.
The spectrum has velocites extracted from it using the intensity weighted (IW) and
modified envelope tracing (MET) method. V_{sys} and 2.5σ noise level is shown as well.
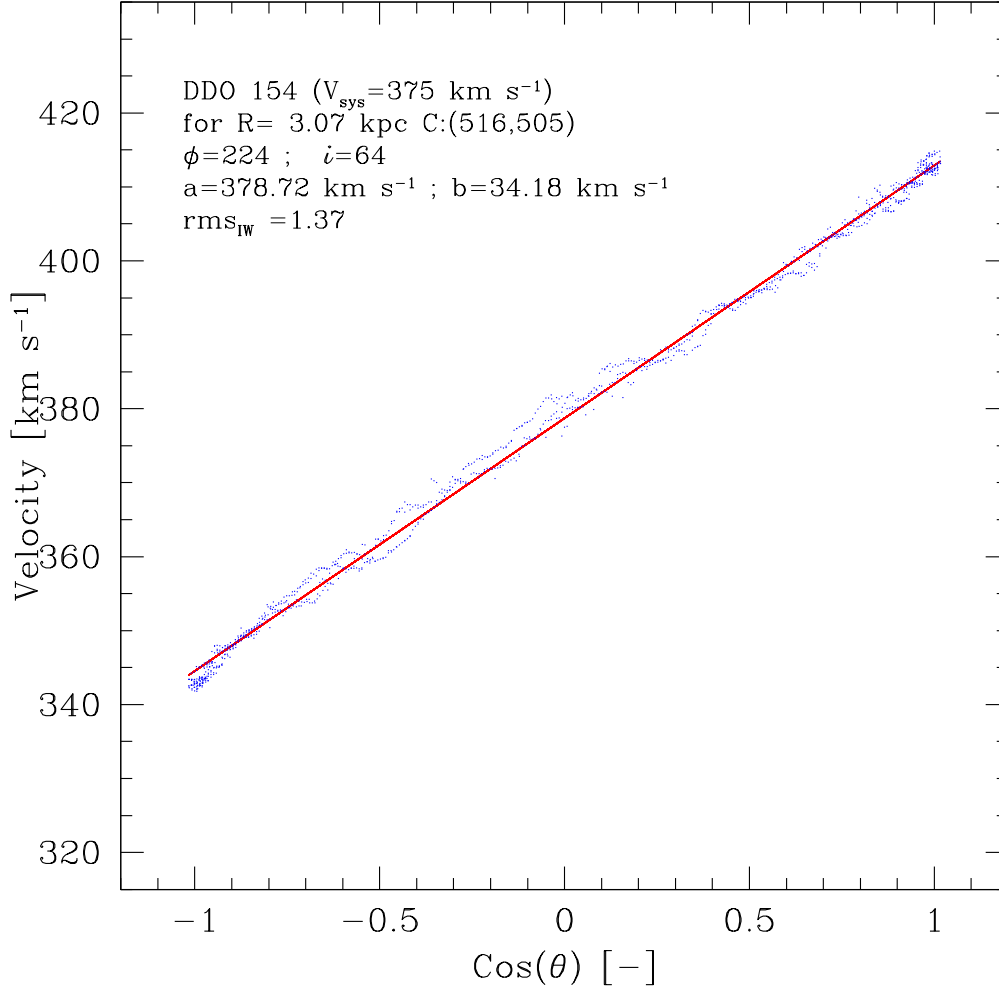
FIGURE 6: Cos(θ) vs Velocity Plot for a 3.07 kpc Annulus from DDO 154 –
This a cos(θ) vs velocity plot from DDO 154 for an annulus of radius 3.07 kpc centered
on (α_{2000}, δ_{2000})=(07^h 28^m 45.6^s, +69° 11' 14.6"). Blue point are sky positions within
the annulus. The velocity comes from the spectra, in this case extracted with the
intensity weighted (IW) method. Cos(θ) represent their location within the annulus.
The red line is the fit to these points (Equation 2.2); the a and b fit parameters are
shown. Error bars have been left off in order to see the locations of the points as this
plot contains over a thousand points.
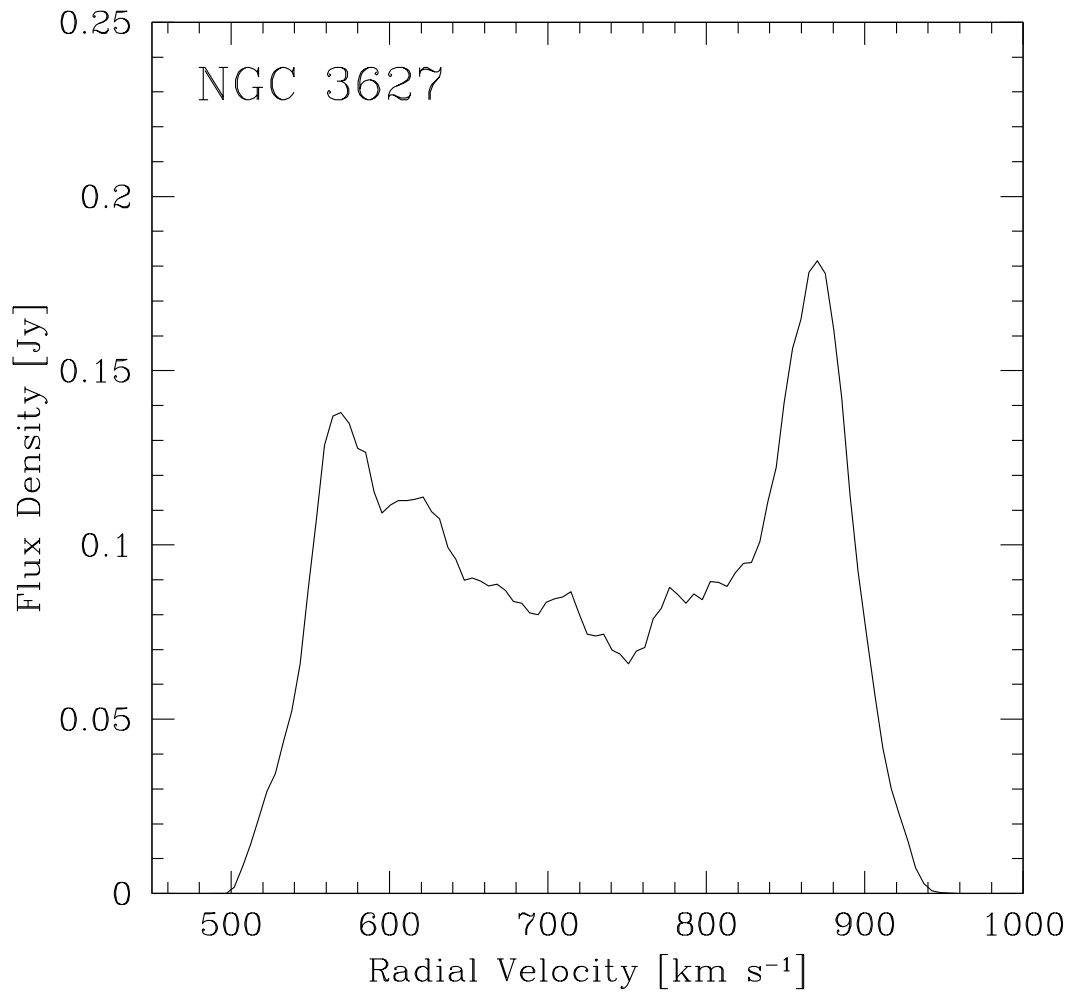
FIGURE 7: The Global H I Profile for NGC 3627 –
The Global H I profile for the galaxy NGC 3627. This galaxy exhibits the 'double horned' feature on the red and blue sides of the spectra. The integral of this graph is the total flux density, $\mathcal{S}_{HI}$ reported in Table 6.
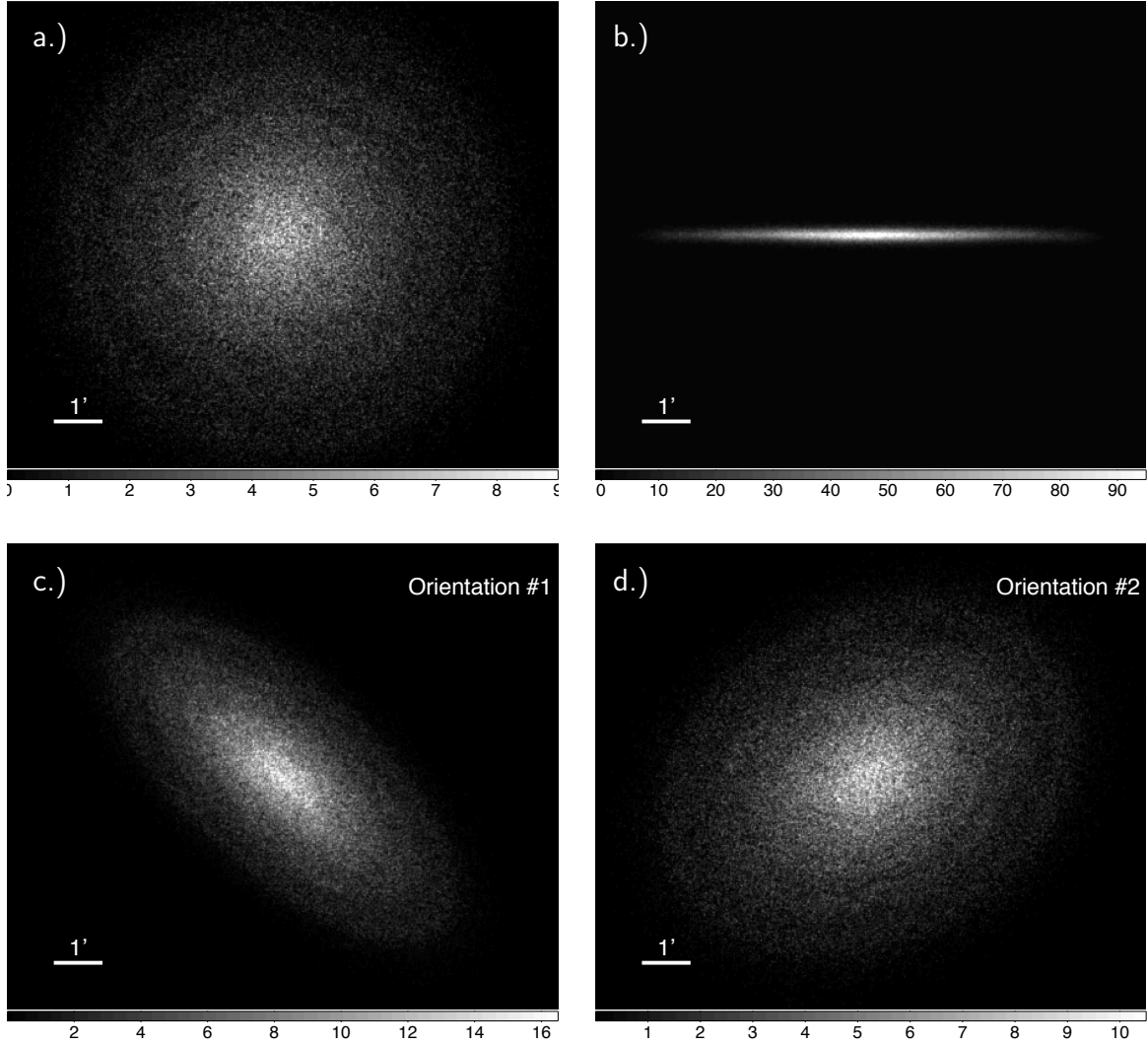
FIGURE 8: N-Body Simulation of a Disk Galaxy –
a.) Simulated galaxy in a face on orientation ($i = 0°$). b.) Simulated galaxy in a edge on orientation ($\phi = 90°$, $i = 90°$). c.) Simulated galaxy in orientation #1 ($\phi = 48°$, $i = 65°$). d.) Simulated galaxy in orientation #2 ($\phi = 300°$, $i = 42°$).
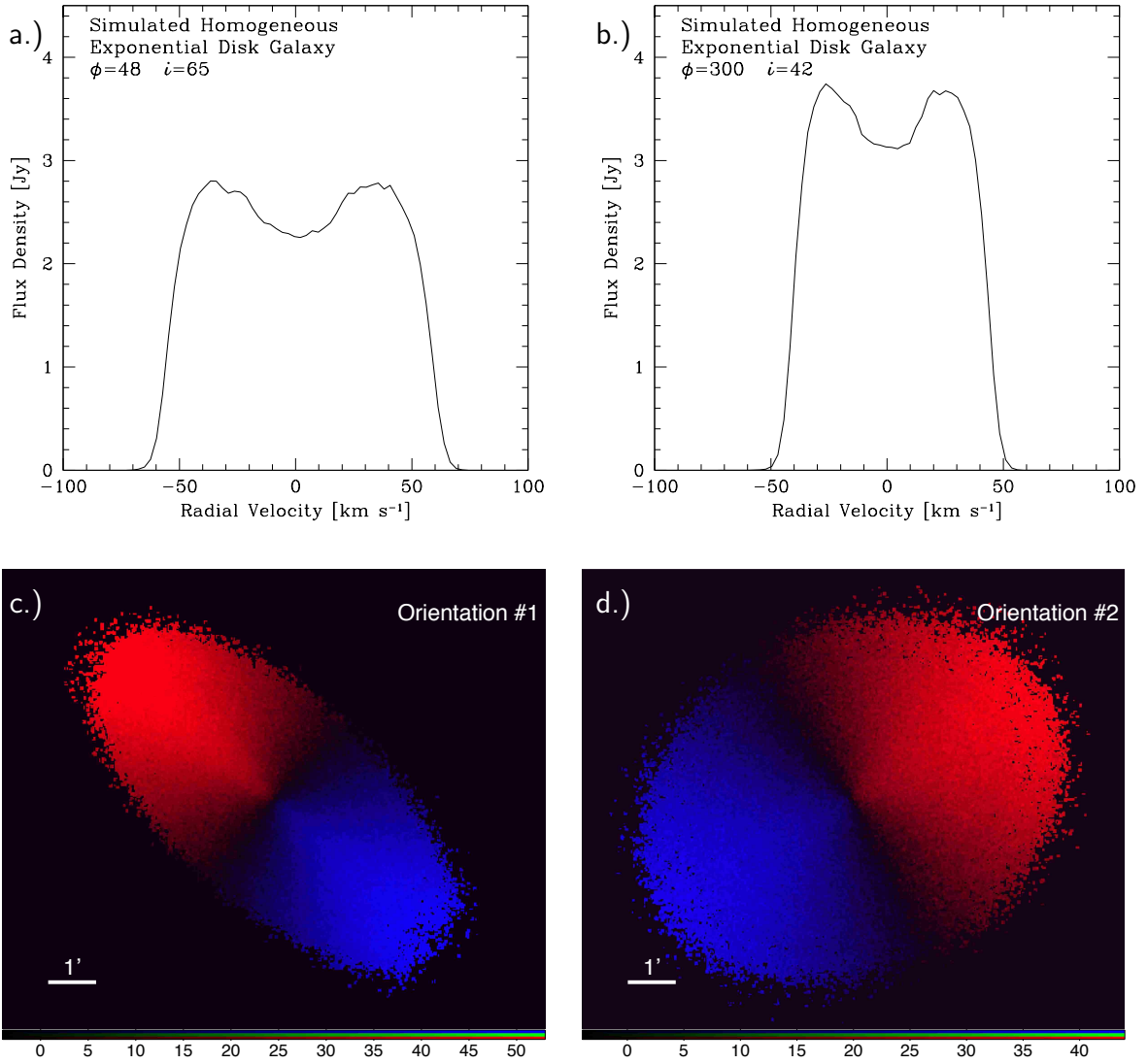
FIGURE 9: Hɪ Profile and Velocity Contours for the N-Body Simulation in Two Orientations –

a.) Global Hɪ profile of the simulated galaxy with orientation: ($\phi = 48°$, $i = 65°$). b.) Global Hɪ profile of the simulated galaxy with orientation: ($\phi = 300°$, $i = 42°$). In each orientation, notice the 'double horned' feature on the red and blue sides of the spectrum. c. and d.) The velocity maps for the simulated galaxy with orientations ($\phi = 48°$, $i = 65°$) and ($\phi = 300°$, $i = 42°$), respectively.
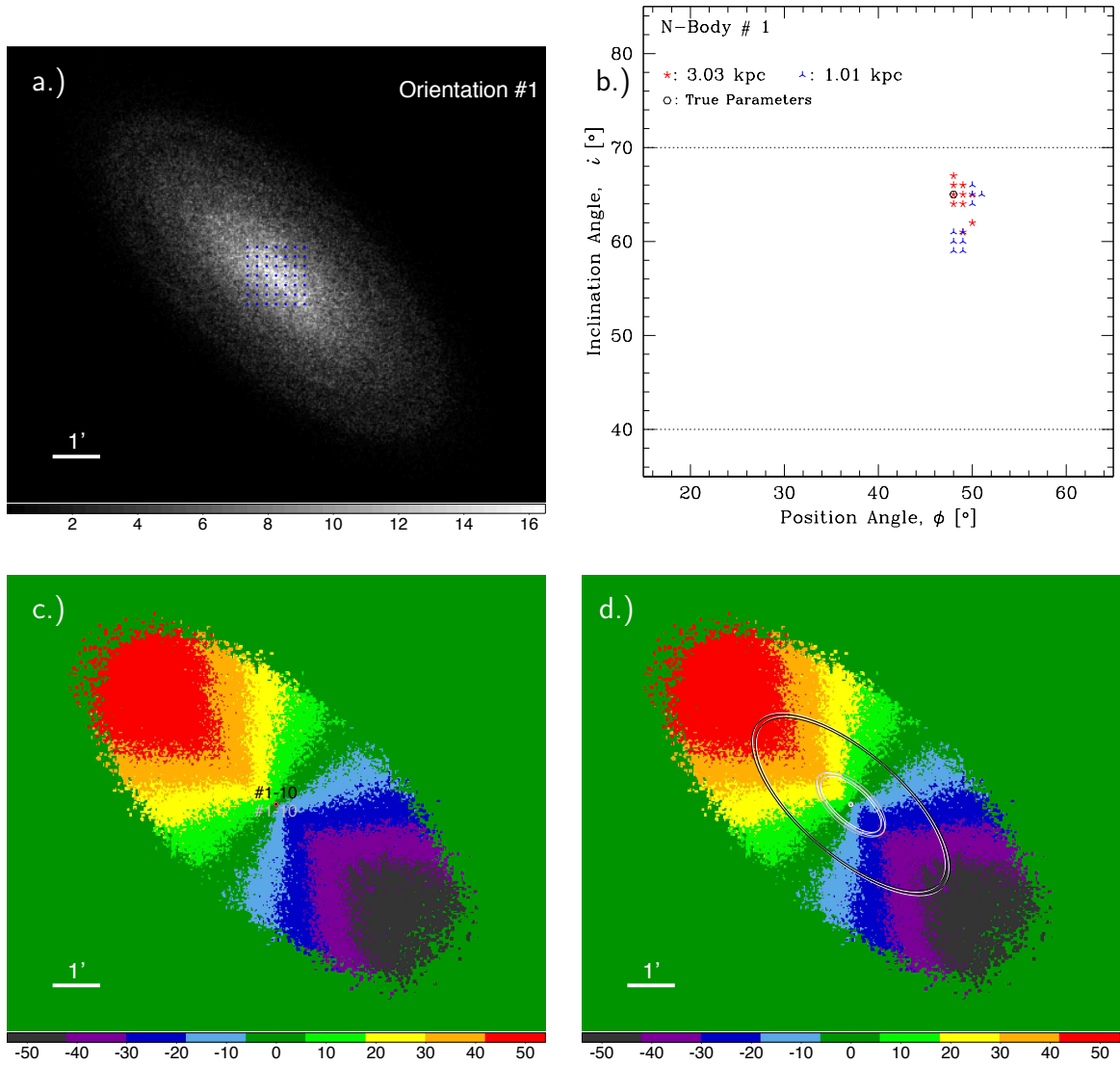
FIGURE 10: N-Body Orientation #1 – Results

a.) The center search sample area of 49 centers used for the simulated galaxy with ($\phi = 48°$, $i = 65°$). The parameter space of position and inclination angles is investigated each of these centers. Each center is separated by approximately 0.25 kpc in the x and y direction. b.) A plot showing the orientation parameters for the ten lowest RMS$_{IW}$ of the IW search for both annuli. The dotted lines show the allowable limits of i. c.) An image showing the velocity field derived using the intensity weighted (IW) method with the center locations for the ten lowest RMS$_{IW}$ of the IW search for both annuli. Each color bin is 12 km s^{-1} wide. d.) An image showing the model parameters using the lowest RMS$_{IW}$ for both annuli and for the true parameters.
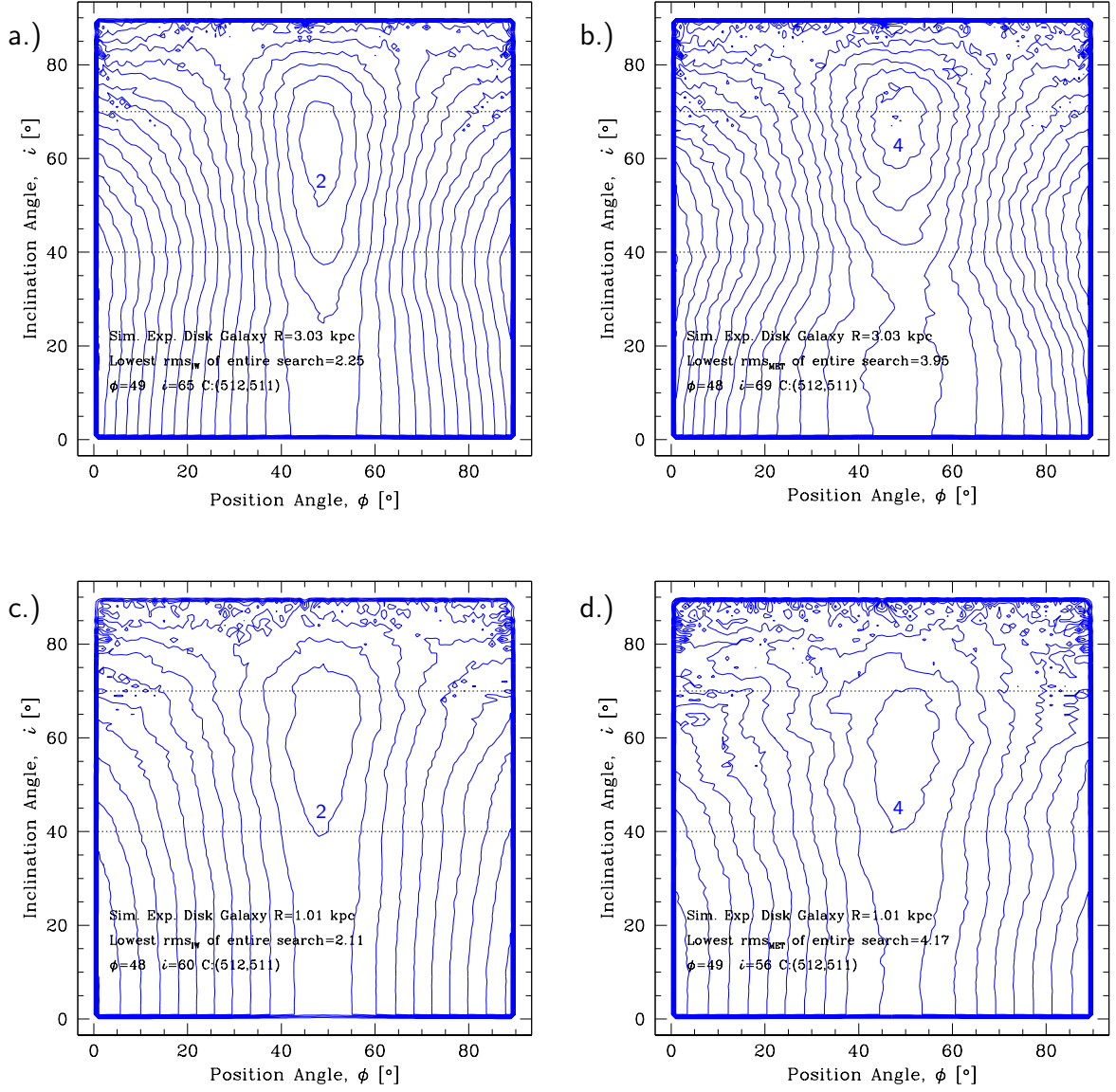
FIGURE 11: N-Body Orientation #1 – RMS Contour Plots for 3.03 kpc and 1.01 kpc Annuli using IW and MET Methods

RMS contour plots for the simulated galaxy with ($\phi = 48°$, $i = 65°$). The dotted lines show the allowable limits of i. The lowest contour is labeled and increase in increments of 1 km sec^{-1}: a.) for the center which contains the lowest RMS value found using the IW method with an annulus of radius 3.03 kpc. b.) for the center which contains the lowest RMS value found using the MET method with an annulus of radius 3.03 kpc. The second lowest contour is labeled. The small contour near the center of the labeled contour is the lowest. c.) for the center which contains the lowest RMS value found using the IW method with an annulus of radius 1.01 kpc. d.) for the center which contains the lowest RMS value found using the MET method with an annulus of radius 1.01 kpc.
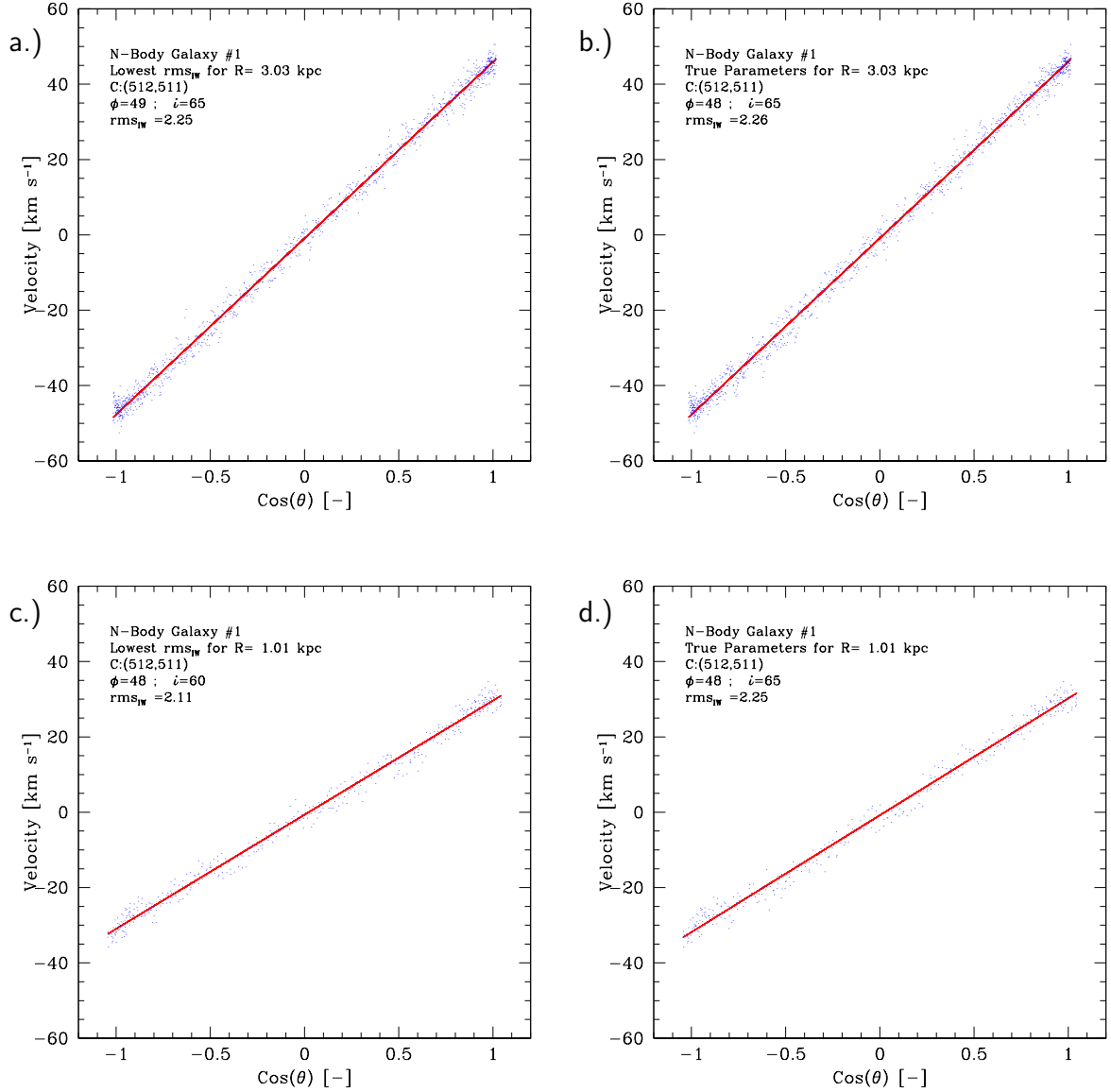
FIGURE 12: N-Body Orientation #1 – Cos(θ) vs Velocity Plots for 3.03 kpc and 1.01 Annuli

These are the $\cos(\theta)$ vs velocity plots used for finding the circular velocity for an annulus of the simulated galaxy with ($\phi = 48°$, $i = 65°$). Error bars have been left off in order to see the locations of the points as each plot contains several hundred points. a.) This plot shows the parameters corresponding to the lowest RMS_{IW} for the 3.03 kpc annulus. b.) This plot shows the true parameters for a 3.03 kpc ring. a.) This plot shows the parameters corresponding to the lowest RMS_{IW} for the 1.01 kpc annulus. b.) This plot shows the true parameters for a 1.01 kpc ring.
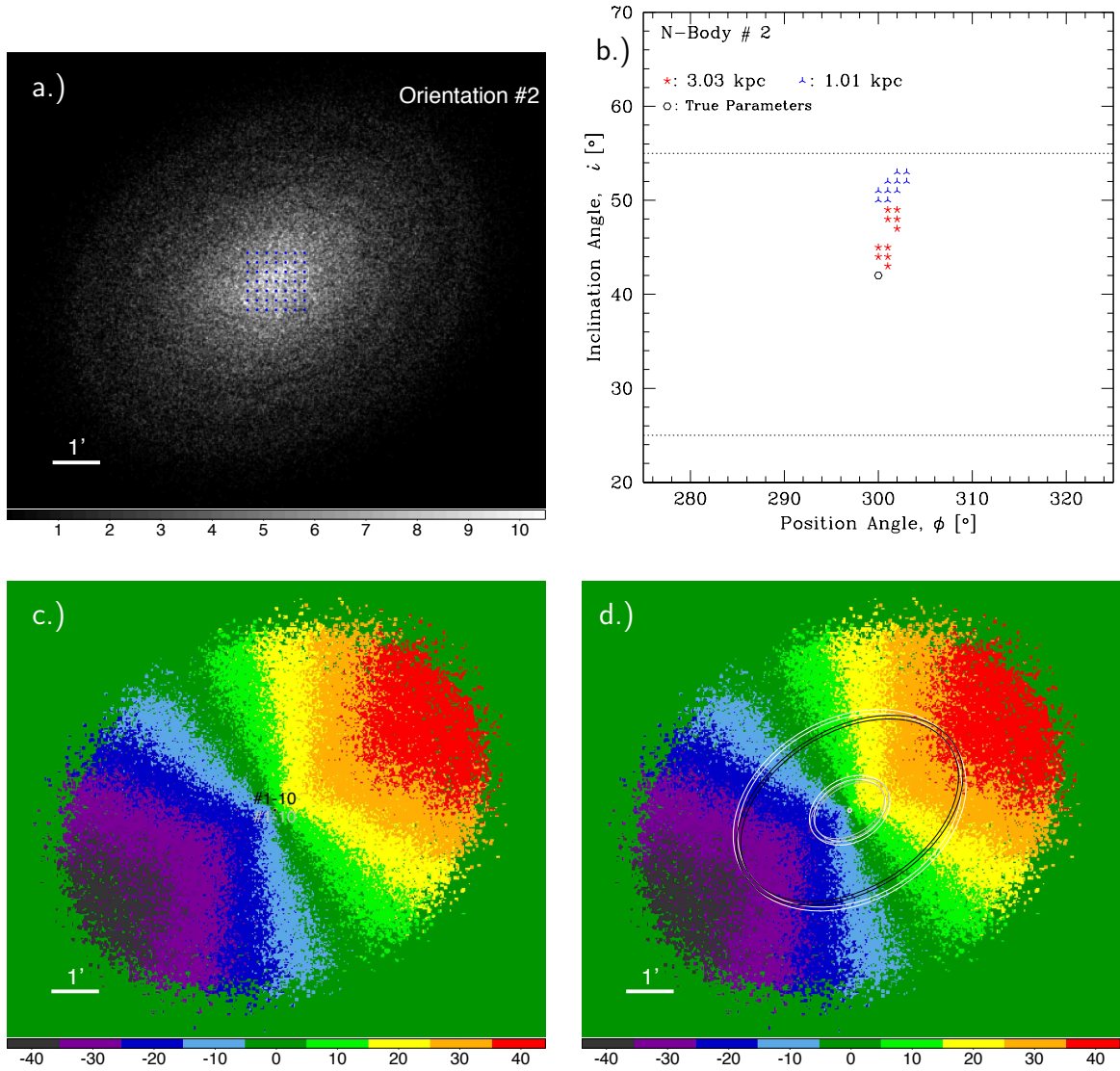
FIGURE 13: N-Body Orientation #2 – Results
a.) The center search sample area of 49 centers used for the simulated galaxy with
($\phi = 300°$, $i = 42°$). The parameter space of position and inclination angles is
investigated each of these centers. Each center is separated by approximately 0.25
kpc in the x and y direction. b.) A plot showing the orientation parameters for
the ten lowest RMS_{IW} of the IW search for both annuli. The dotted lines show
the allowable limits of i. c.) An image showing the velocity field derived using the
intensity weighted (IW) method with the center locations for the ten lowest RMS_{IW}
of the IW search for both annuli. Each color bin is 10 km s^{-1} wide. d.) An image
showing the model parameters using the lowest RMS_{IW} for both annuli and for the
true parameters.
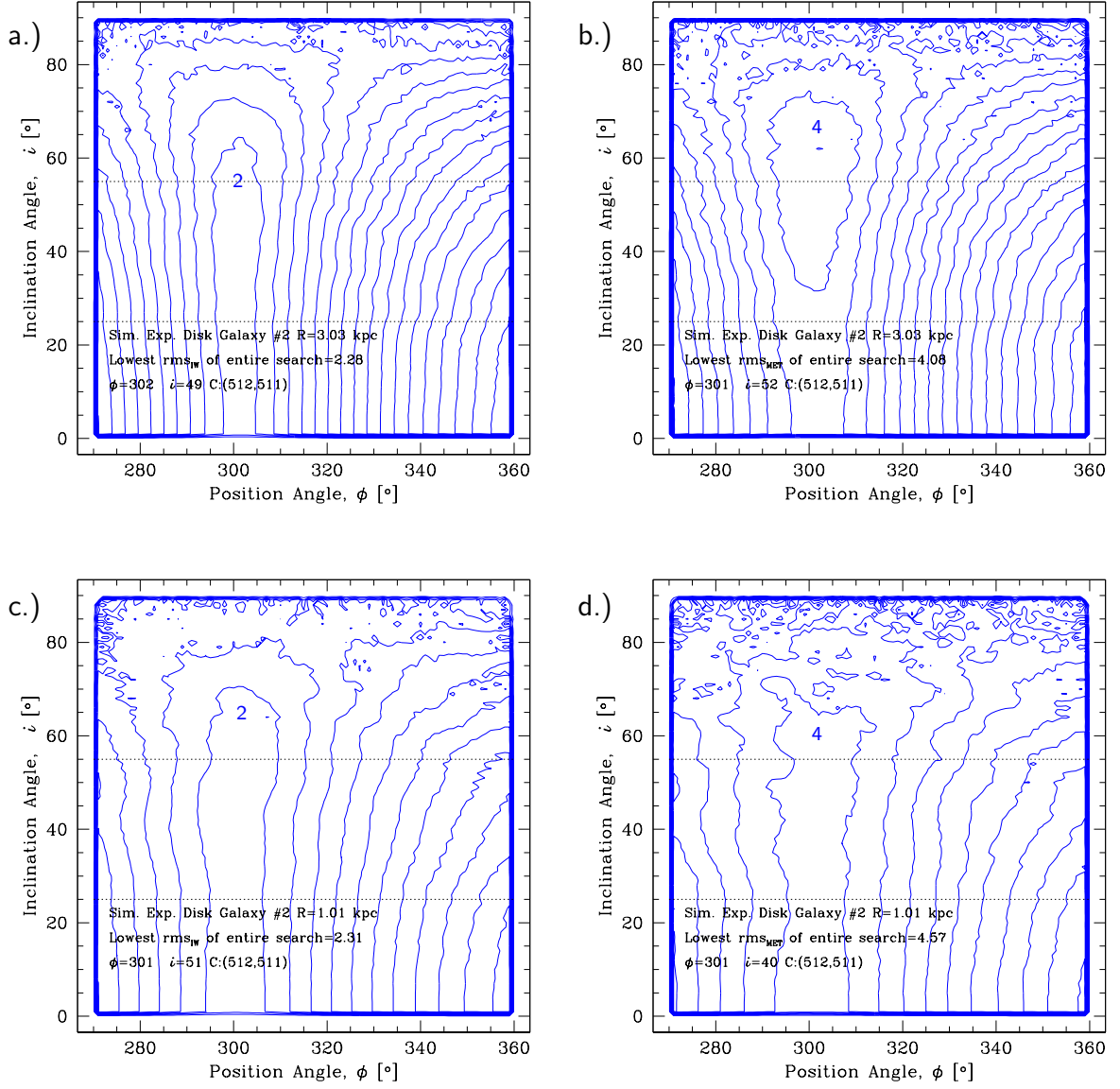
FIGURE 14: N-Body Orientation #2 – RMS Contour Plots for 3.03 kpc and 1.01 kpc Annuli using IW and MET Methods

RMS contour plots for the simulated galaxy with ($\phi = 300°$, $i = 42°$). The dotted lines show the allowable limits of i. The lowest contour is labeled and increase in increments of 1 km sec^{-1}: a.) for the center which contains the lowest RMS value found using the IW method with an annulus of radius 3.03 kpc. b.) for the center which contains the lowest RMS value found using the MET method with an annulus of radius 3.03 kpc. The second lowest contour is labeled. The tiny contour above i=60° is outside the acceptable range based on physical motivations. c.) for the center which contains the lowest RMS value found using the IW method with an annulus of radius 1.01 kpc. d.) for the center which contains the lowest RMS value found using the MET method with an annulus of radius 1.01 kpc.
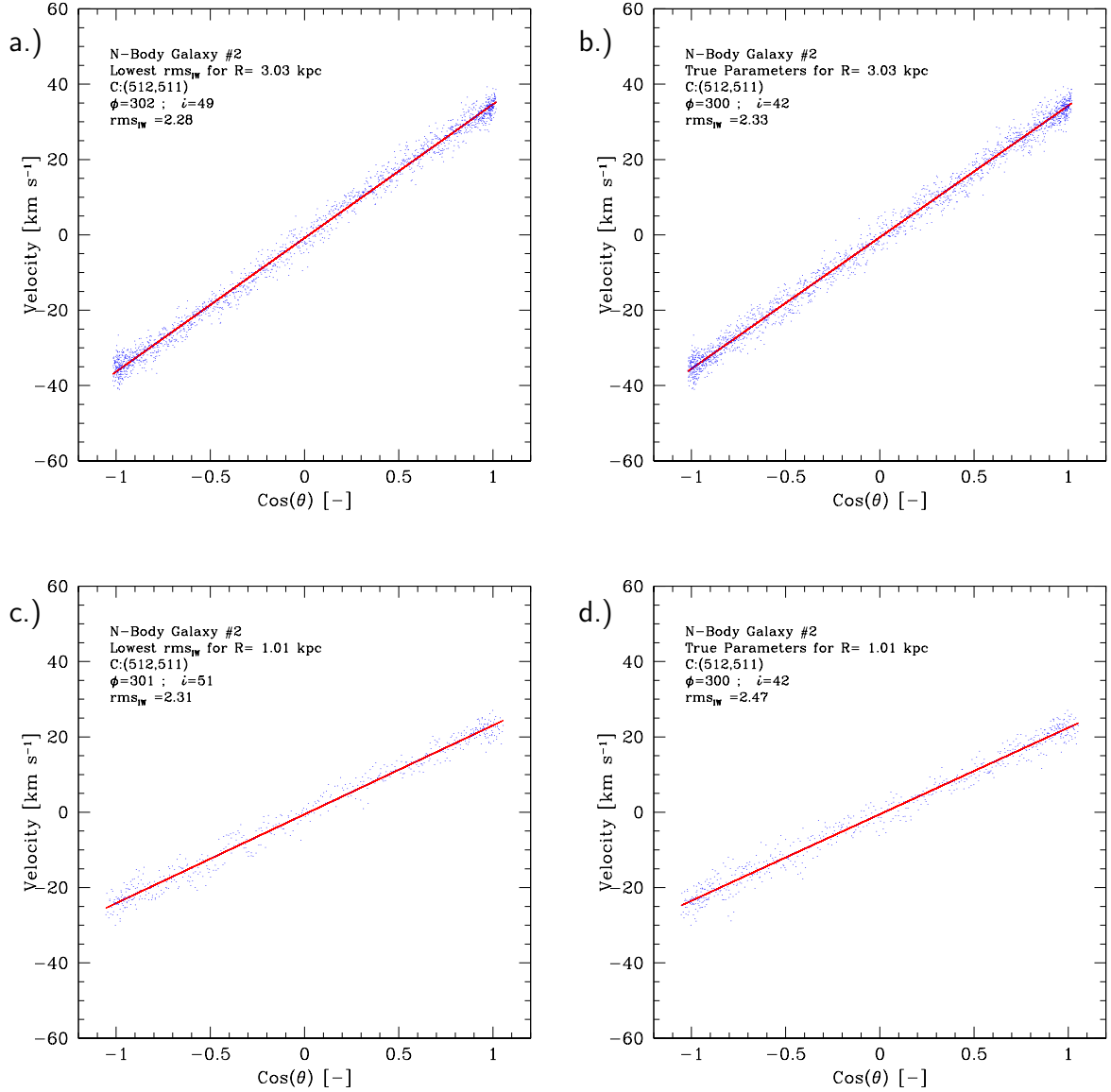
FIGURE 15: N-Body Orientation #2 – Cos(θ) vs Velocity Plots for 0.94 kpc and 0.78 Annuli

These are the cos(θ) vs velocity plots used for finding the circular velocity for an annulus of the simulated galaxy with ($\phi = 300°$, $i = 42°$). Error bars have been left off in order to see the locations of the points as each plot contains several hundred points. a.) This plot shows the parameters corresponding to the lowest RMS$_{IW}$ for the 3.03 kpc annulus. b.) This plot shows the true parameters for a 3.03 kpc ring. c.) This plot shows the parameters corresponding to the lowest RMS$_{IW}$ for the 1.01 kpc annulus. d.) This plot shows the true parameters for a 1.01 kpc ring.
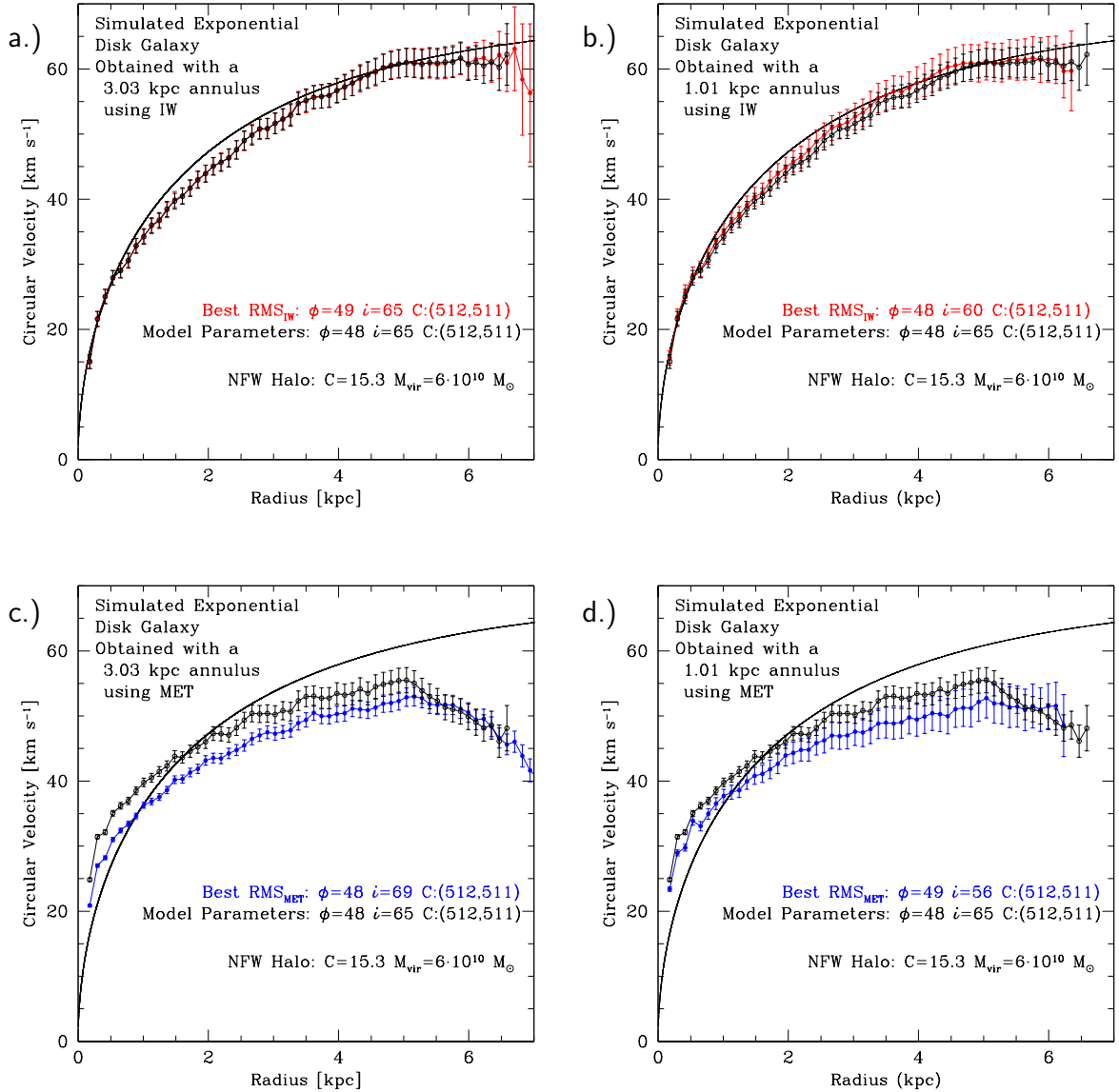
FIGURE 16: N-Body Orientation #1 – Rotation Curves with Results for 3.03 kpc and 1.01 kpc Annuli

In all plots the black line is true circular velocity derived from the NFW halo model. a.) Rotation curve with parameters corresponding to the lowest RMS for the IW method for the 3.03 kpc annulus. Red points correspond to the data, while black points correspond to the true parameters. b.) Rotation curve with parameters corresponding to the lowest RMS for the IW method for the 1.01 kpc annulus. Red points correspond to the data, while black points correspond to the true parameters. c.) Rotation curve with parameters corresponding to the lowest RMS for the MET method for the 3.03 kpc annulus. Blue points correspond to the data, while black points correspond to the true parameters. d.) Rotation curve with parameters corresponding to the lowest RMS for the MET method for the 1.01 kpc annulus. Blue points correspond to the data, while black points correspond to the true parameters.
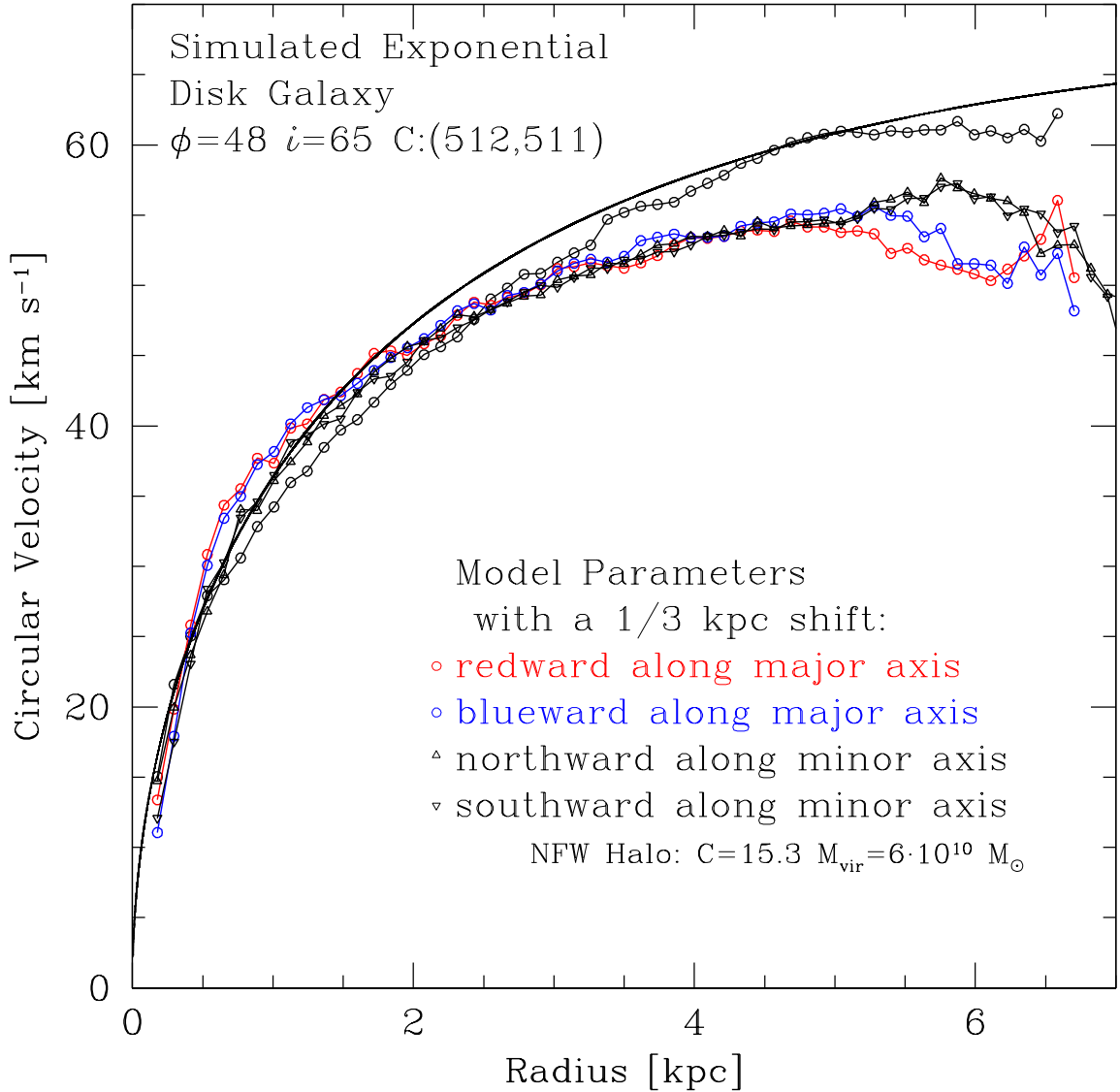
FIGURE 17: N-Body Orientation #1 – Effect of Shifting the Dynamic Center on the Inferred Rotation Curve

Rotation curve derived with the IW method and adopting the true orientation parameters and various centers. The open points correspond to setting the model center to the true center of the galaxy. The blue and red points correspond to shifting the model center a third of a kiloparsec blueward and redward along the major axis, respectively. The up and down triangles correspond to shifting the model center a third of a kiloparsec northward and southward along the minor axis, respectively. The solid black line is true circular velocity derived from the NFW halo model. Error bars were left off for ease of reading.
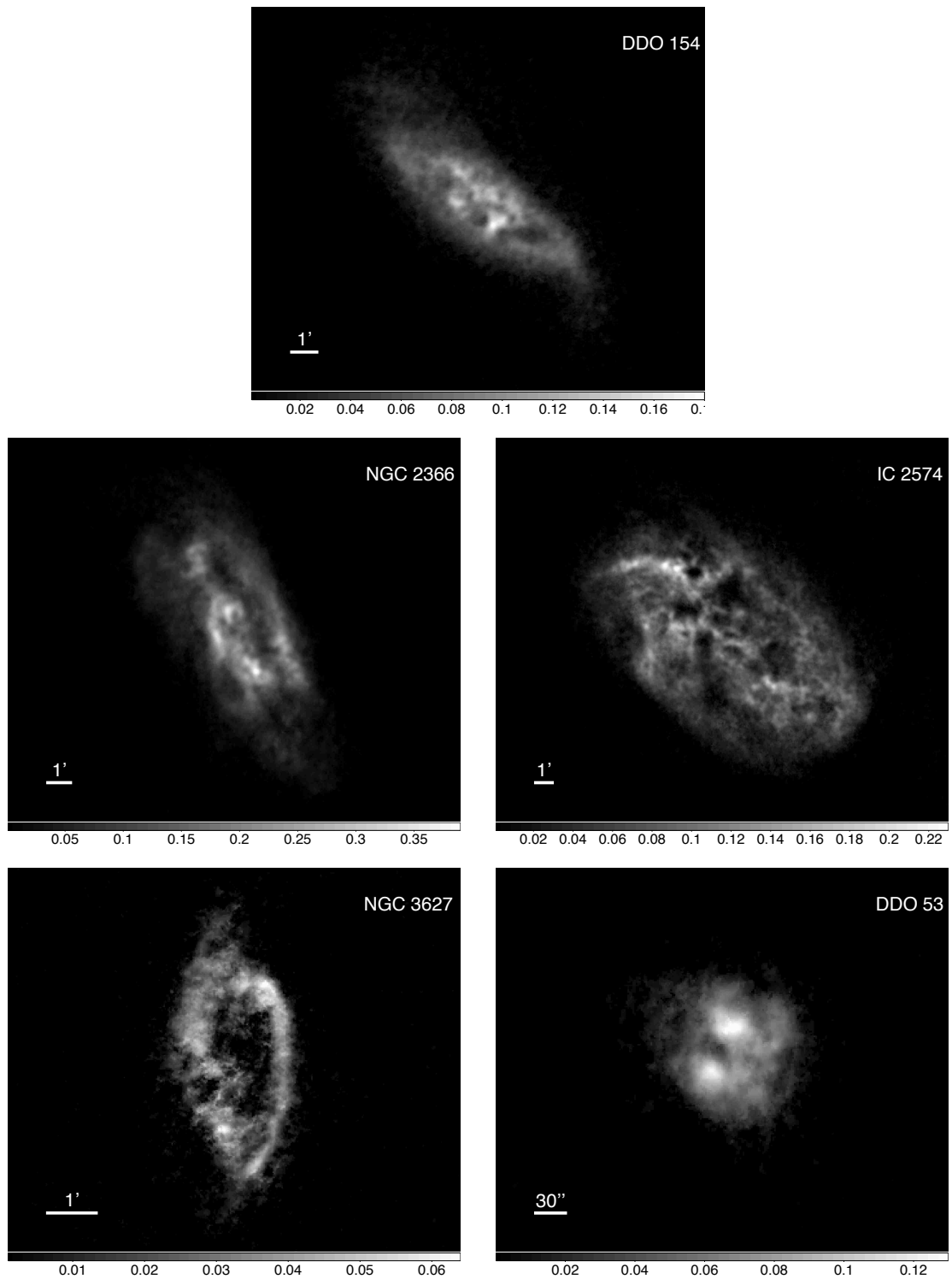
FIGURE 18: The Galaxy Sample-
The integrated Hɪ maps (moment 0) for the galaxy sample. The data come from
(Walter et al. 2008). These made after cleaning the data cubes.
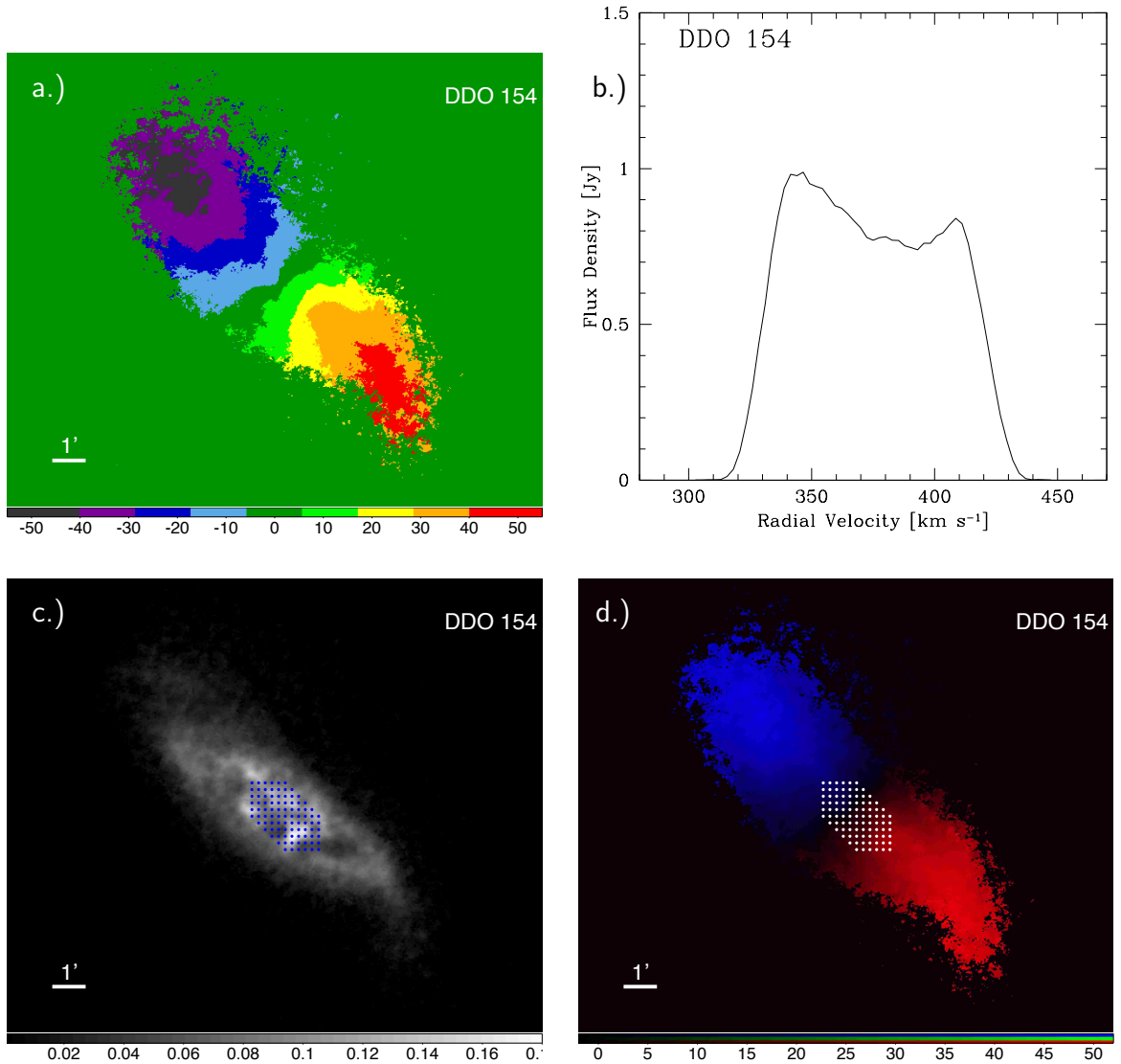
FIGURE 19: DDO 154-

a.) This is the velocity field (moment 1) for DDO 154 derived using the intensity weighted (IW) method. Each color bin is about 11.5 km s^{-1} wide. b.) The Global H\textsc{i} profile for DDO 154. c.) The center search sample area containing 91 centers overlaid onto the integrated H\textsc{i} map. The parameter space of position and inclination angles is investigated each of these centers. Each center is separated by approximately 0.233 kpc in α and δ. d.) The center search overlaid onto a continuous velocity field; the more vibrant blue and red are the locations of the strongest rotation.
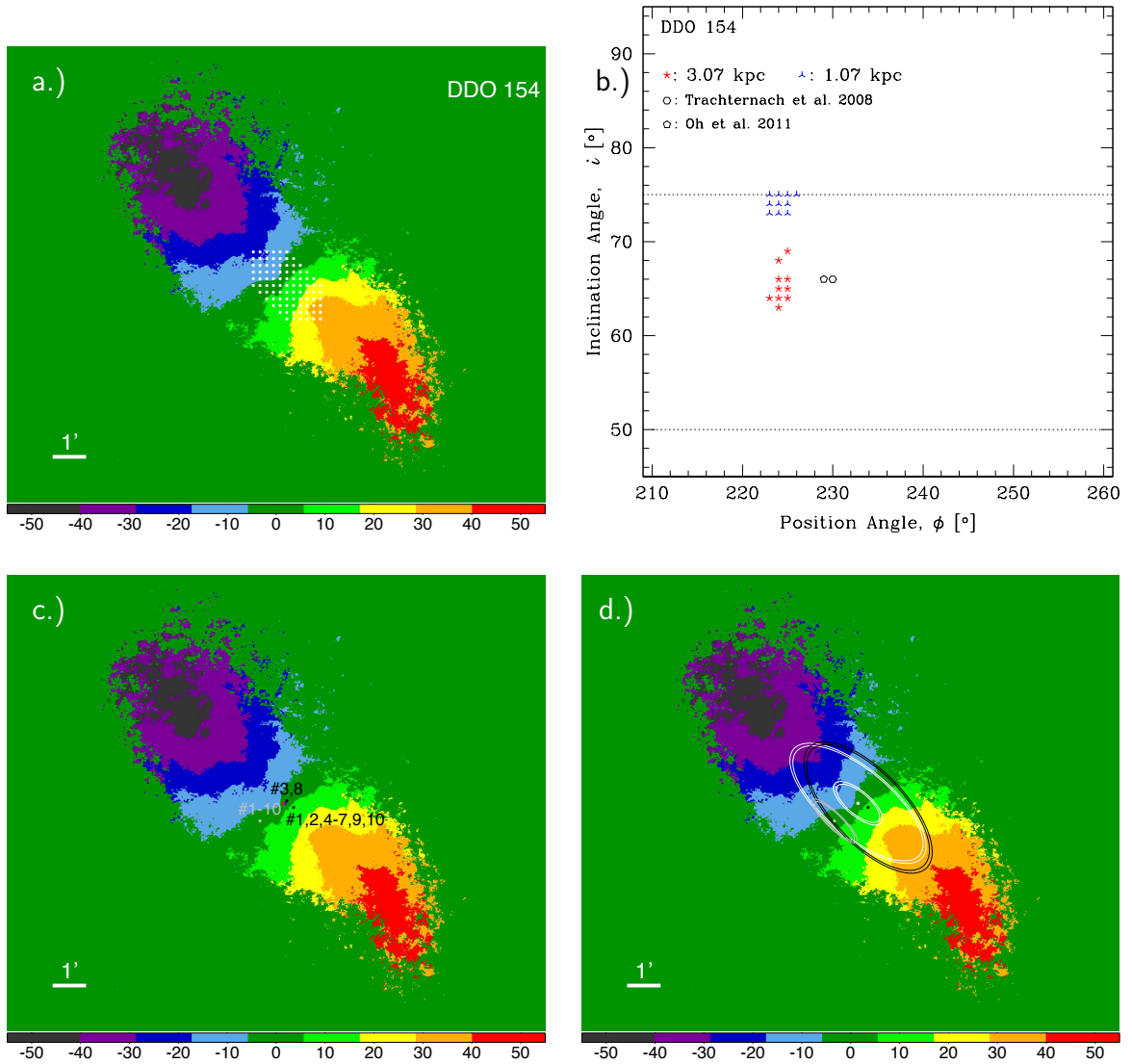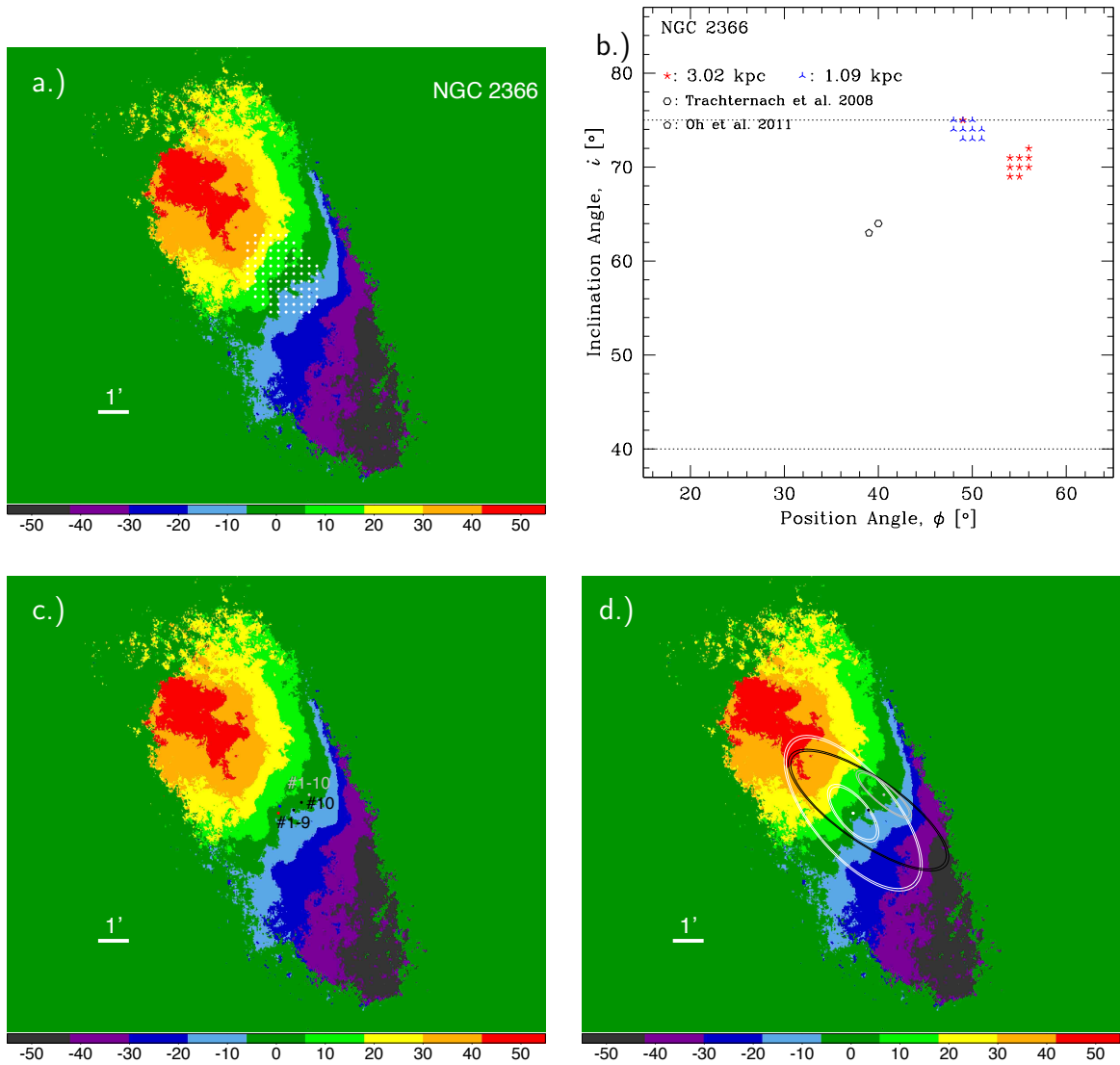
FIGURE 20: DDO 154 – Results

a.) The center search sample area for DDO 154 of 91 centers overlaid onto integrated H I map. The parameter space of position and inclination angles is investigated each of these centers. Each center is separated by approximately 0.233 kpc in α and δ. b.) A plot showing the orientation parameters for the ten lowest RMS_{IW} of the IW search for both annuli. The dotted rectangle shows the allowable limits of ϕ and i. c.) An image showing the center locations for the ten lowest RMS_{IW} of the IW search for the 3.07 kpc annulus (black) and the 1.07 kpc annulus (grey) overlaid onto the velocity field. Centers reported by Oh et al. (2008) (blue) and Trachternach et al. (2008) (red) are also included, for this galaxy these two points are near the same location. d.) An image showing the model parameters using the lowest RMS_{IW} for the 3.07 annulus (black), the 1.07 annulus (grey), and for parameters taken from Trachternach et al. (2008) (white for both annuli).
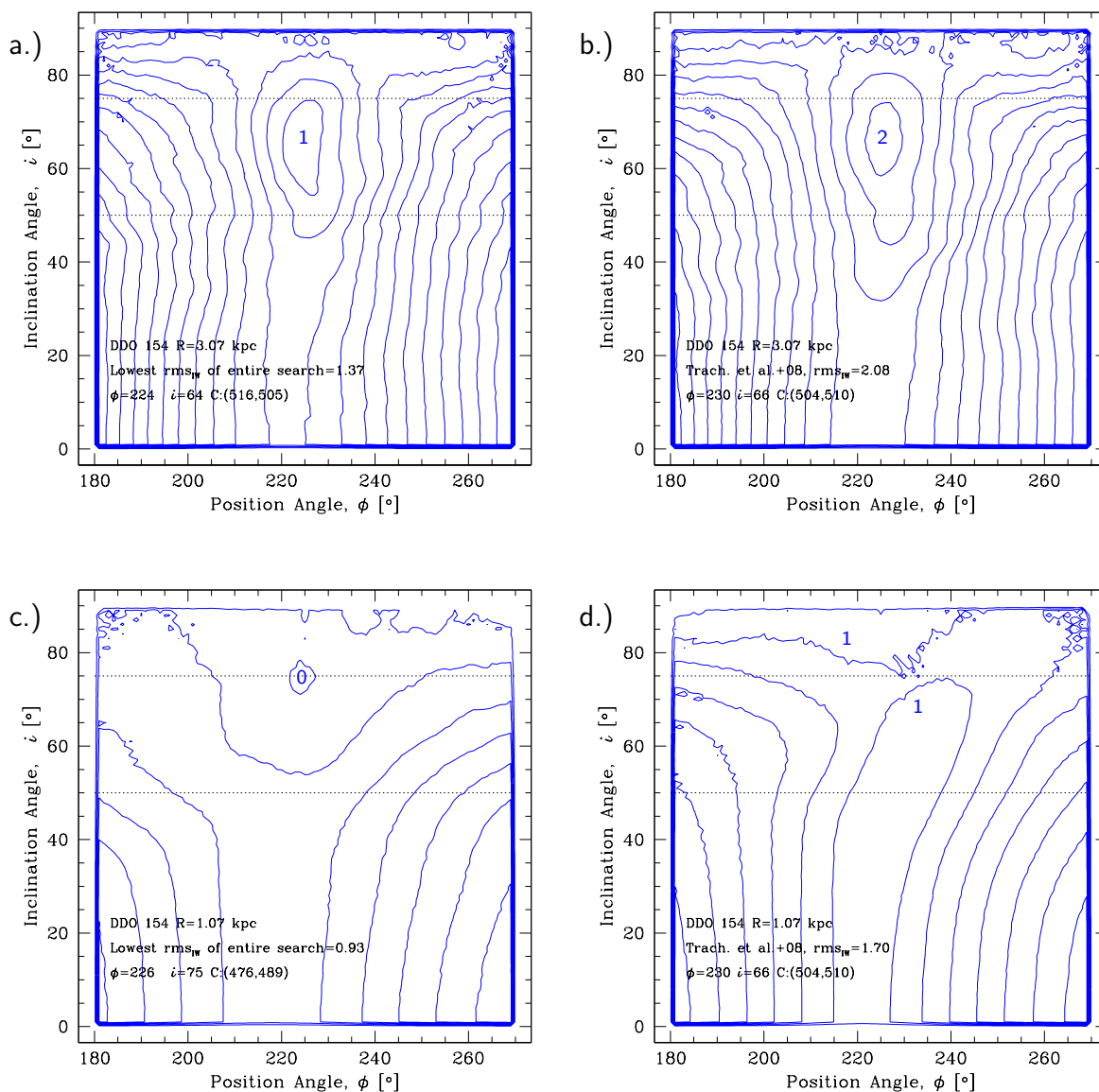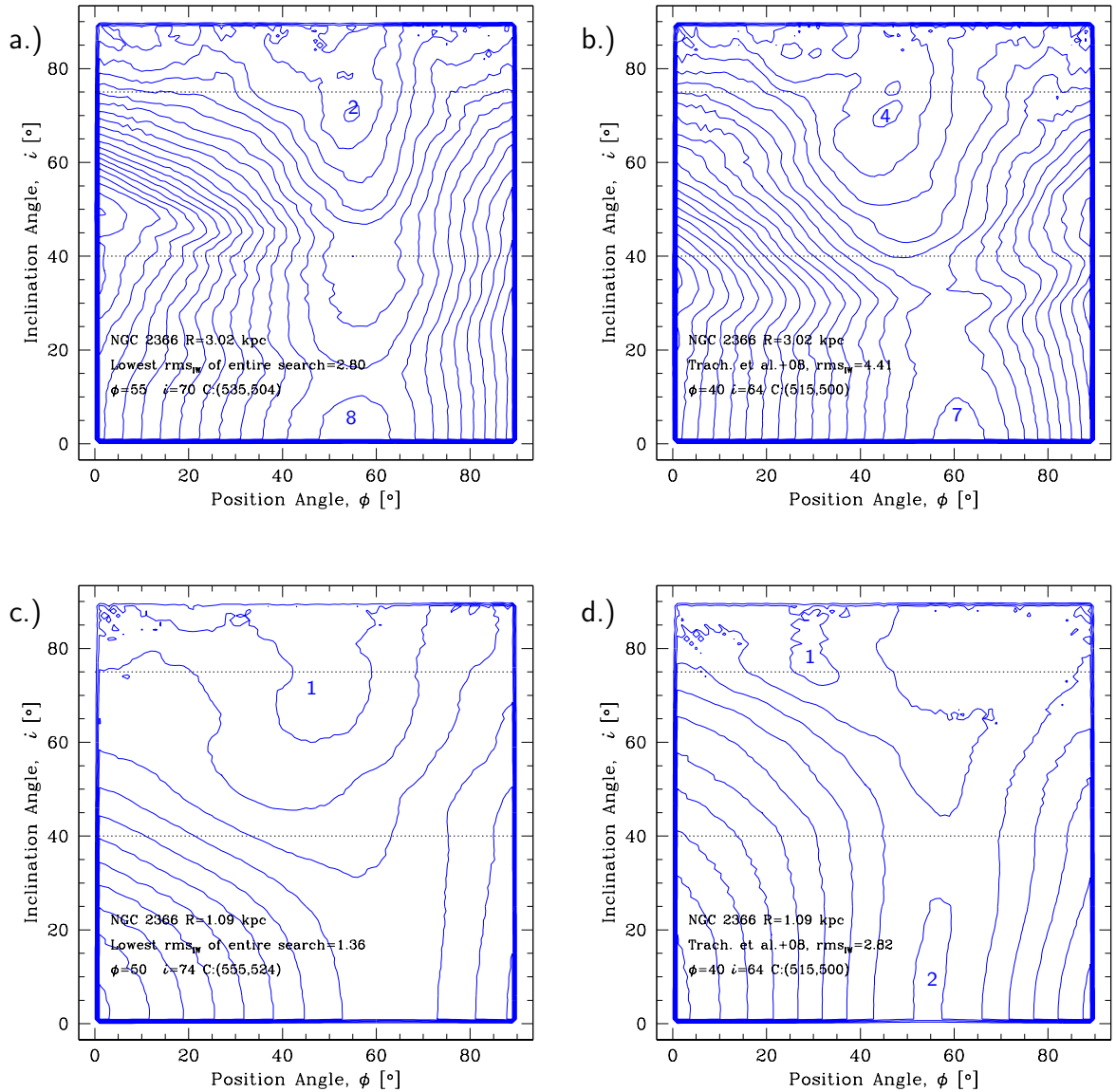
FIGURE 21: DDO 154 – RMS Contour Plots for 3.07 kpc and 1.07 kpc Annuli
The dotted lines show the allowable limits of i. The lowest contour for each are labeled and increase in increments of 1 km sec^{-1}: a.) for the center which contains the lowest RMS value found using the IW method with 3.07 kpc annulus. b.) using the center from Trachternach et al. (2008) with 3.07 kpc annulus. c.) for the center which contains the lowest RMS value found using the IW method with 1.07 kpc annulus. d.) using the center from Trachternach et al. (2008) with 1.07 kpc annulus.
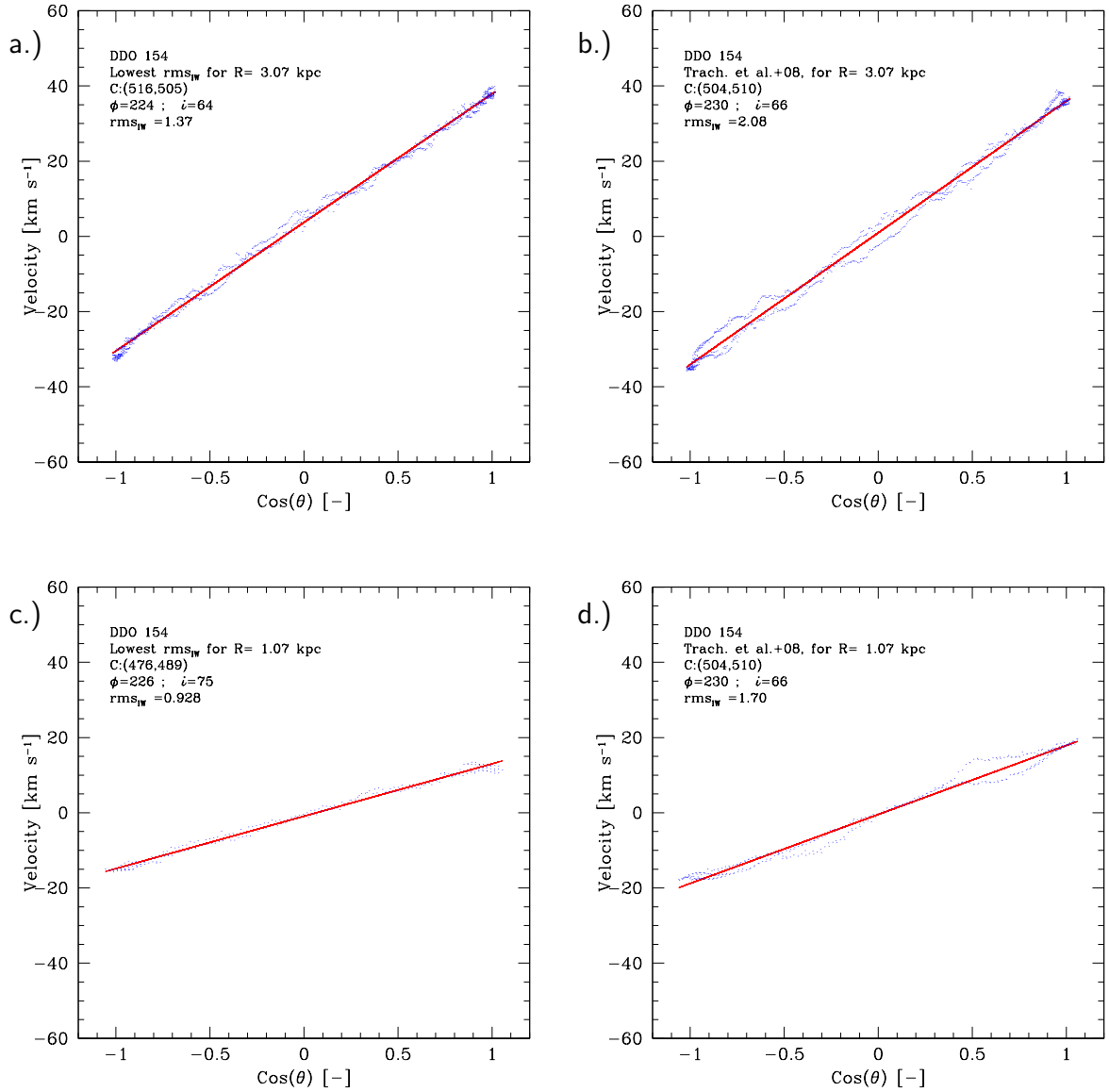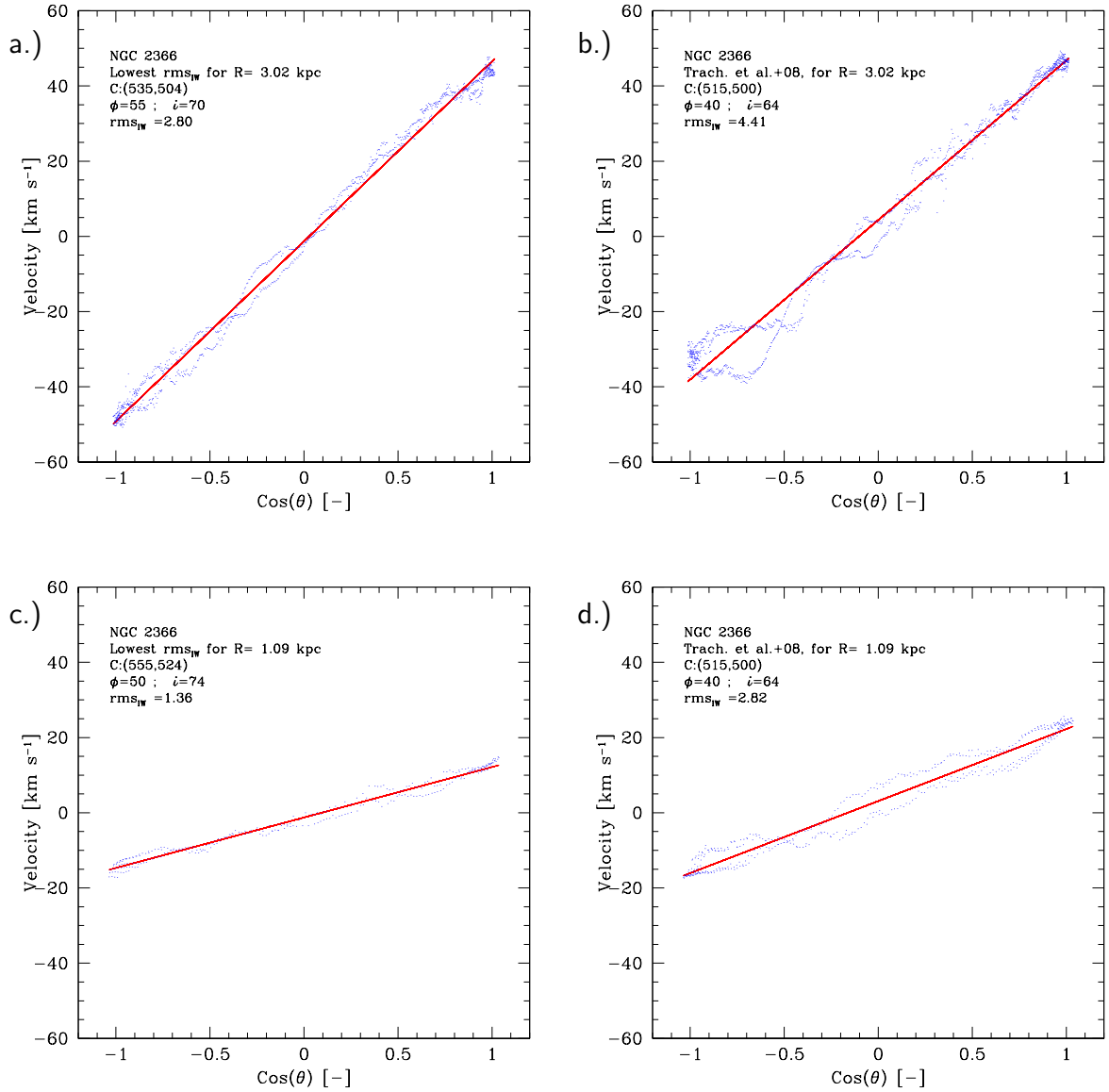
FIGURE 22: DDO 154 – Cos(θ) vs Velocity Plots for 3.07 kpc and 1.07 kpc Annuli Error bars have been left off in order to see the locations of the points as each plot contains several hundred points. a.) This plot shows the parameters corresponding to the lowest RMS$_{IW}$ for the 3.07 kpc annulus. b.) This plot shows the parameters taken from Trachternach et al. (2008) for a 3.07 kpc annulus. c.) This plot shows the parameters corresponding to the lowest RMS$_{IW}$ for the 1.07 kpc annulus. d.) This plot shows the parameters taken from Trachternach et al. (2008) for a 1.07 kpc annulus.
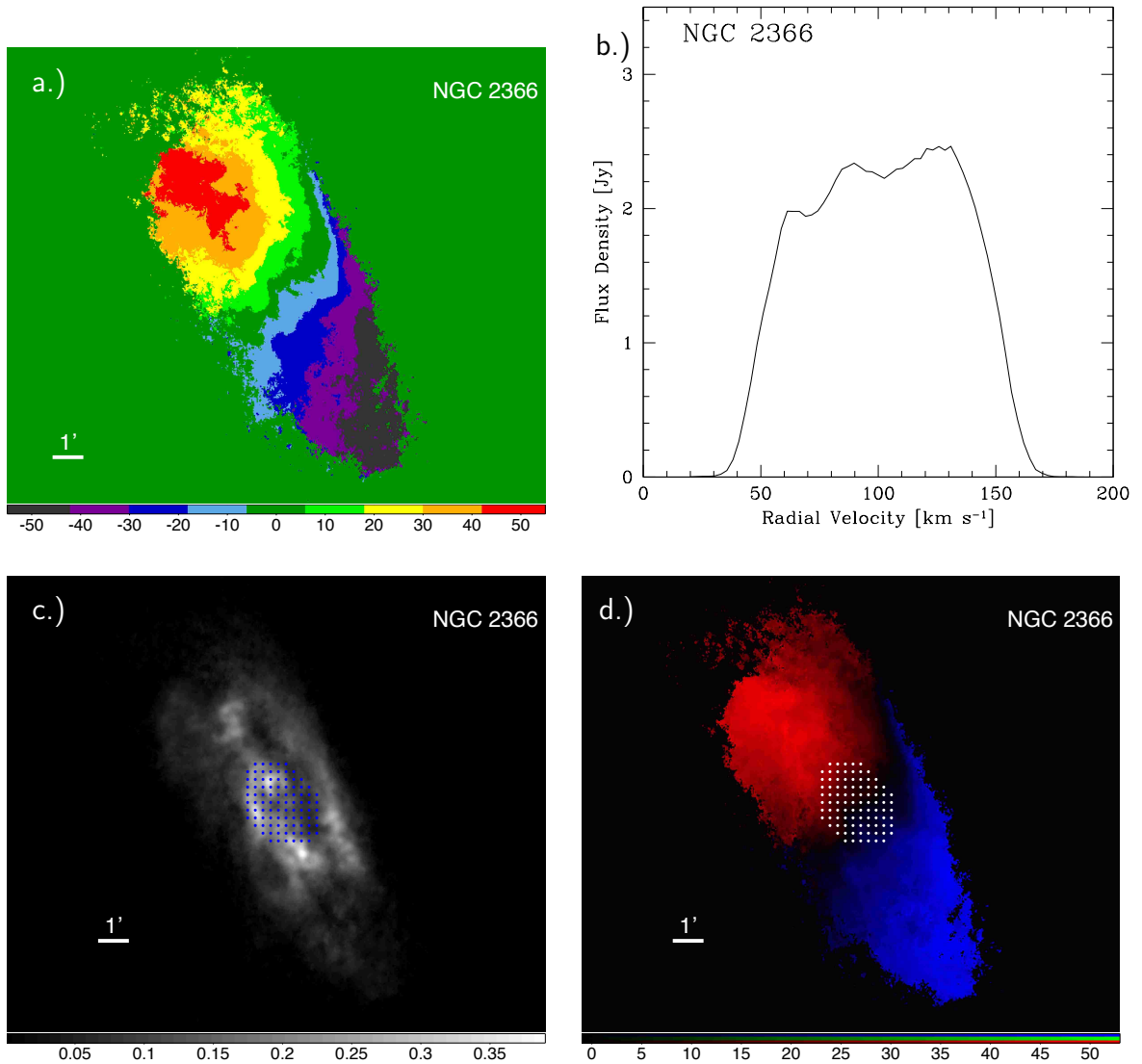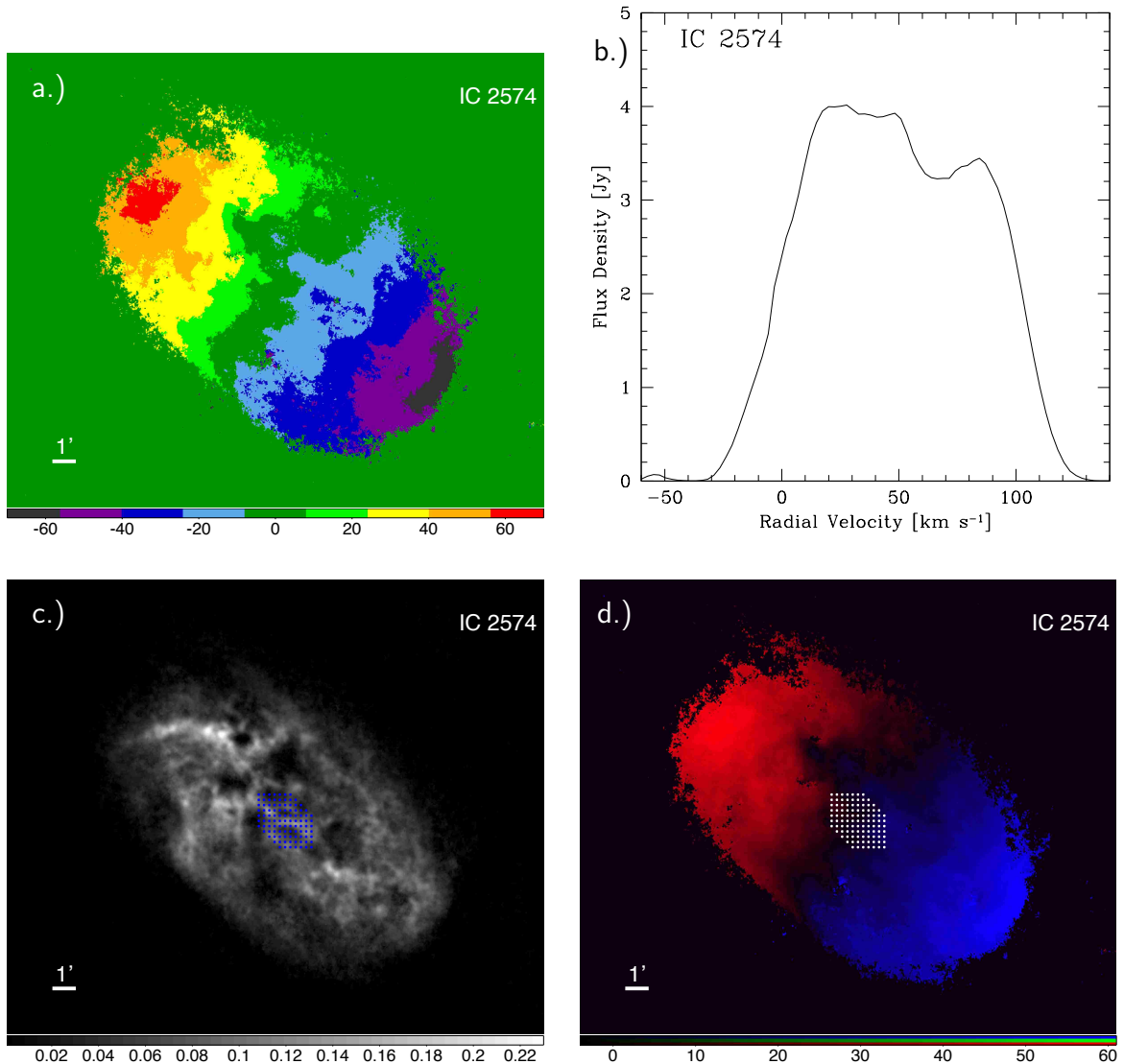
FIGURE 23: NGC 2366 –
a.) This is the velocity field (moment 1) for NGC 2366 derived using the intensity weighted (IW) method. Each color bin is 12 km s^{-1} wide. b.) The Global H I profile for NGC 2366. c.) The center search sample area containing 92 centers overlaid onto the integrated H I map. The parameter space of position and inclination angles is investigated each of these centers. Each center is separated by approximately 0.247 kpc in α and δ. d.) The center search overlaid onto a continuous velocity field; the more vibrant blue and red are the locations of the strongest rotation.
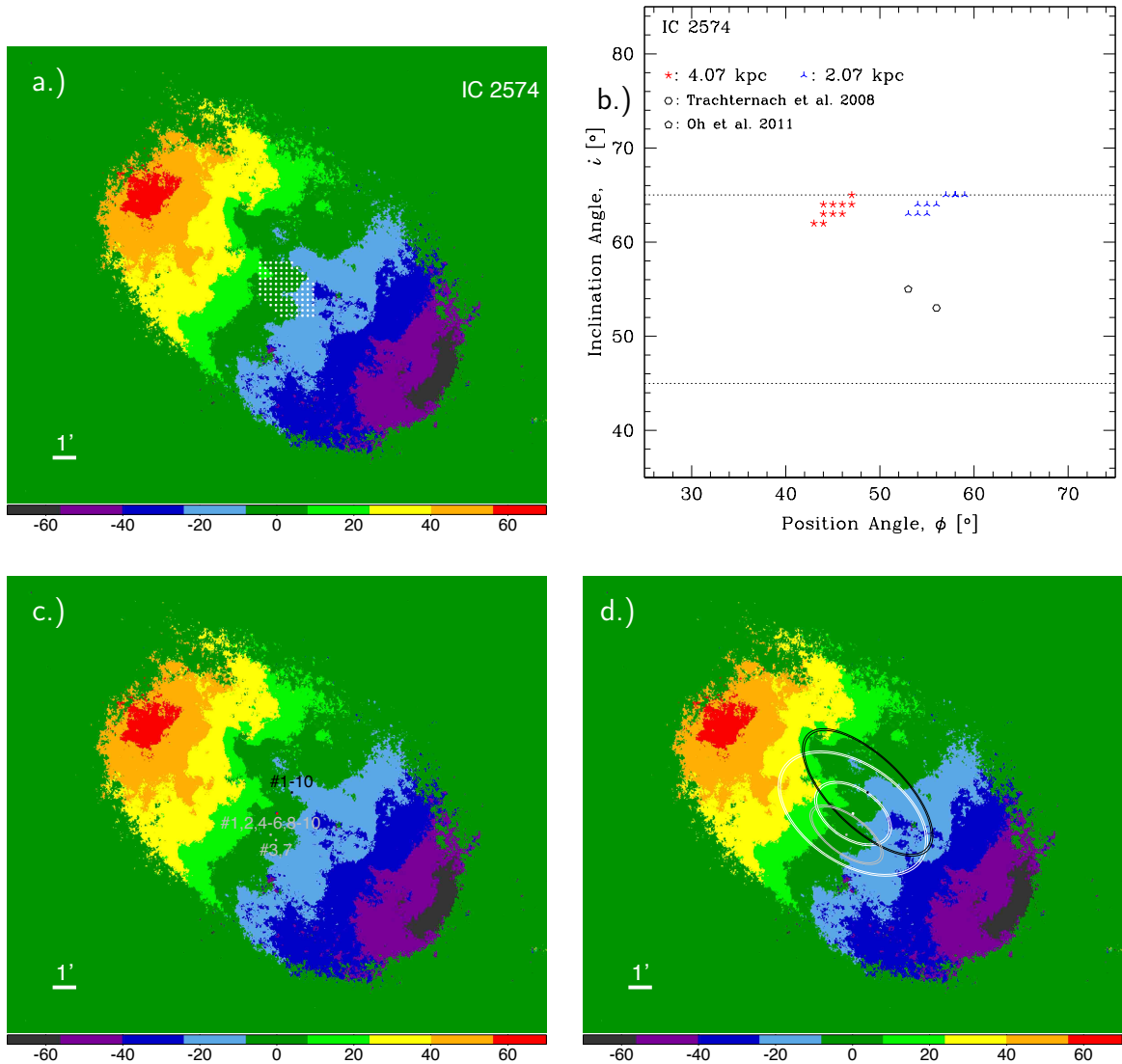
FIGURE 24: NGC 2366 – Results

a.) The center search sample area for NGC 2366 of 92 centers overlaid onto integrated HI map. The parameter space of position and inclination angles is investigated each of these centers. Each center is separated by approximately 0.247 kpc in α and δ. b.) A plot showing the orientation parameters for the ten lowest RMS_{IW} of the IW search for both annuli. The dotted rectangle shows the allowable limits of ϕ and i. c.) An image showing the center locations for the ten lowest RMS_{IW} of the IW search for the 3.02 kpc annulus (black) and the 1.09 kpc annulus (grey) overlaid onto the velocity field. Centers reported by Oh et al. (2008) (blue) and Trachternach et al. (2008) (red) are also included. d.) An image showing the model parameters using the lowest RMS_{IW} for the 3.02 kpc annulus (black), the 1.09 kpc annulus (grey), and for parameters taken from Trachternach et al. (2008) (white for both annuli).
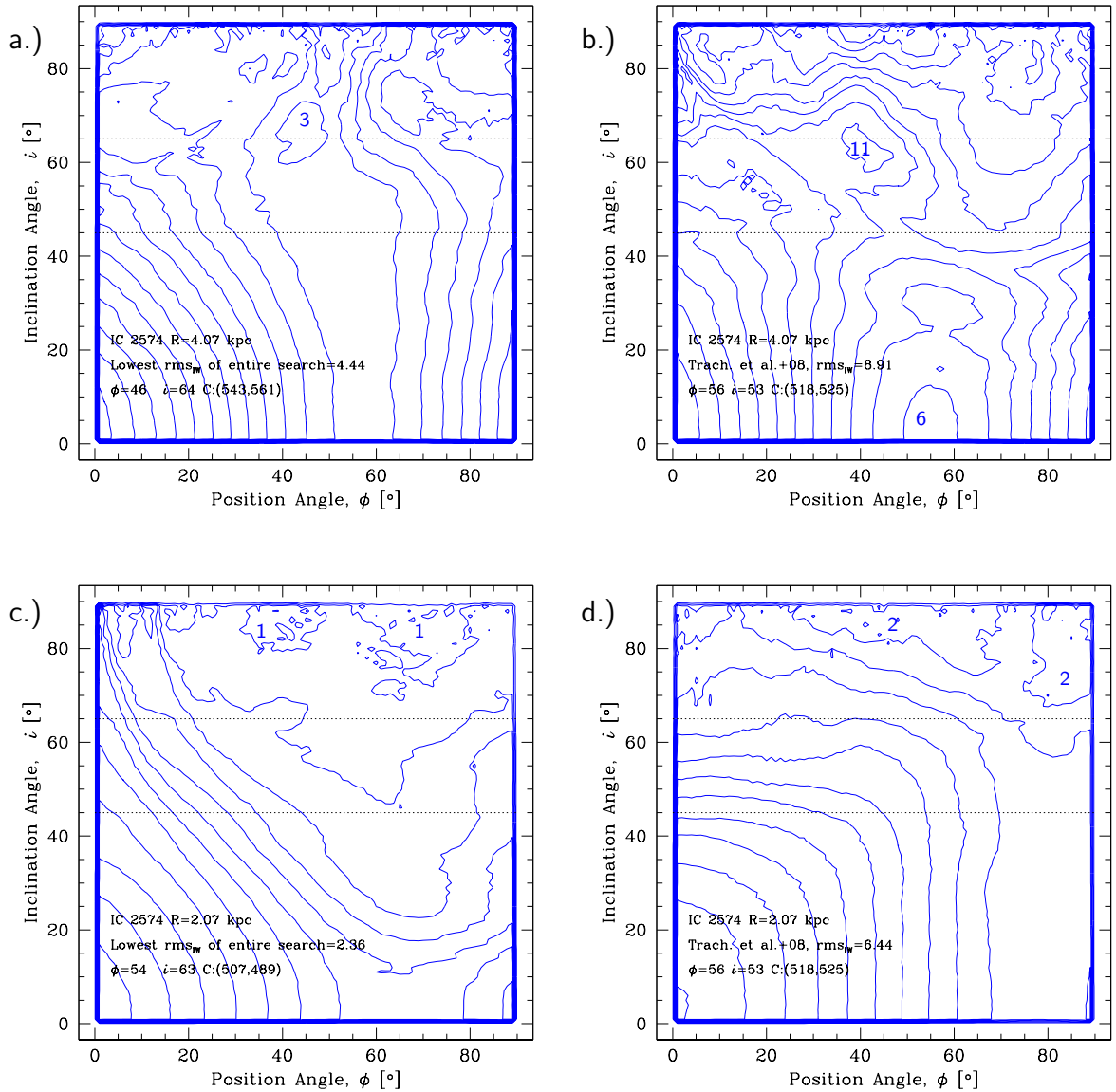
FIGURE 25: NGC 2366 – RMS Contour Plots for 3.02 kpc and 1.09 Annuli
The dotted lines show the allowable limits of i. The lowest contour for each are labeled and increase in increments of 1 km sec^{-1}: a.) for the center which contains the lowest RMS value found using the IW method with the 3.02 kpc annulus. b.) using the center from Trachternach et al. (2008) with the 3.02 kpc annulus. c.) for the center which contains the lowest RMS value found using the IW method with the 1.09 kpc annulus. d.) using the center from Trachternach et al. (2008) with the 1.09 kpc annulus.

FIGURE 26: NGC 2366 – Cos(θ) vs Velocity Plots for 3.02 kpc and 1.09 Annuli
Error bars have been left off in order to see the locations of the points as each plot contains several hundred points. a.) This plot shows the parameters corresponding to the lowest RMS$_{IW}$ for the 3.02 kpc annulus. b.) This plot shows the parameters taken from Trachternach et al. (2008) for a 3.02 kpc annulus. c.) This plot shows the parameters corresponding to the lowest RMS$_{IW}$ for the 1.09 kpc annulus. d.) This plot shows the parameters taken from Trachternach et al. (2008) for a 1.09 kpc annulus.

FIGURE 27: IC 2574 –

a.) This is the velocity field (moment 1) for IC 2574 derived using the intensity weighted (IW) method. Each color bin is 16 km s^{-1} wide. b.) The Global H$\textsc{i}$ profile for IC 2574. c.) The center search sample area containing 101 centers overlaid onto the integrated H$\textsc{i}$ map. The parameter space of position and inclination angles is investigated each of these centers. Each center is separated by approximately 0.262 kpc in α and δ. d.) The center search overlaid onto a continuous velocity field; the more vibrant blue and red are the locations of the strongest rotation.

FIGURE 28: IC 2574 – Results

a.) The center search sample area for IC 2574 of 101 centers overlaid onto integrated HI map. The parameter space of position and inclination angles is investigated each of these centers. Each center is separated by approximately 0.262 kpc in α and δ. b.) A plot showing the orientation parameters for the ten lowest RMS_{IW} of the IW search for both annuli. The dotted rectangle shows the allowable limits of ϕ and i. c.) An image showing the center locations for the ten lowest RMS_{IW} of the IW search for the 4.07 kpc annulus (black) and the 2.07 kpc annulus (grey) overlaid onto the velocity field. Centers reported by Oh et al. (2008) (blue) and Trachternach et al. (2008) (red) are also included, for this galaxy these two points are near the same location. d.) An image showing the model parameters using the lowest RMS_{IW} for the 4.07 kpc annulus (black), the 2.07 annulus (grey), and for parameters taken from Trachternach et al. (2008) (white for both annuli).

113

FIGURE 29: IC 2574 – RMS Contour Plots for 4.07 kpc and 2.07 kpc Annuli
The dotted lines show the allowable limits of i. The lowest contour for each are labeled and increase in increments of 1 km sec^{-1}: a.) for the center which contains the lowest RMS value found using the IW method with the 4.07 kpc annulus. b.) using the center from Trachternach et al. (2008) with the 4.07 kpc annulus. c.) for the center which contains the lowest RMS value found using the IW method with the 2.07 kpc annulus. d.) using the center from Trachternach et al. (2008) with the 2.07 kpc annulus.
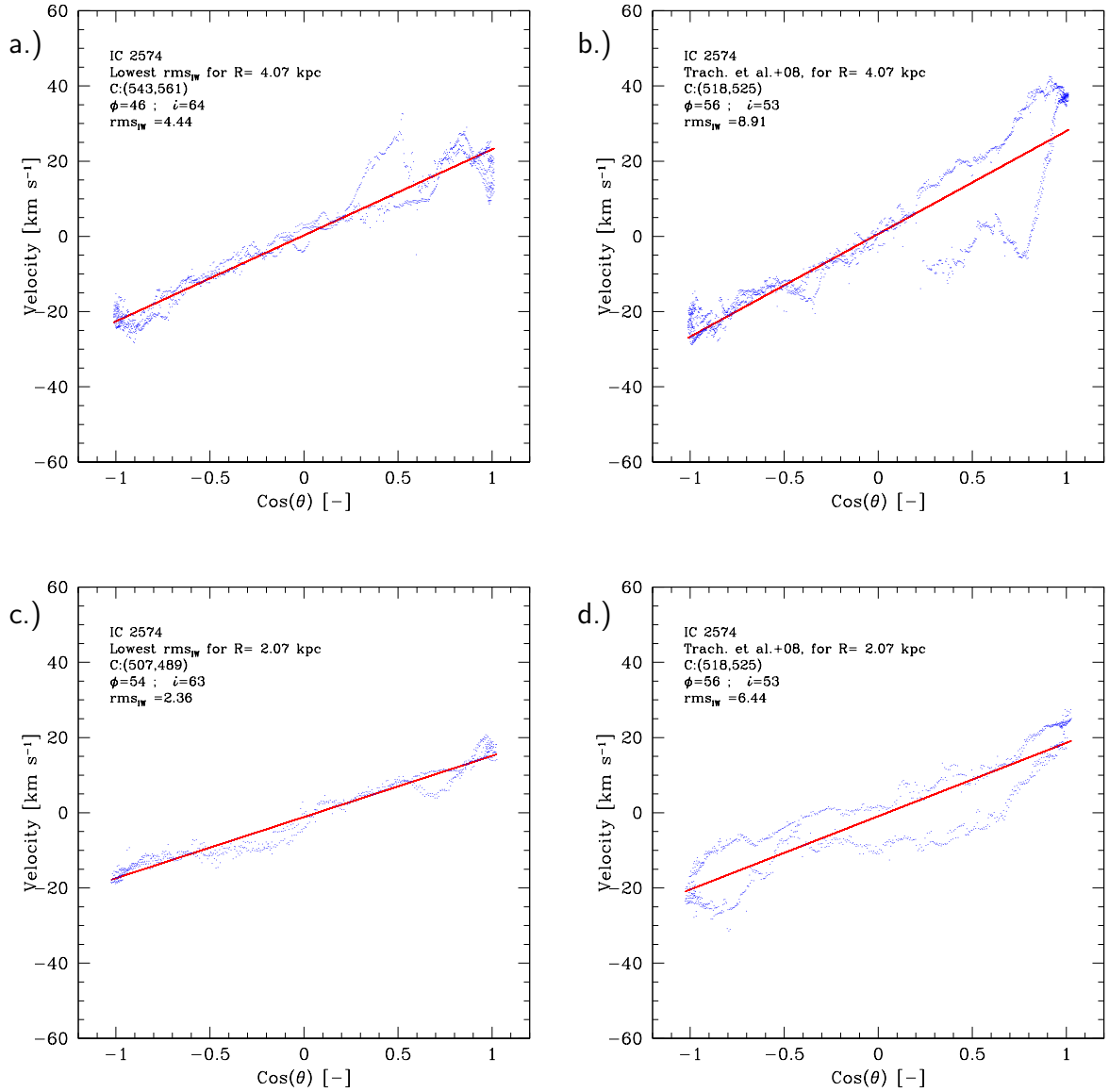
FIGURE 30: IC 2574 – Cos(θ) vs Velocity Plots for 4.07 kpc and 2.07 kpc Annuli
Error bars have been left off in order to see the locations of the points as each plot
contains several hundred points. a.) This plot shows the parameters corresponding
to the lowest RMS$_{IW}$ for the 4.07 kpc annulus. b.) This plot shows the parameters
taken from Trachternach et al. (2008) for a 4.07 kpc annulus. c.) This plot shows
the parameters corresponding to the lowest RMS$_{IW}$ for the 2.07 kpc annulus. d.)
This plot shows the parameters taken from Trachternach et al. (2008) for a 2.07 kpc
annulus.
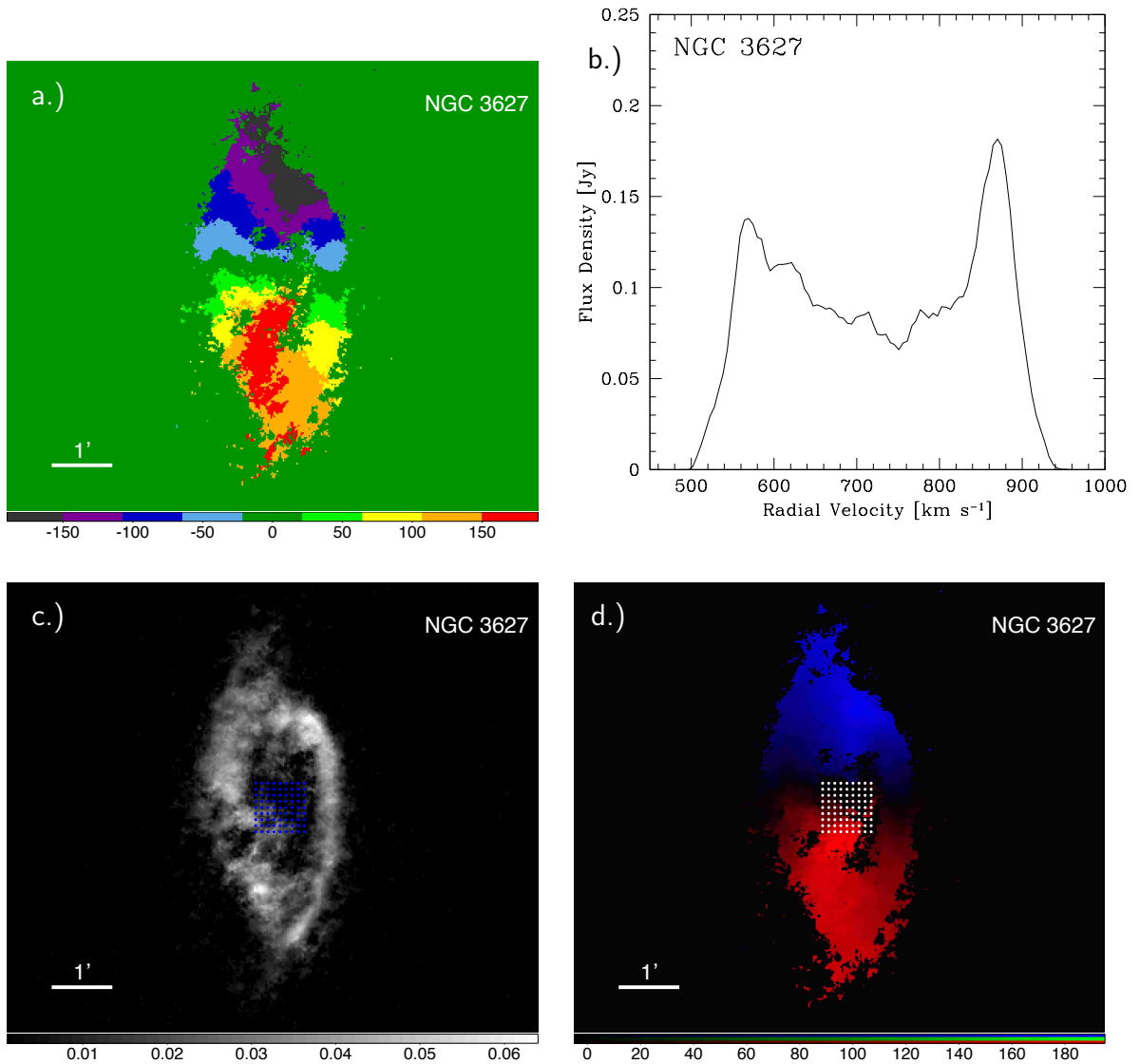
FIGURE 31: NGC 3627 –
a.) This is the velocity field (moment 1) for NGC 3627 derived using the intensity weighted (IW) method. Each color bin is about 43 km s^{-1} wide. b.) The Global H I profile for NGC 3627. c.) The center search sample area containing 81 centers overlaid onto the integrated H I map. The parameter space of position and inclination angles is investigated each of these centers. Each center is separated by approximately 0.271 kpc in α and δ. d.) The center search overlaid onto a continuous velocity field; the more vibrant blue and red are the locations of the strongest rotation.
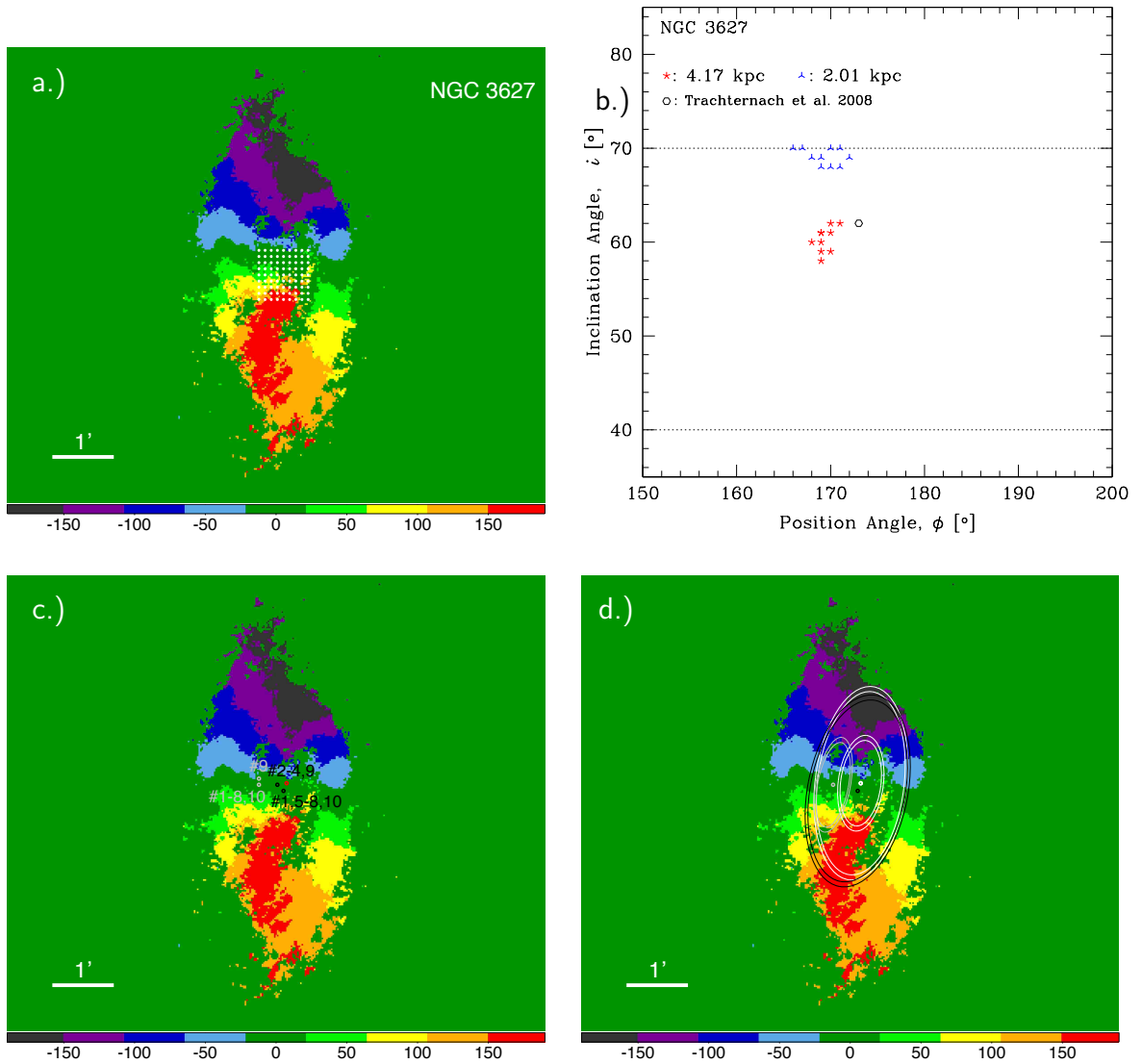
FIGURE 32: NGC 3627 – Results

a.) The center search sample area for NGC 3627 of 81 centers overlaid onto integrated H I map. The parameter space of position and inclination angles is investigated each of these centers. Each center is separated by approximately 0.271 kpc in α and δ.
b.) A plot showing the orientation parameters for the ten lowest RMS_{IW} of the IW search for both annuli. The dotted rectangle shows the allowable limits of ϕ and i.
c.) An image showing the center locations for the ten lowest RMS_{IW} of the IW search for the 4.17 kpc annulus (black) and the 2.01 kpc annulus (grey) overlaid onto the velocity field. Centers reported by Trachternach et al. (2008) (red) is also included.
d.) An image showing the model parameters using the lowest RMS_{IW} for the 4.17 kpc annulus (black), the 2.01 kpc annulus (grey), and for parameters taken from Trachternach et al. (2008) (white for both annuli).
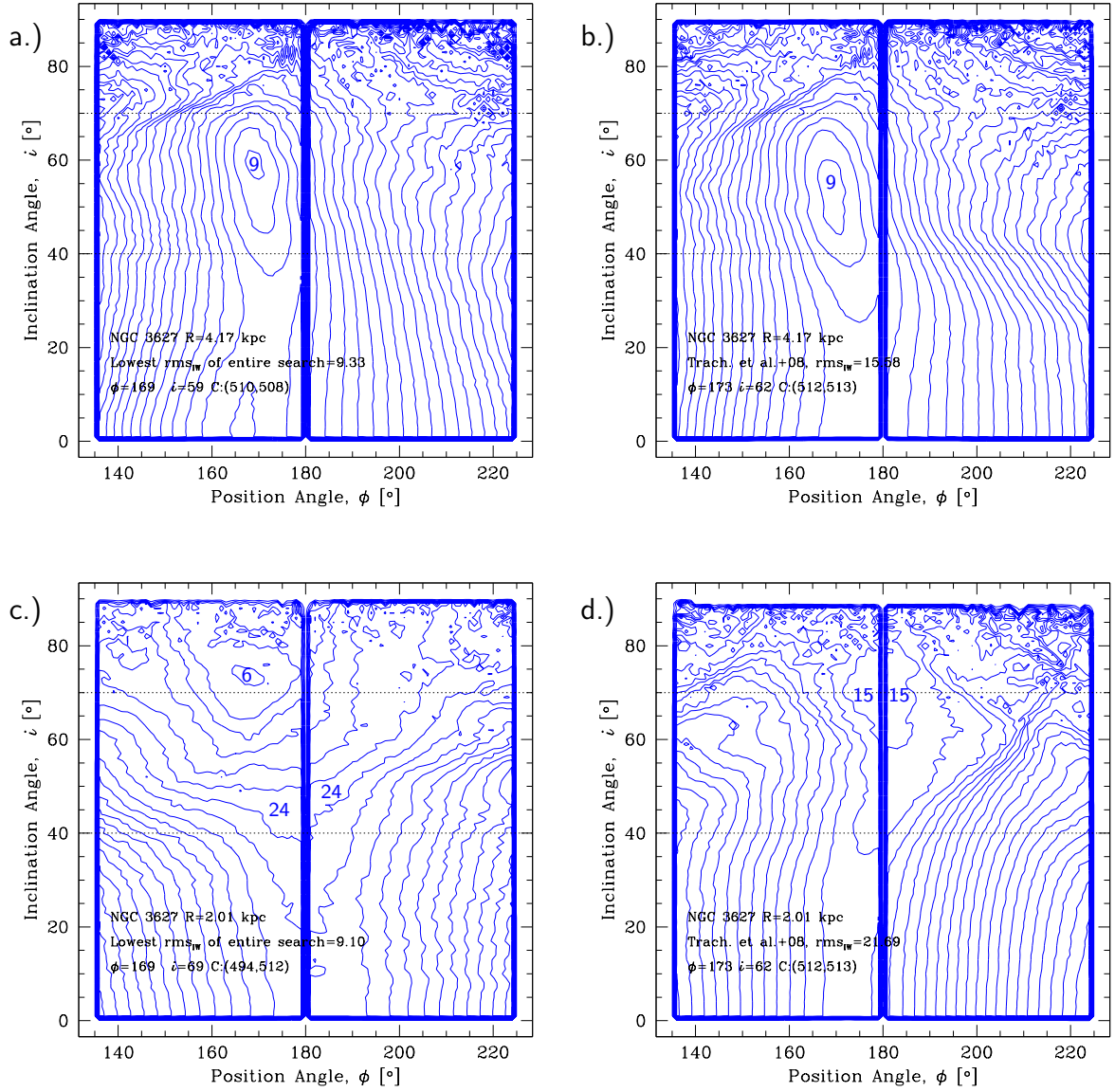
FIGURE 33: NGC 3627 – RMS Contour Plots for 4.17 kpc and 2.01 kpc Annuli
The dotted lines show the allowable limits of i. The lowest contour for each are labeled and increase in increments of 3 km sec^{-1}: a.) for the center which contains the lowest RMS value found using the IW method with the 4.17 kpc annulus. b.) using the center from Trachternach et al. (2008) with the 4.17 kpc annulus. c.) for the center which contains the lowest RMS value found using the IW method with the 2.01 kpc annulus. d.) using the center from Trachternach et al. (2008) with the 2.01 kpc annulus.
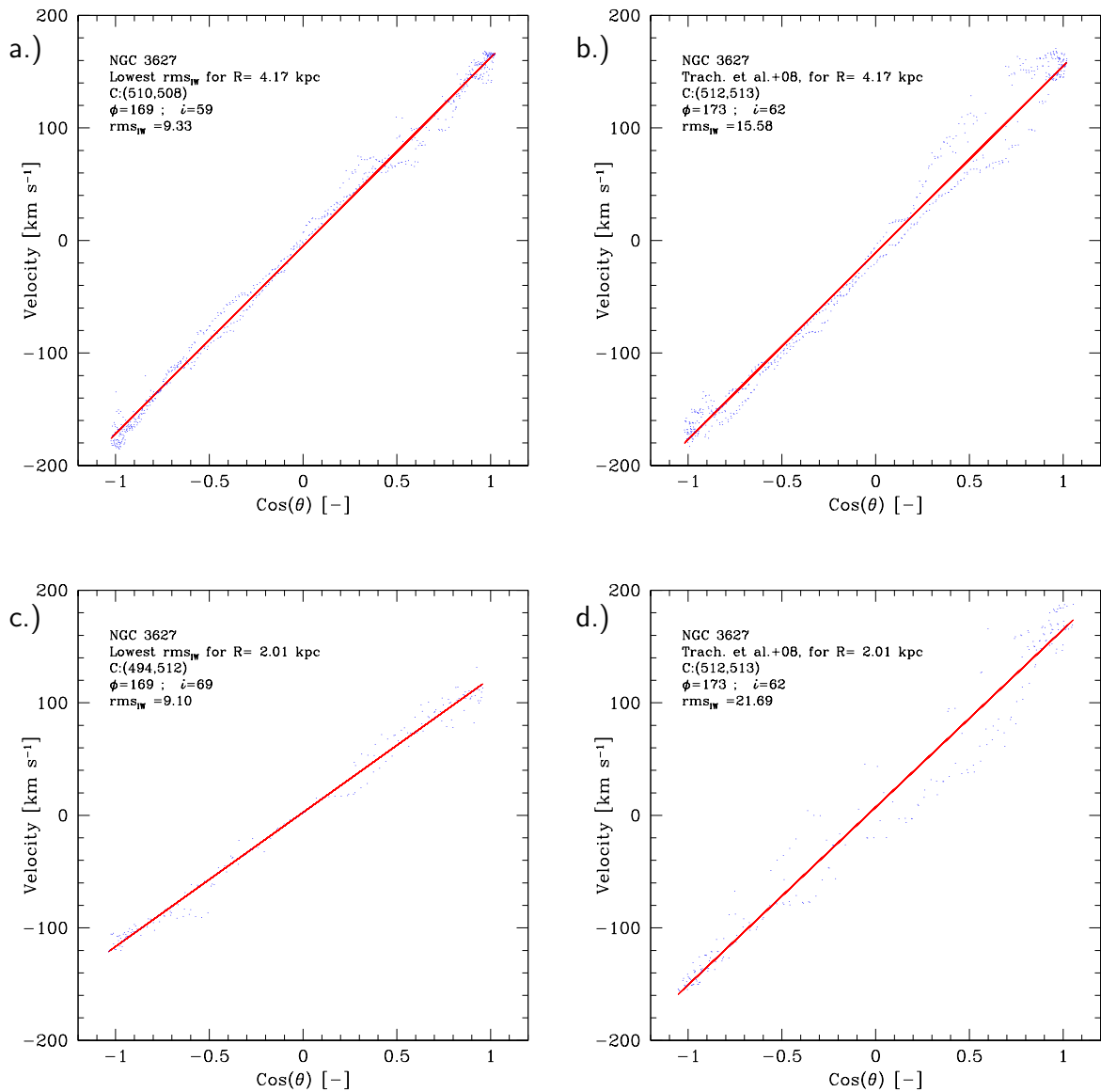
FIGURE 34: NGC 3627 – Cos(θ) vs Velocity Plots for 4.17 kpc and 2.01 kpc Annuli Error bars have been left off in order to see the locations of the points as each plot contains several hundred points. a.) This plot shows the parameters corresponding to the lowest RMS$_{IW}$ for the 4.17 kpc annulus. b.) This plot shows the parameters taken from Trachternach et al. (2008) for a 4.17 kpc annulus. c.) This plot shows the parameters corresponding to the lowest RMS$_{IW}$ for the 2.01 kpc annulus. d.) This plot shows the parameters taken from Trachternach et al. (2008) for a 2.01 kpc annulus.
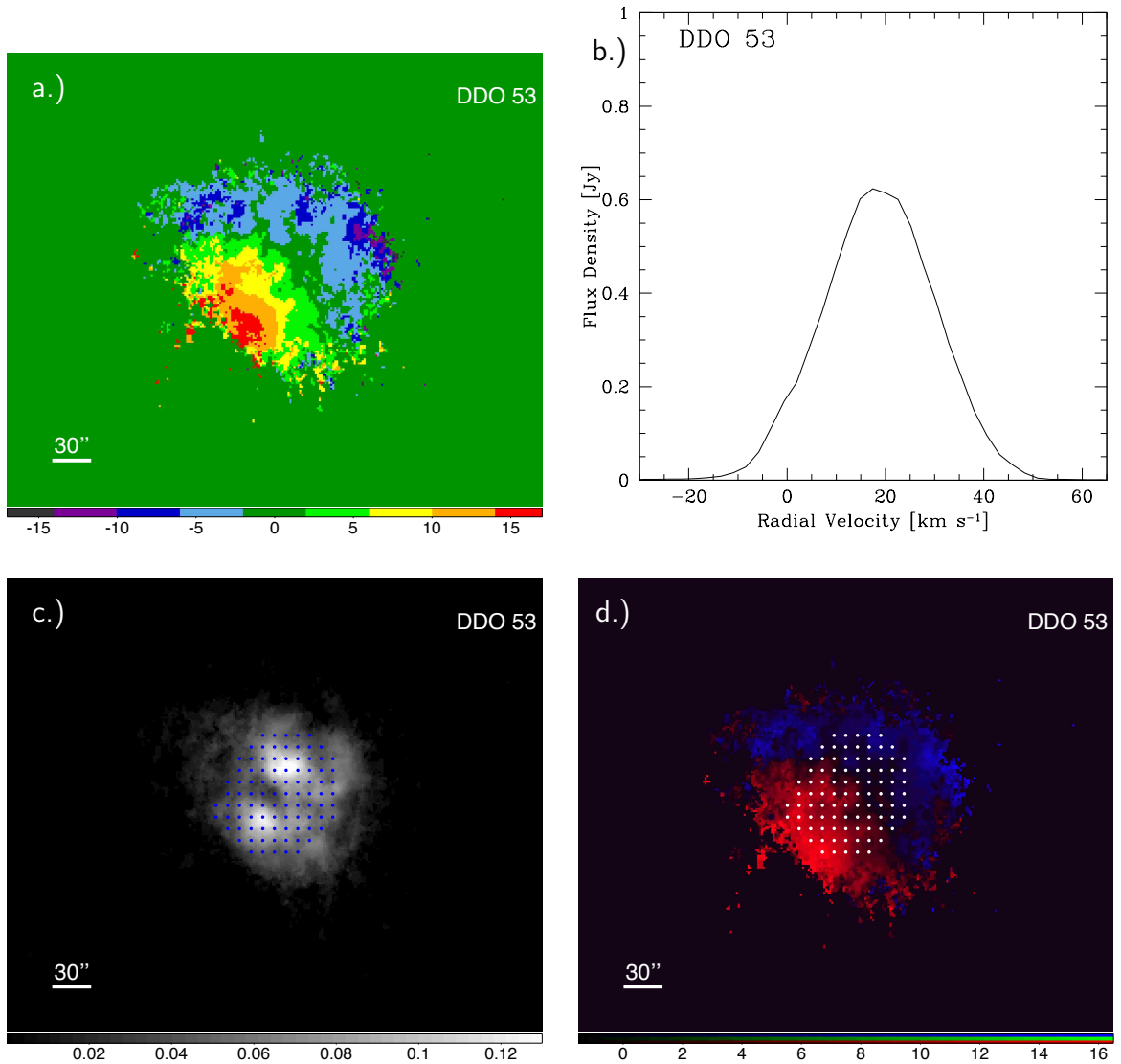
FIGURE 35: DDO 53 –

a.) This is the velocity field (moment 1) for DDO 53 derived using the intensity weighted (IW) method. Each color bin is 4 km s^{-1} wide. b.) The Global H I profile for DDO 53. c.) The center search sample area containing 93 centers overlaid onto the integrated H I map. The parameter space of position and inclination angles is investigated each of these centers. Each center is separated by approximately 0.157 kpc in α and δ. d.) The center search overlaid onto a continuous velocity field; the more vibrant blue and red are the locations of the strongest rotation.
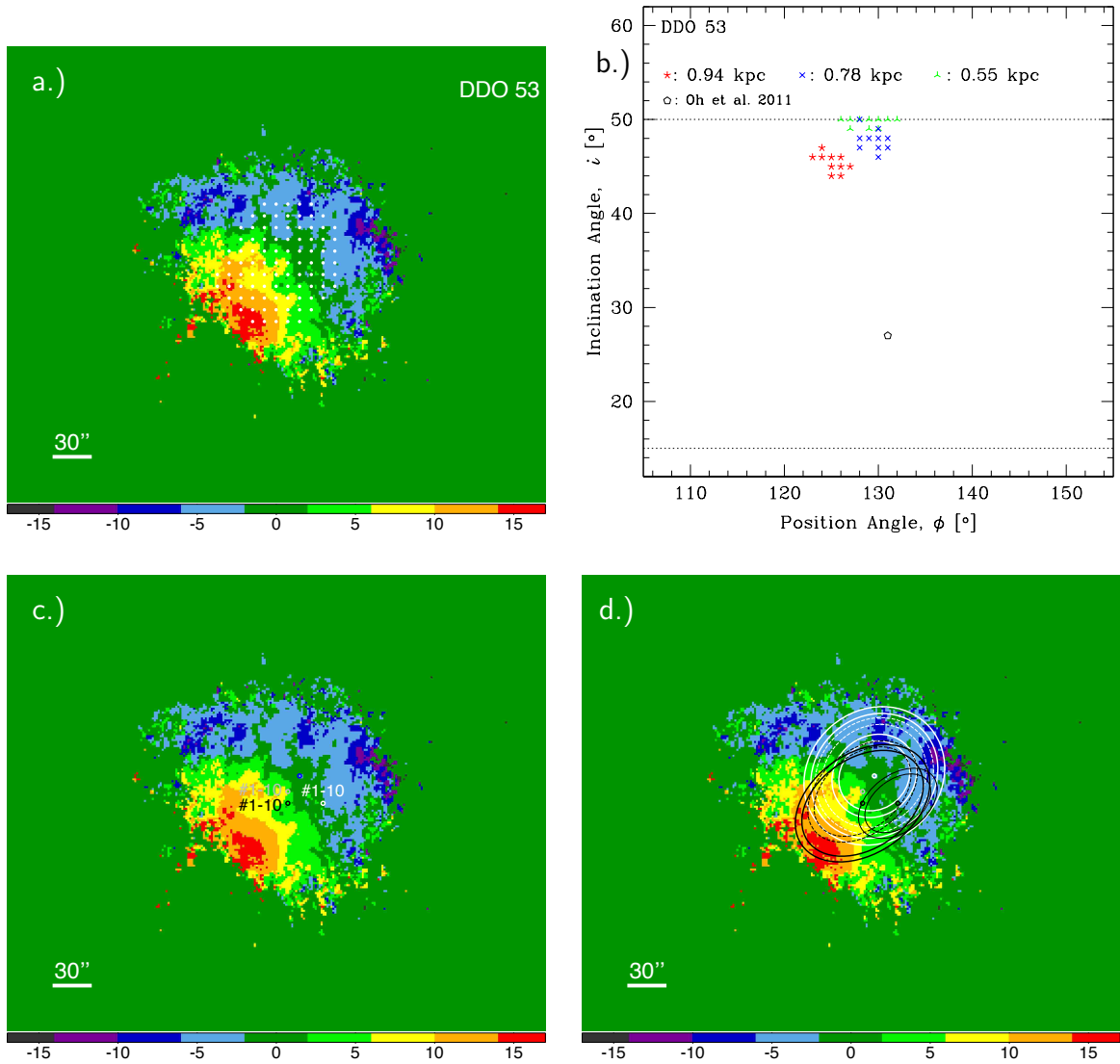
FIGURE 36: DDO 53 – Results

a.) The center search sample area for DDO 53 of 93 centers overlaid onto integrated H I map. The parameter space of position and inclination angles is investigated each of these centers. Each center is separated by approximately 0.157 kpc in α and δ. b.) A plot showing the orientation parameters for the ten lowest RMS_{IW} of the IW search for both annuli. The dotted rectangle shows the allowable limits of ϕ and i. c.) An image showing the center locations for the ten lowest RMS_{IW} of the IW search for the 0.94 kpc annulus (black), the 0.78 kpc annulus (grey), and the 0.55 kpc annulus (white) overlaid onto the velocity field. Center reported by Oh et al. (2008) (blue) is also included. d.) An image showing the model parameters using the lowest RMS_{IW} for the 0.94 kpc annulus (black), the 0.78 kpc annulus (grey), the 0.55 kpc annulus (black), and for parameters taken from Oh et al. (2008) (white for all annuli, 0.78 kpc annulus is dashed).
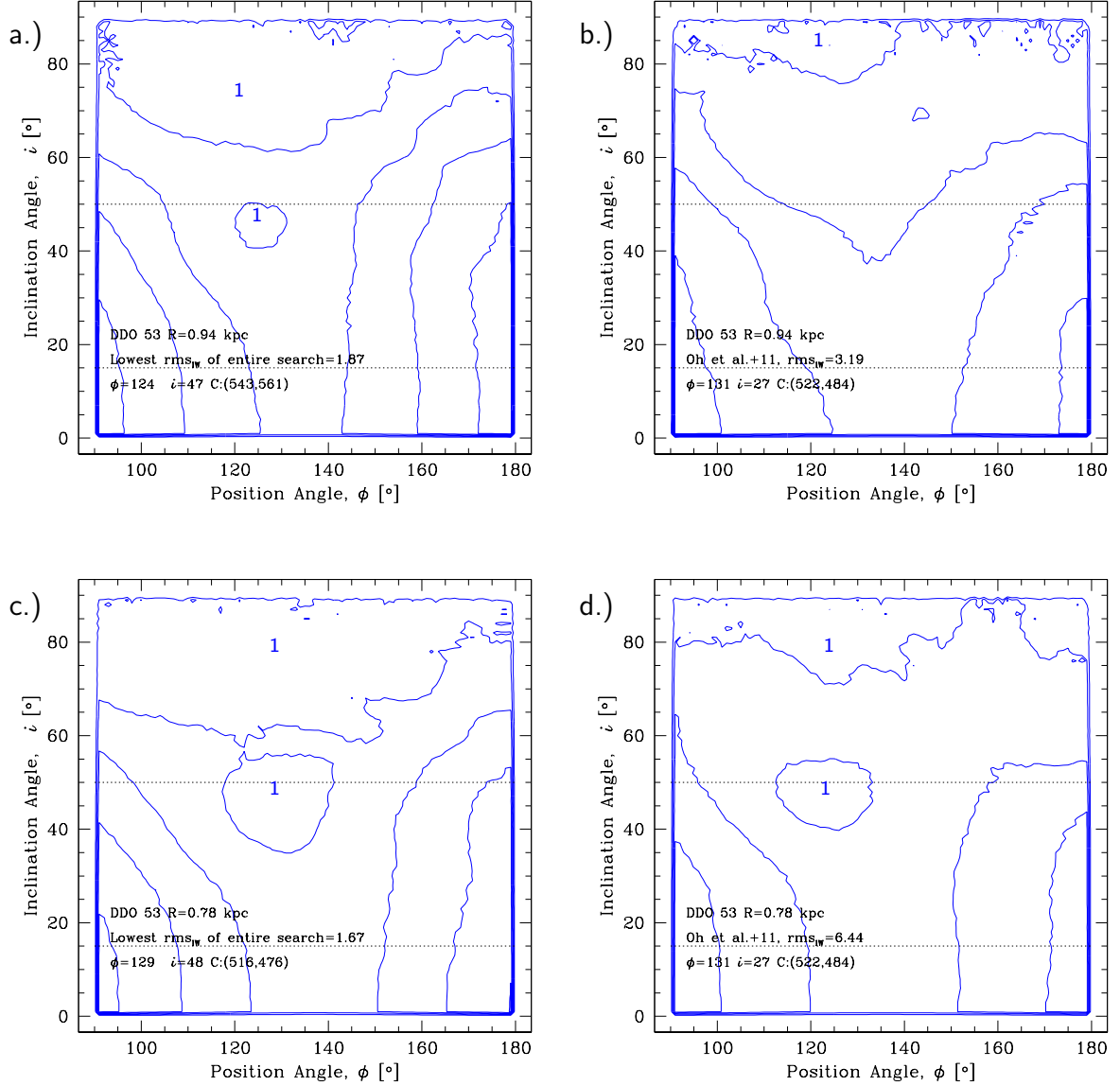
FIGURE 37: DDO 53 – RMS Contour Plots for 0.94 kpc and 0.78 kpc Annuli
The dotted lines show the allowable limits of i. The lowest contour for each are labeled and increase in increments of 1 km sec^{-1}: a.) for the center which contains the lowest RMS value found using the IW method with the 0.94 kpc annulus. b.) using the cent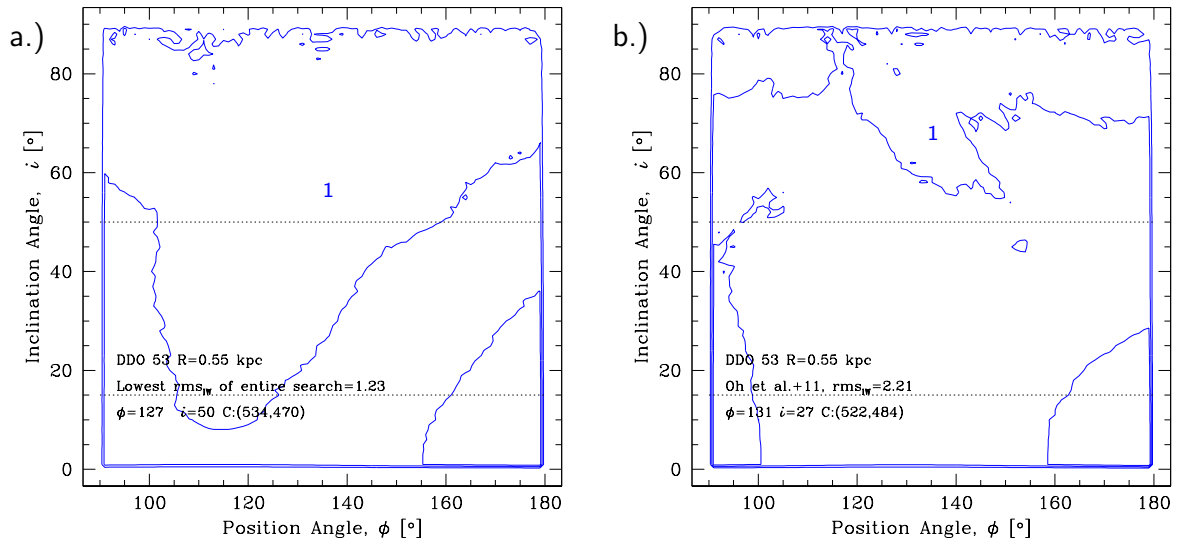er from Oh et al. (2008) with the 0.94 kpc annulus. c.) for the center which contains the lowest RMS value found using the IW method with the 0.78 kpc annulus. d.) using the center from Oh et al. (2008) with the 0.78 kpc annulus.

FIGURE 38: DDO 53 – RMS and (a-V_{sys}) Contour Plots for 0.55 kpc Annulus
The dotted lines show the allowable limits of i. The lowest contour for each are labeled and increase in increments of 1 km sec^{-1}: a.) for the center which contains the lowest RMS value found using the IW method. b.) using the center from Oh et al. (2008).
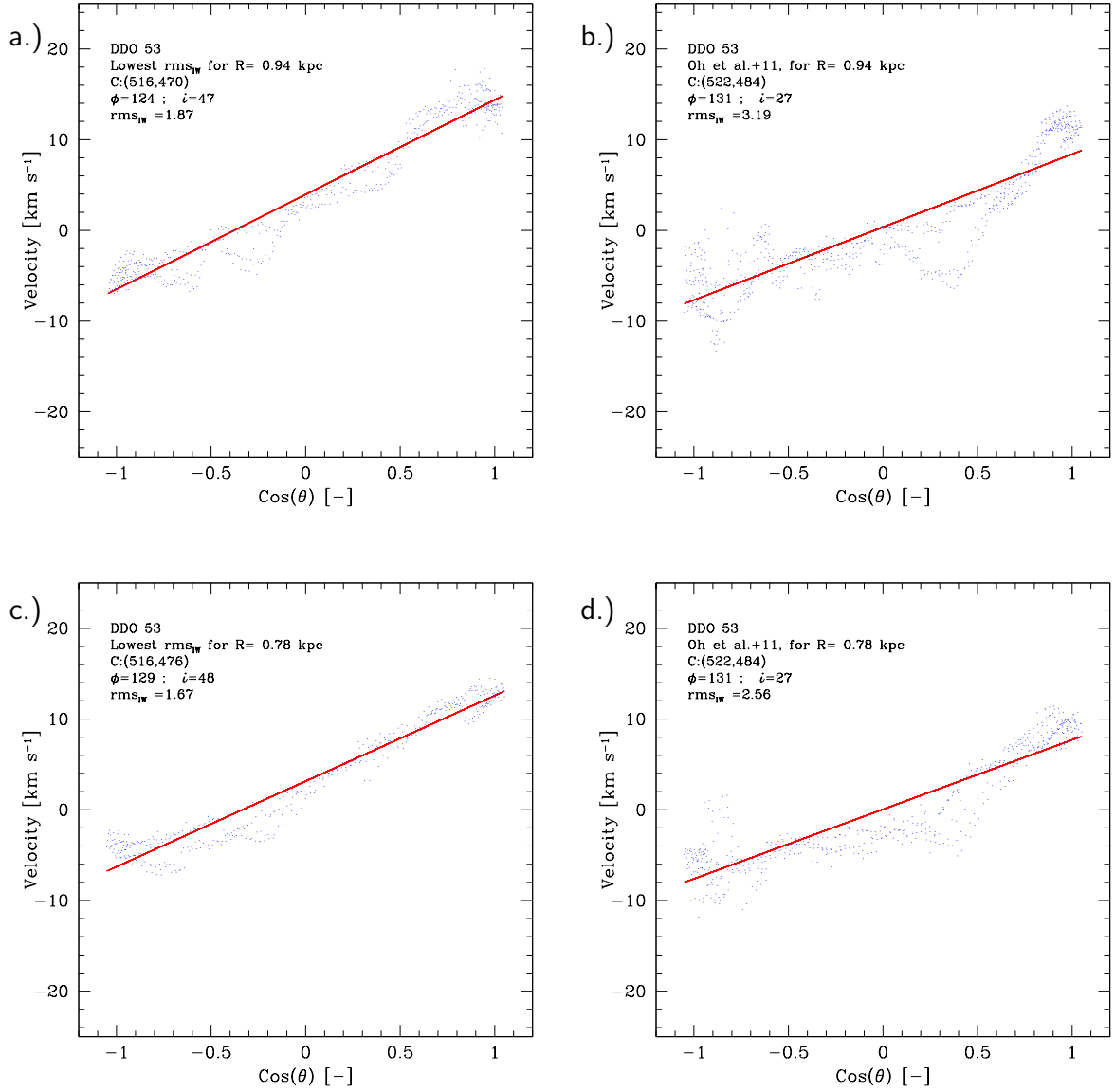
FIGURE 39: DDO 53 – Cos(θ) vs Velocity Plots for 0.94 kpc and 0.78 kpc Annuli Error bars have been left off in order to see the locations of the points as each plot contains several hundred points. a.) This plot shows the parameters corresponding to the lowest RMS$_{IW}$ for the 0.94 kpc annulus. b.) This plot shows the parameter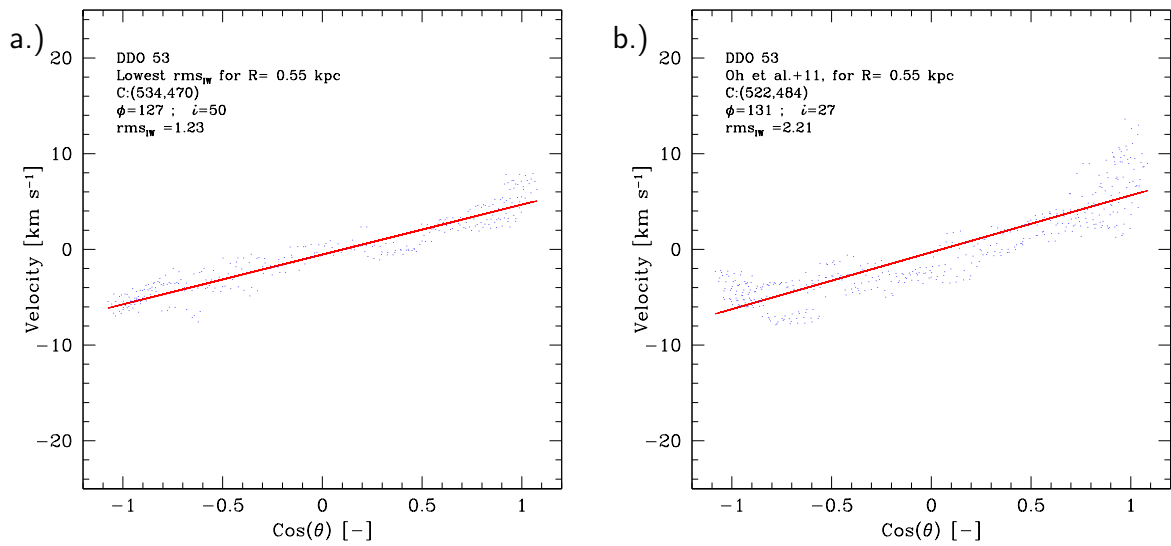s taken from Oh et al. (2008) for a 0.94 kpc annulus. c.) This plot shows the parameters corresponding to the lowest RMS$_{IW}$ for the 0.78 kpc annulus. d.) This plot shows the parameters taken from Oh et al. (2008) for a 0.78 kpc annulus.

FIGURE 40: DDO 53 – Cos(θ) vs Velocity Plots for 0.55 kpc Annulus
Error bars have been left off in order to see the locations of the points as each plot contains several hundred points. a.) This plot shows the parameters corresponding to the lowest RMS$_{IW}$ for the 0.55 kpc annulus. b.) This plot shows the parameters taken from Oh et al. (2008) for a 0.55 kpc annulus.
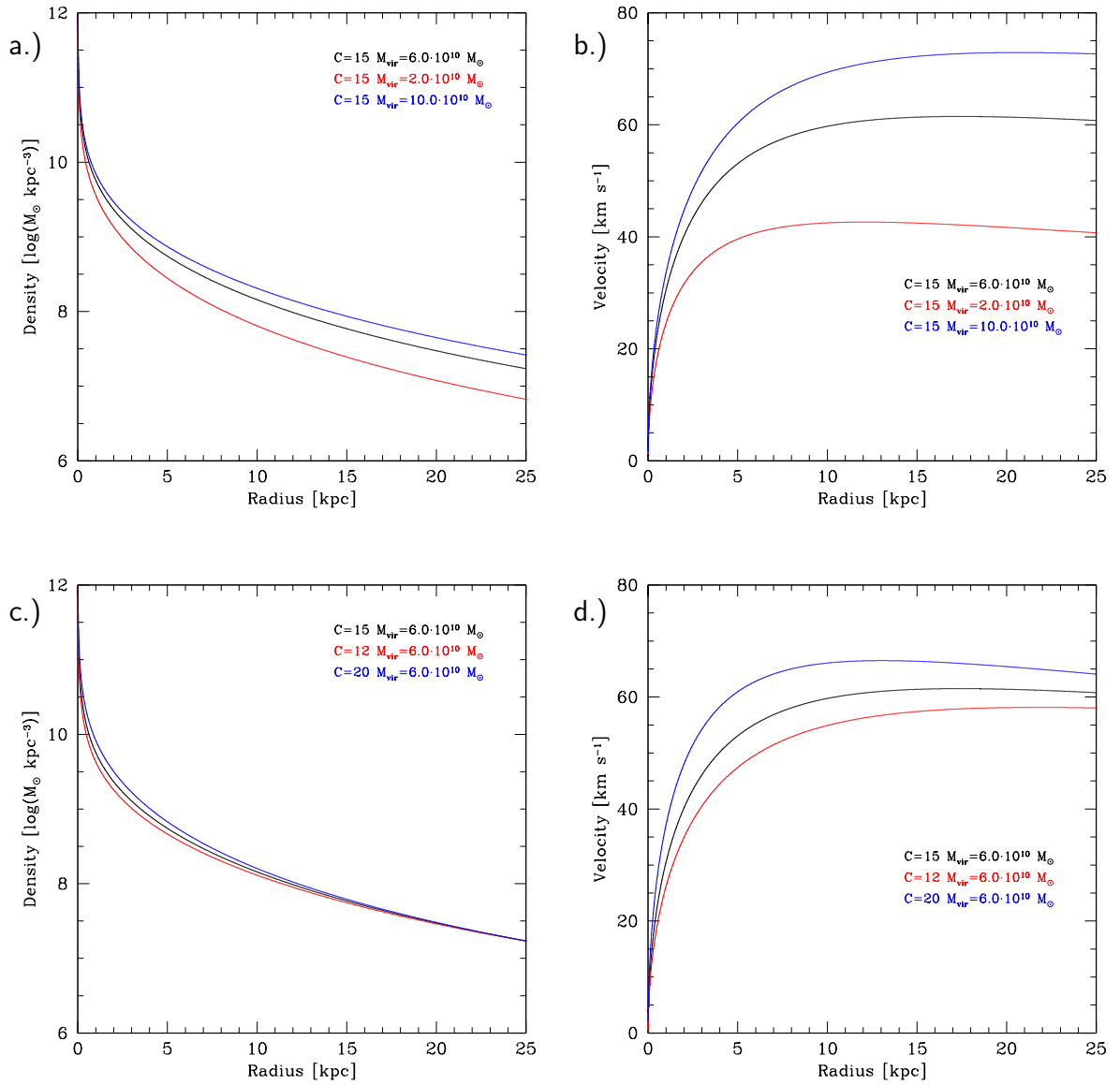
FIGURE 41: NFW Model – Effect on the Density Profile and Rotation Curve Varying M_{vir} and C

a.) Here the concentration parameter is held constant and the effect on changing the virial mass is shown. b.) This plot shows the rotation curves generated by the density profiles in panel a. c.) Here the virial mass is held constant and the effect of changing the concentration is shown. d.) This plot shows the rotation curves generated by the density profiles in panel c.
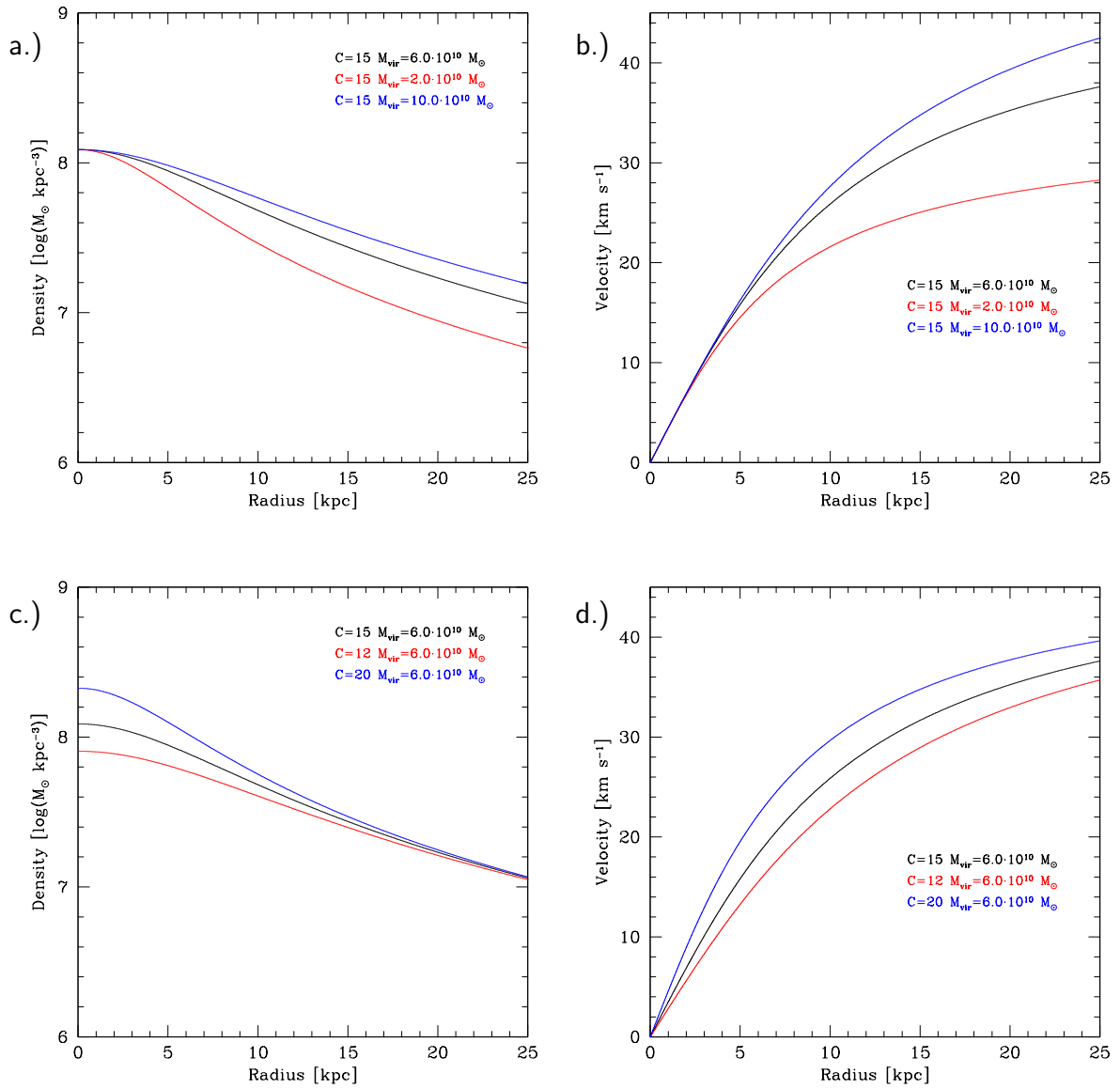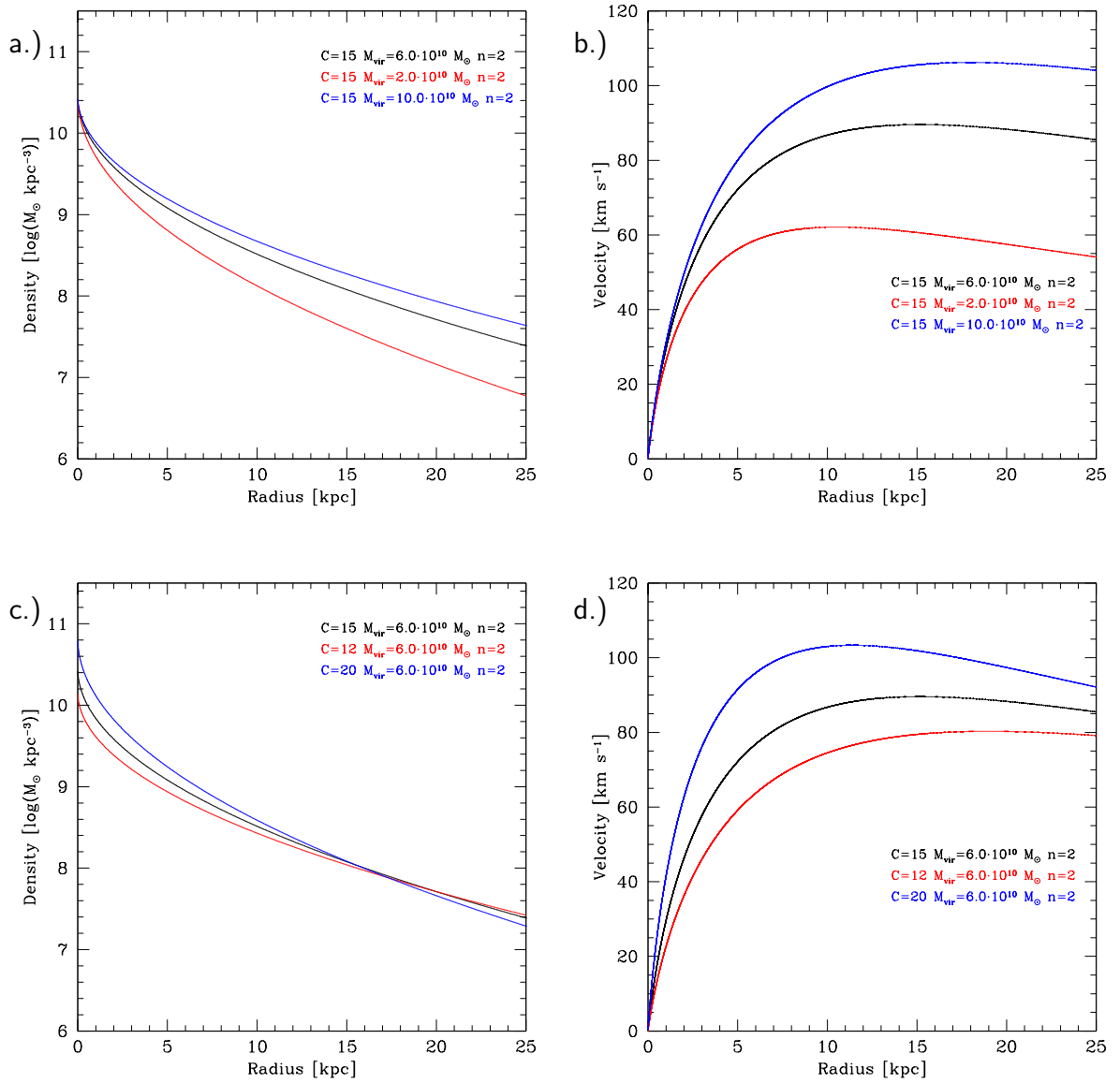
FIGURE 42: ISO Model – Effect on the Density Profile and Rotation Curve Varying M_{vir} and C

a.) Here the concentration parameter is held constant and the effect on changing the virial mass is shown. b.) This plot shows the rotation curves generated by the density profiles in panel a. c.) Here the virial mass is held constant and the effect of changing the concentration is shown. d.) This plot shows the rotation curves generated by the density profiles in panel c.

FIGURE 43: Einasto Model – Effect on the Density Profile and Rotation Curve Varying M_{vir} and C with a Fixed n

a.) Here the concentration parameter is held constant and the effect of changing the virial mass is shown. b.) This plot shows the rotation curves generated by the density profiles in panel a. c.) Here the virial mass is held constant and the effect on changing the concentration is shown. d.) This plot shows the rotation curves generated by the density profiles in panel c.
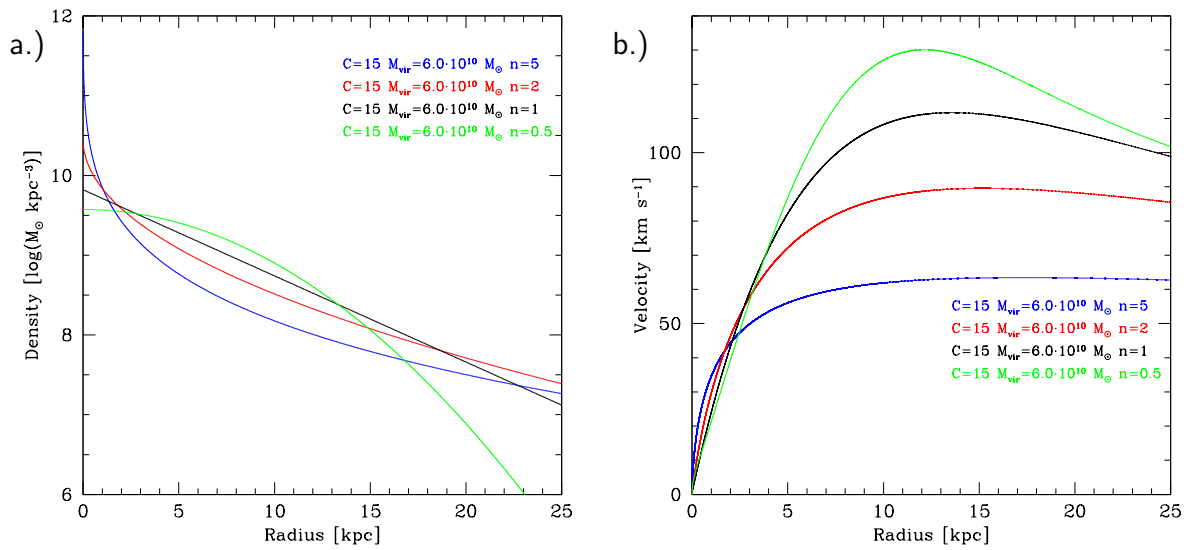
FIGURE 44: Einasto Model – Effect on the Density Profile and Rotation Curve Varying n with a Fixed M_{vir} and C

a.) This plot shows the density profiles for various n. b.) This plot shows the rotation curves generated by the density profiles in panel a.
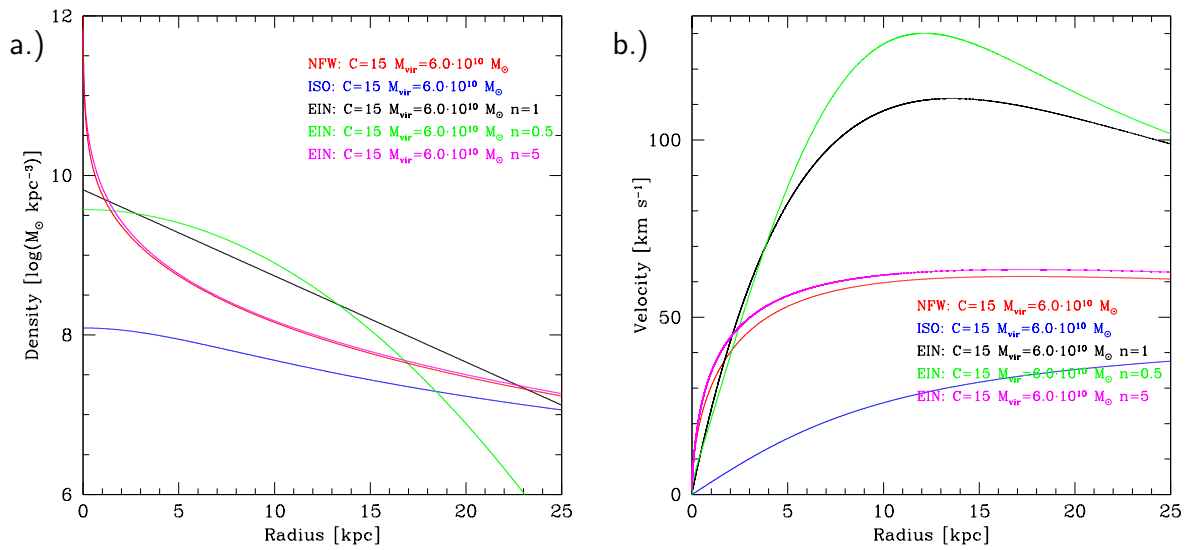
FIGURE 45: Comparison of Halo Models with Fixed M_{vir} and C –
Here three different Einasto indicies are included. a.) This plot shows the density profiles for various models. b.) This plot shows the rotation curves generated by the density profiles in panel a.

REFERENCES

Alcock, C., Allsman, R. A., Alves, D. R., et al. 2000, The Astrophysical Journal, 542, 281

Begeman, K. G. 1989, Astronomy & Astrophysics, 223, 47

Briggs, D. S. 1995, Bulletin of the American Astronomical Society, 27, #112.02

Chemin, L., de Blok, W. J. G., & Mamon, G. A. 2011, The Astronomical Journal, 142, 109

Corbelli, E., Lorenzoni, S., Walterbos, R., Braun, R., & Thilker, D. 2010, Astronomy & Astrophysics, 511, A89

de Blok, W. J. G., Walter, F., Brinks, E., et al. 2008, Astronomical Journal, 136, 2648

Draine, B. T. 2011, Physics of the Interstellar and Intergalactic Medium by Bruce T. Draine. Princeton University Press, 2011.

Duffy, A. R., Meyer, M. J., Staveley-Smith, L., et al. 2012, Mnras, 426, 3385

Einasto, J. 1965, Trudy Astrofizicheskogo Instituta Alma-Ata, 5, 87

Einasto, J. 1969, Astronomische Nachrichten, 291, 97

Essen, L., Donaldson, R. W., Bangham, M. J., & Hope, E. G. 1971, Nature, 229, 110

Ewen, H. I., & Purcell, E. M. 1951, Nature, 168, 356

Field, G. B. 1957, Astronomical Journal, 62, 15

Fisher, J. R., & Tully, R. B. 1981, Astrophysical Journal Supplement, 47, 139

Gentile, G., Salucci, P., Klein, U., Vergani, D., & Kalberla, P. 2004, Mnras, 351, 903

Gould, R. J. 1994, The Astrophysical Journal, 423, 522

Governato, F., Brook, C., Mayer, L., et al. 2010, Nature, 463, 203

Guedes, J., Callegari, S., Madau, P., & Mayer, L. 2011, The Astrophysical Journal, 742, 76

Jansky, K. G. 1933, Nature, 132, 66

Kamphuis, J. J. 1993, Ph.D. Thesis, Univ. Groningen

Klypin, A., Zhao, H., & Somerville, R. S. 2002, The Astrophysical Journal, 573, 597

Kravtsov, A. V., Klypin, A. A., & Khokhlov, A. M. 1997, Astrophysical Journal Supplement, 111, 73

Kravtsov, A. V. 1999, Ph.D. Thesis

Kuhlen, M., Guedes, J., Pillepich, A., Madau, P., & Mayer, L. 2013, The Astrophysical Journal, 765, 10

Lake, G., & Mark, J. W.-K. 1980, Nature, 287, 705

Milgrom, M. 1983, The Astrophysical Journal, 270, 365

Mohr, P. J., & Taylor, B. N. 2005, Reviews of Modern Physics, 77, 1

Muller, C. A., & Oort, J. H. 1951, Nature, 168, 357

Navarro, J. F., Frenk, C. S., & White, S. D. M. 1997, The Astrophysical Journal, 490, 493

Navarro, J. F., Hayashi, E., Power, C., et al. 2004, Mnras, 349, 1039

Oh, S.-H., de Blok, W. J. G., Walter, F., Brinks, E., & Kennicutt, R. C., Jr. 2008, The Astronomical Journal, 136, 2761

Oh, S.-H., de Blok, W. J. G., Brinks, E., Walter, F., & Kennicutt, R. C., Jr. 2011, The Astronomical Journal, 141, 193

Oort, J. H. 1955, Vistas in Astronomy, 1, 607

Pence, W. D., Chiappetti, L., Page, C. G., Shaw, R. A., & Stobie, E. 2010, Astronomy & Astrophysics, 524, A42

Rhee, G., Valenzuela, O., Klypin, A., Holtzman, J., & Moorthy, B. 2004, The Astrophysical Journal, 617, 1059

Roelfsema, P. 1989, Synthesis Imaging in Radio Astronomy, 6, 315

Rogstad, D. H., Lockhart, I. A., & Wright, M. C. H. 1974, Astrophysical Journal, 193, 309

Sparke, L. S., & Gallagher, J. S., III 2007, Galaxies in the Universe, by Linda S. Sparke, John S. Gallagher, III, Cambridge, UK: Cambridge University Press, 2007.

Storey, J. W. V., Ashley, M. C. B., Naray, M., & Lloyd, J. P. 1994, American Journal of Physics, 62, 1077

Trachternach, C., de Blok, W. J. G., Walter, F., Brinks, E., & Kennicutt, R. C., Jr. 2008, The Astronomical Journal, 136, 2720

van Albada, T. S., Bahcall, J. N., Begeman, K., & Sancisi, R. 1985, Astrophysical Journal, 295, 305

van de Hulst, H. C. 1945, Ned.Tijd.Natuurkunde, 11, 210

van der Kruit, P. C., & Freeman, K. C. 2011, ARA&A, 49, 301

Weldrake, D. T. F., de Blok, W. J. G., & Walter, F. 2003, Mnras, 340, 12

Walter, F., Brinks, E., de Blok, W. J. G., et al. 2008, The Astronomical Journal, 136, 2563

VITA

The Graduate College
University of Nevada, Las Vegas

John Henry Boisvert

Degrees:
   Bachelor of Sciences, Physics, 2010
   University of Nevada Las Vegas

Thesis Title: How accurately can the inclination angle, position angle, and location of the dynamic center be measured from the neutral hydrogen disk in the central regions of dwarf galaxies?

Thesis Examination Committee:
   Chairperson, George Rhee, Ph. D.
   Committee Member, Stephen Lepp, Ph. D.
   Committee Member, Kentaro Nagamine, Ph. D.
   Graduate Faculty Representative, Rodney Metcalf, Ph. D.